UNIVERSITÀ DEGLI STUDI DI MILANO

FACOLTÀ DI SCIENZE E TECNOLOGIE

Corso di Laurea Magistrale in Fisica

A study for the measurement of the Λ baryon electromagnetic dipole moments in LHCb

Relatore: Prof. Nicola NERI
Correlatore: Dott.ssa Elisabetta SPADARO NORELLA

Tesi di Laurea di:
Alessandro DE GENNARO
Matricola 933289
Codice P.A.C.S.: 14.20.-c

Anno Accademico 2020–2021

Contents

Acknowledgements

The work presented in this thesis would not have been possible without steady input and support from the Milan and Valencia LHCb research groups. While it would be impossible for me to recount every contribution made, I struggle to think of a single person who did not volunteer to help me whenever I needed it.

Although I never had the pleasure of working alongside him directly, Salvatore Aiola laid most of the groundwork for the $\Lambda_b^0 \to J/\psi\,\Lambda^0$ signal selection process and his influence is ubiquitous. The foundation in such a sprawling analysis is often the most critical step, and I couldn't have asked for a better bedrock than the one he left me. His and Luca Pessina's comparative work on different multivariate classifiers was also instrumental in the choice of the histogrammed boosted decision tree I ended up using.

The treatment of ghost vertex $\Lambda^0 \to p\pi^-$ events owes a lot to Joan Ruiz Vidal's identification and systematization of the problem. Without his intuition and ψ–h parameterization of the ghost vertex locus of points, I would not have gained nearly as much insight into the nature of the issue and its impact on proton angular resolution.

Contributions by Andrea Merli and Giorgia Tonani cannot be overstated. Along with my supervisor and co-supervisor, they were the ones who molded the inexperienced physics student I was at the beginning of this year-long endeavour into the slightly more competent soon-to-be graduate I am now; without them, I doubt I would have achieved half of what is included in this thesis. Giorgia's excellent study of the Λ^0 polarization from the $\Xi_c^0 \to \Lambda^0 K^- \pi^+$ decay was a beacon of light during the drafting of Chapter 5 and spared me several sleepless nights.

Finally, special thanks are due to Fernando Martinez Vidal, with whom I worked closely in the development of the Armenteros-Podolanski veto and who went above and beyond in his guidance throughout.

Introduction

From the discovery of dark matter in spiral galaxies to the confirmation of neutrino oscillation as solution to the solar neutrino problem, evidence has piled up in favour of the incompleteness of the Standard Model of Particle Physics, currently the best description of particles at the subatomic level. The subject of violation of the CP discrete symmetry has gained traction in recent years due to the 10^{10} factor disparity between the known Standard Model sources of violation and the extent required to explain the present matter-antimatter asymmetry in the Universe.

One promising pathway to new physics is the study of electromagnetic dipole moments of elementary and composite particles. Permanent electric dipole moments (EDMs) introduce a CP-violating term in the system's Hamiltonian; given that expected Standard Model contributions are orders of magnitude smaller than current experiment sensitivities, EDM upper limits place strict constraints on the existence of new physics. Magnetic dipole moments (MDMs) can further be used to probe violation of the CPT theorem, which predicts MDMs to be identical in magnitude and opposite in sign for particles and matching antiparticles.

Electromagnetic dipole moments of long-lived particles can be measured from the precession of their spin-polarization vector in a strong magnetic field, which depends on the particle's gyroelectric and gyromagnetic factors. In this thesis, I present my work in preparation of a measurement of the electromagnetic dipole moments of the Λ^0 baryon with the LHCb experiment. Long-lived Λ^0 baryons from the exclusive $\Lambda_b^0 \to J/\psi\ (\to \mu^+\mu^-)\ \Lambda^0\ (\to p\pi^-)$ decay are selected with the requirement that the Λ^0 decay after the LHCb dipole magnet, allowing for the comparison of initial and final polarization states. Theoretical background for the EDM/MDM measurement approach and specifics on the LHCb detecting apparatus are reported in Chapters 1 and 2 respectively.

For the first part of my thesis, detailed in Chapter 3, I report on my work in understanding and improving the vertex reconstruction process in LHCb, with the main goal of mitigating the low efficiency of $\Lambda^0 \to p\pi^-$ reconstruction in $\Lambda_b^0 \to J/\psi\,\Lambda^0$ decays. I also analyze the z coordinate resolution of the reconstructed Λ^0 vertex to gauge possible sources of bias.

In the second part of my thesis, I focus on the development and finalization of the three major steps in the signal selection process: preliminary filters, rejection of $B^0 \to J/\psi\, K^0_S$ physical background, and discrimination of signal through the training and testing of a supervised learning multivariate classifier. Results on this front are collected in Chapter 4.

Finally, in Chapter 5 I capitalize on my earlier work to perform a first analysis of the angular distribution of $\Lambda^0 \to p\pi^-$ decay products, a key stepping stone in the prospective measurement of the Λ^0 electromagnetic dipole moments.

Chapter 1

Flavour physics and CP symmetry violation

This chapter explores the theoretical framework for the rest of the thesis. Section 1.1 provides a basic introduction to the Standard Model of Particle Physics and flavour physics in particular; Section 1.2 delves into the inner workings of discrete symmetries in quantum physics; Section 1.3 discusses the relevance of electromagnetic dipole moments of elementary particles as a test for CP violation and CPT symmetry; finally, Section 1.4 introduces the main physics motivation for this thesis, the study of dipole moments of the Λ^0 baryon and the proposed measurement technique.

1.1 The Standard Model of Particle Physics

Ever since Democritus' philosophy of atomism, one of the driving desires behind mankind's advancements in the fields of natural science has been to reduce reality to its basic components. While one can convincingly argue that we may never fully understand what has come to be known as the quantum world, the Standard Model of Particle Physics (Standard Model, or SM, for short) [1] is as close as physics has to offer to a comprehensive theory of the building blocks of matter and energy.

In addition to predicting a number of then-unknown particles discovered in later years, the Standard Model has shown remarkable consistency against high precision tests, especially in the better known electroweak sector [2]. Despite this, it would be a mistake to call it *complete*, even if only for the three fundamental forces it covers. Many experimental evidences, some of which will be discussed in the following pages, have already opened cracks in the model, and many more may emerge in the future; one of the recurring topics of this chapter will thus be the need for physics Beyond the Standard Model (BSM).

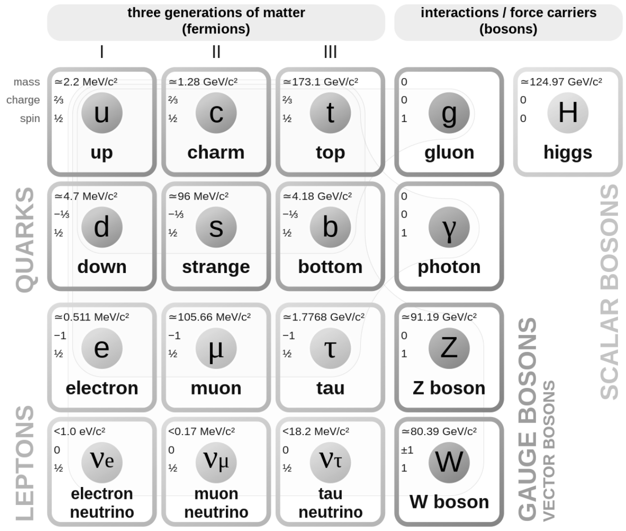

Figure 1.1: The seventeen currently known elementary particles of the Standard Model. Antiparticles are not depicted.

1.1.1 Elementary particles

Intuitively, a particle is said to be *elementary* when no substructure can be probed. A century of efforts in the fields of nuclear, quantum, and high energy physics has whittled down the spectrum of matter to just seventeen unique fundamental particles, colloquially known as the *particle zoo* and depicted in Figure 1.1.

Each particle is joined by an *antimatter particle* (*antiparticle* for short), a companion of opposite charge identified by the prefix *anti-*, e.g. antimuon for the muon; the only exception to this naming convention is the electron, whose antiparticle, for historical reasons, is known as positron. While often omitted for the sake of brevity, antiparticles are elementary particles in every respect, distinct from their partners (barring neutral gauge bosons and the Higgs boson, which are their own antiparticles) and related to them through the transformation of charge conjugation (see Section 1.2.2).

Leptons

Leptons are fermions (half-integer spin particles) not sensitive to the strong nuclear interaction. There are currently six *flavours* of leptons grouped in three generations: each generation comprises a *charged* lepton (electron, muon, tauon) and a *neutral* lepton (electron neutrino, muon neutrino, tauon neutrino).

All charged leptons have a charge of $-e$, where e is the elementary positive charge, and their masses range from $\approx 0.5\,\text{MeV}$ for the electron to over $1.7\,\text{GeV}$ for the tauon [3]. By contrast, as the names suggest, all neutrinos are electrically neutral and are assumed massless in the Standard Model[1]; this implies that their only meaningful interactions happen through the weak nuclear force, which grants them their characteristic evasiveness to most particle detectors.

Quarks

Much like leptons, quarks are also fermions existing in three generations. The main difference from the former category is that quarks, besides interacting through weak and electromagnetic forces, are also susceptible to the strong nuclear forces; this allows them to bind together in composite states known as *hadrons*, which are classified as *baryons* (states of three quarks) and *mesons* (states of one quark and one antiquark)[2].

Quarks can be classified as *up-type* (up, charm and top quarks) and *down-type* (down, strange and bottom quarks): up-type quarks have a fractionary charge of $+\frac{2}{3}e$, whereas down-type quarks have a charge of $-\frac{1}{3}e$. All quarks also have one of three *color* charges (red, green or blue), while antiquarks similarly have one of three *anti-color* charges (antired, antigreen or antiblue). A combination of all three colors/anti-colors or a combination of a color and its matching anticolor produces *colorless* particles, a property shared by all observed quark composite states.

Unlike leptons, quarks are impossible to observe directly: according to the phenomenon of *color confinement*, the energy of the interaction field between two color charges being pulled apart increases with their distance until it becomes high enough to create a quark-antiquark pair. This process of *fragmentation* develops many times over in such a way that the final observable state is entirely composed of colorless particles. For this reason, high energy physics experiments such as LHCb do not detect free quarks, instead observing cone-shaped streams of hadrons known as *hadronic jets*.

Gauge bosons and fundamental interactions

In quantum field theory, the interaction between two fields is implemented through the exchange of an intermediary particle known as *force carrier*. In the Standard Model all force carriers are vector (spin 1) bosons known as *gauge bosons*. The name is owed to the *gauge principle* used to introduce them: the

[1]The observation of flavour oscillation in solar neutrinos shows that neutrinos do in fact have non-zero, albeit very small, mass [4].

[2]As recently as 2003, evidence has surfaced for the existence of exotic hadrons composed of four (*tetraquarks*) [5] and five quarks (*pentaquarks*) [6].

localization of a global continuous symmetry group provides the free fermion Lagrangians with interaction terms with the proviso that one or more bosonic fields are introduced.

The gauge principle accounts for the implementation of three fundamental interactions along with their gauge bosons: the *strong nuclear force* with its massless gluon, responsible for the binding of both quarks inside baryons and nucleons inside atomic nuclei; the *electromagnetic force* mediated by the massless photon, the importance of which should be known from everyday life; and the *weak nuclear force* with two massive $W^{\pm}$ and Z bosons, the source of many subnuclear processes such as β radioactivity.

The latter two forces share a unified description in the Glashow-Weinberg-Salam theory as a single *electroweak interaction* and are introduced via localization of a $\mathrm{SU}(2)_L \otimes \mathrm{U}(1)_Y$ symmetry group, the first related to the conservation of weak isospin in left-handed chirality states and the second to the conservation of hypercharge. Quantum chromodynamics (QCD), the theory of the strong nuclear force, is based on a separate $\mathrm{SU}(3)_C$ symmetry acting on the three-dimensional space of color charges.

There are no gauge bosons nor gauge theories associated to the fourth known fundamental force, gravity. Since every attempt to reconcile the general theory of relativity with quantum mechanics has failed so far, gravity is presently excluded from the Standard Model. This doesn't affect SM predictions at the subatomic level on account of the remarkably low intensity of this force, over 30 orders of magnitude lower than the weak interaction.

The Higgs boson

The Higgs boson is one of the latest additions to the Standard Model, being proposed in 1964 [7] and observed in 2012 by the ATLAS [8] and CMS [9] collaborations. Its introduction solved perhaps the most insidious SM shortcoming at the time: gauge theories, which the model was built on, only worked under the assumption that all particles involved were massless, whereas the local invariance would fall apart (*gauge breaking*) when adding a free mass term.

The Higgs field accounts for mass generation of the weak bosons $W^{\pm}$ and Z via the Brout-Englert-Higgs mechanism resulting from the spontaneous electroweak symmetry breaking; elementary fermions also gain mass through a distinct, Yukawa-like interaction with the field.

1.1.2 Flavour physics

A reader unfamiliar with SM terminology may find amusing the use of the word *flavour* to refer to what have been so far presented as different kinds of particles altogether. However quirky, the lexical choice highlights a defining feature: flavour, much like the degree of sweetness in a recipe, can change [10].

As often happens in particle physics, the rules are somewhat easier for leptons. For a given generation $\ell = (e, \mu, \tau)$, one can define a lepton family number L_ℓ as the difference between the number of particles and antiparticles of said generation, charged leptons and neutrinos alike:

$$L_\ell \coloneqq n(\ell^-) - n(\ell^+) + n(\nu_\ell) - n(\bar{\nu}_\ell). \tag{1.1}$$

For all three generations, L_ℓ is conserved in every interaction except neutrino oscillations; an example is the dominant muon decay channel $\mu^- \to e^- \nu_\mu \bar{\nu}_e$, which maintains $L_\mu = 1, L_e = 0$.

Quarks are not as straightforward. A similarly defined quark flavour number, such as the so-called *topness* (or *truth*)

$$T \coloneqq n(t) - n(\bar{t}), \tag{1.2}$$

is preserved through EM and strong interactions, but can change when the state undergoes a weak charged interaction, i.e. a weak interaction mediated by the charged gauge bosons $W^\pm$. Weak interactions for quarks can be accurately described if we assume that the weak eigenstates (d', s', b') of down-type quarks, i.e. the weak isospin doublet partners to up-type quarks, are related to the free mass eigenstates (d, s, b) through a rotation:

$$\begin{pmatrix} d' \\ s' \\ b' \end{pmatrix} = \begin{pmatrix} V_{ud} & V_{us} & V_{ub} \\ V_{cd} & V_{cs} & V_{cb} \\ V_{td} & V_{ts} & V_{tb} \end{pmatrix} \begin{pmatrix} d \\ s \\ b \end{pmatrix}. \tag{1.3}$$

In this notation, the probability for a quark of flavour i to change into a quark of flavour j as a result of a weak charged interaction is proportional to $|V_{ij}|^2$.

The unitary rotation matrix is known as the Cabibbo-Kobayashi-Maskawa (CKM) matrix V_{CKM}. The moduli of its components up to the third decimal place, according to the most recent estimates [3], are

$$\begin{pmatrix} |V_{ud}| & |V_{us}| & |V_{ub}| \\ |V_{cd}| & |V_{cs}| & |V_{cb}| \\ |V_{td}| & |V_{ts}| & |V_{tb}| \end{pmatrix} \approx \begin{pmatrix} 0.974 & 0.224 & 0.004 \\ 0.221 & 0.987 & 0.041 \\ 0.008 & 0.039 & 1.013 \end{pmatrix}. \tag{1.4}$$

A full definition of the CKM matrix requires four independent parameters. Particularly useful for the following sections is the standard parameterization with three angles θ_{12}, θ_{23}, θ_{13}, expressing the mixing between different quark generations, and a complex phase δ_{13}. Defining $s_{ik} \coloneqq \sin\theta_{ik}$ and $c_{ik} \coloneqq \cos\theta_{ik}$, V_{CKM} can be written as

$$V_{\text{CKM}} = \begin{pmatrix} c_{12}c_{13} & s_{12}c_{13} & s_{13}e^{-i\delta_{13}} \\ -s_{12}c_{23} - c_{12}s_{23}s_{13}e^{i\delta_{13}} & c_{12}c_{23} - s_{12}s_{23}s_{13}e^{i\delta_{13}} & s_{23}c_{13} \\ s_{12}s_{23} - c_{12}c_{23}s_{13}e^{i\delta_{13}} & -c_{12}s_{23} - s_{12}c_{23}s_{13}e^{i\delta_{13}} & c_{23}c_{13} \end{pmatrix} \tag{1.5}$$

The measured hierarchy of $s_{13} \ll s_{23} \ll s_{12} \ll 1$ is often emphasized by using the Wolfenstein parameterization of V_{CKM}:

$$V_{\text{CKM}} = \begin{pmatrix} 1-\frac{\lambda^2}{2} & \lambda & A\lambda^3(\rho - i\eta) \\ -\lambda & 1-\frac{\lambda^2}{2} & A\lambda^2 \\ A\lambda^3(1-\rho-i\eta) & -A\lambda^2 & 1 \end{pmatrix} + \mathcal{O}(\lambda^4), \tag{1.6}$$

depending on the four parameters A, λ, ρ, η via

$$\lambda \coloneqq s_{12}, \tag{1.7a}$$

$$A\lambda^2 \coloneqq s_{23}, \tag{1.7b}$$

$$A\lambda^2(\rho + i\eta) \coloneqq s_{13}e^{i\delta_{13}}. \tag{1.7c}$$

The phase δ_{13} is known as the CP-violating phase. To fully understand what it means and its role in particle physics, however, a digression into discrete symmetries is needed.

1.2 Discrete symmetries and CP violation

In quantum mechanics, a system described by a Hamiltonian $\hat{\mathcal{H}}$ is *symmetric* under a transformation $\hat{S}$ if the two operators commute, i.e.

$$\left[\hat{\mathcal{H}}, \hat{S}\right] = 0. \tag{1.8}$$

Symmetries are of great relevance in physics on account of Noether's theorem, which establishes a relationship between the *continuous* symmetry of a system and a corresponding conservation law; the emphasis is on the requirement of continuity, meaning the related transformation changes the system «in a smooth way», much like a rotation does. An example of this principle has already been presented earlier in this thesis: the three symmetry groups employed in SM gauge theories all imply the conservation of a specific charge, be it weak isospin, hypercharge, or color.

This section will instead delve into *discrete* symmetries [11], which do not share said «smoothness» property. The absence of a Noether-like theorem for this class of transformations does not detract from their importance in physics: as will be shown, the three symmetries we'll focus on have a remarkable influence on many fields of study.

1.2.1 Parity inversion

The *parity inversion* (or simply *parity*) transformation $\hat{P}$ flips the sign of the three spatial coordinates:

$$\hat{P}: \begin{pmatrix} x \\ y \\ z \end{pmatrix} \to \begin{pmatrix} -x \\ -y \\ -z \end{pmatrix}. \tag{1.9}$$

Its action on a quantum $|\psi(\vec{x},t)\rangle$ is therefore

$$\hat{P}\,|\psi(\vec{x},t)\rangle = |\psi(-\vec{x},t)\rangle\,. \tag{1.10}$$

For parity eigenstates (known as parity-defined states) a parity quantum number can be introduced; such states may have a P-parity eigenvalue $\eta_P = +1$ (parity-even states) or $\eta_P = -1$ (parity-odd states). Since by definition $\hat{P}^2 = \mathbb{1}$, where $\mathbb{1}$ is the identity operator, these are the only two allowed P-parity values.

A similarly dichotomous behaviour is observed on both scalar and vector quantities commonly used in classical physics, such as momenta and electromagnetic fields. Parity-even scalar quantities are called *true scalars* or just *scalars* (e.g. energy), whereas parity-odd ones are called *pseudoscalars* (e.g. helicity). Likewise, vector quantities are either *axial vectors* (parity-even, e.g. angular momentum) or *polar vectors* (parity-odd, e.g. linear momentum).

As far as is currently known, gravity, electromagnetic and strong nuclear interactions conserve parity. The same cannot be said for the weak interaction, the P-violating properties of which were first proven in the 1956 Wu experiment on the ^{60}Co β^- decay [12].

1.2.2 Charge conjugation

The transformation of *charge conjugation* $\hat{C}$ changes the sign of all electric charges:

$$\hat{C}: q \to -q. \tag{1.11}$$

It should be readily apparent that $\hat{C}$ has close ties with the concept of antimatter. The action of charge conjugation turns a quantum state into its antimatter partner, inverting the sign of its quantum numbers in the process:

$$\hat{C}\,|\psi\rangle = |\bar{\psi}\rangle\,. \tag{1.12}$$

For single-particle systems, the only possible $\hat{C}$ eigenstates are particles that are their own antiparticle, like the photon, for which a C-parity $\eta_C = \pm 1$ is defined by analogy with the P-parity eigenvalue.

Unlike in the case of parity, there isn't a single breakthrough experiment credited for showing that the weak interaction is not C-symmetric: it was known from theory that parity violation in a weak process, when observed under certain conditions, would also imply a violation of charge conjugation, with such a violation being confirmed shortly after Wu's results [13]. As for the other three fundamental interactions, no evidence of C symmetry violation has surfaced so far.

1.2.3 Time reversal

Perhaps the most intuitively named of the three discrete symmetries discussed here, *time reversal* $\hat{T}$ does exactly what it promises:

$$\hat{T} : t \to -t. \tag{1.13}$$

The action of time reversal on a quantum state is represented by an *antiunitary* (unitary and antilinear) operator, which implies a complex conjugation on top of the time reversal itself:

$$\hat{T} \left| \psi(\vec{x}, t) \right\rangle = \left| \psi^*(\vec{x}, -t) \right\rangle \tag{1.14}$$

There are a number of arguments for the antiunitarity of $\hat{T}$, the most straightforward being that it prevents final states with negative energy.

Direct evidence of T violation in weak nuclear forces has surfaced in recent years starting with analyses at BaBar [14], whereas gravity, strong and electromagnetic forces are T-symmetric. However, as will be explained shortly, most experiments probing T violation do so indirectly by exploiting a side effect of the CPT theorem.

1.2.4 CP symmetry and violation

The sequential combination of C, P and T transformations, commonly designated as CPT symmetry, plays a key role in the foundations of quantum physics. As well as being the only combination of said transformations still observed to be a symmetry of physical laws, the *CPT theorem* states that any Lorentz-invariant local quantum field theory must be CPT-symmetric. Because a violation of the CPT symmetry would imply the collapse of the modern quantum physics framework, it is generally accepted that a T-violating process must also be a CP-violating process. This bears an important consequence on the study of discrete symmetry violations: because of the self-evident hindrances in building a time-reversed experimental setup outside of trivial cases, most tests of T violation are by necessity tests of CP violation.

CP symmetry is also an interesting field of study in and of itself [15]. While C and P symmetries are maximally violated by the weak interaction, CP isn't; this is exemplified by the chirally left-handed neutrino, which possesses a CP-partner (the right-handed antineutrino) despite lacking both a P-partner (the right-handed neutrino) and a C-partner (the left-handed antineutrino).

The subject of CP violation is also closely tied to another long-standing dilemma in both particle physics and cosmology: the observed asymmetry between matter and antimatter in our Universe. A perfectly CP-symmetric system would produce a roughly equal number of particles and antiparticles, which would annihilate one another and yield an empty Universe; our very existence implies a primordial imbalance that resulted in baryogenesis and therefore some degree of CP violation.

Since gravity, EM and strong interactions all individually conserve parity and charge conjugation, it stands to reason that they are also CP-symmetric, leaving the weak nuclear interaction as the only possible CP-violating fundamental force. Experiments conducted over the last 50 years have found that, despite CP still being preserved in most weak processes, some select interactions show evidence of CP violation.

The first indirect discovery came in 1964 by Christenson et al. [16], who observed the long-lived neutral kaon two-pion decay $K^0_L \to \pi^+\pi^-$ with a branching ratio of $\approx 10^{-3}$ over all charged modes. This result could only be explained by assuming that the K^0_L weak eigenstate is a mixture of both $\eta_{CP} = \pm 1$ eigenstates, with the ability to oscillate between the two. Another evidence was found in 1999 by the KTeV collaboration at Fermilab [17] via the observation of differing decay rates in $K^0_{L/S} \to \pi^+\pi^-$ against $K^0_{L/S} \to \pi^0\pi^0$ channels, and CP violation in weak processes was definitely established in the early 2000s via studies on B mesons decays conducted in so-called «B-factories» such as BaBar at SLAC [18] and Belle at KEK [19].

Despite the significant number of experimental evidences collected ever since, the extent of known CP-violating processes is several orders of magnitude below what is expected from cosmological estimates. The matter-antimatter imbalance at the time when the Universe cooled below the pair production threshold temperature can be quantified through the *baryon asymmetry parameter* [20], computed as the difference between the densities of baryons and antibaryons divided by their sum:

$$\eta \coloneqq \frac{n_B - n_{\bar{B}}}{n_B + n_{\bar{B}}}. \tag{1.15}$$

While this parameter cannot be directly measured at the present time, we can approximate it by noting that almost no antimatter currently exists in the Universe ($n_{\bar{B}} \approx 0$) and almost all of the original matter will have annihilated into photons ($n_B + n_{\bar{B}} \approx n_\gamma$):

$$\eta \approx \frac{n_B}{n_\gamma}. \tag{1.16}$$

Both of these quantities can be probed by studying the intergalactic medium and the cosmic microwave background, finding $\eta_{\text{obs}} \approx 10^{-10}$ [21]. As for the Standard Model prediction, all SM sources of CP violation arise from quark mixing, more specifically from the δ_{13} complex phase mentioned in the parameterization (1.5) of the CKM matrix. Computing the baryon asymmetry parameter with this knowledge leads to a much lower $\eta_{\text{SM}} \approx 10^{-20}$ [20].

New sources of CP violation are therefore required to match the observed value, with a promising field being the search for intrinsic electromagnetic dipole moments [15].

1.3 Electromagnetic dipole moments

1.3.1 EDMs

The electric dipole moment (EDM) $\vec{\delta}$ is the measure of a system's *polarity*, i.e. the spatial separation of positive and negative charges within the system. For the simplest of the relevant charge configurations, a dipole of point charges $\pm q$ separated by a distance r, the EDM is expressed as

$$\vec{\delta} = q\vec{r}, \tag{1.17}$$

where the displacement vector $\vec{r}$ points from the negative charge to the positive one.

It's hardly a feat of imagination to theorize that a composite particle like the neutron could acquire an EDM, even if the three quarks inside it cannot be thought of as a system of charges in the classical sense. It may be less intuitive that elementary, point-like particles such as electrons and quarks can also gain one due to quantum effects resulting in the creation and destruction of virtual particles (so-called *loops* in higher order Feynman diagrams).

For a spin-$\frac{1}{2}$ particle, its EDM is written in Gaussian units as [22]

$$\vec{\delta} = d\frac{\mu_B}{2}\vec{s}, \tag{1.18}$$

where d is a dimensionless quantity referred to as *gyroelectric factor*,

$$\mu_B = \frac{e\hbar}{2mc}, \tag{1.19}$$

is the particle magneton, c is the speed of light in a vacuum, m is the particle mass and

$$\vec{s} = 2\frac{\langle\vec{S}\rangle}{\hbar} \tag{1.20}$$

is the spin polarization vector, related to the average value of the spin $\vec{S}$ divided by the reduced Planck constant $\hbar$.

When the particle crosses an external electric field $\vec{E}$, its EDM will polarize by changing the direction of the spin. This introduces an energy term in the system's Hamiltonian with the form

$$H_{\mathrm{EDM}} = -\vec{\delta} \cdot \vec{E}. \tag{1.21}$$

We can now check how the term (1.21) behaves when acted upon by some of the discrete transformations outlined in Section 1.2. The behaviour of spin $\vec{S}$, hence of the spin-related EDM $\vec{\delta}$, can easily be shown to be that of axial vectors, i.e. parity-even. By contrast, the electric field $\vec{E}$ is a polar vector, i.e. parity-odd, which makes H_{EDM} a parity-odd pseudoscalar:

$$H_{\mathrm{EDM}} \xrightarrow{\hat{P}} -H_{\mathrm{EDM}}. \tag{1.22}$$

When considering time reversal $\hat{T}$, the situation is specular: the EDM $\vec{\delta}$ flips its sign, whereas the electric field $\vec{E}$ remains unchanged, implying

$$H_{\mathrm{EDM}} \xrightarrow{\hat{T}} -H_{\mathrm{EDM}}. \tag{1.23}$$

The above result in particular contains a crucial piece of information: assuming the validity of the CPT theorem, a Hamiltonian containing the EDM's interaction term (1.21) can only be CP-symmetric if the average (or *permanent*) EDM of the particle is zero.

It follows that, for a particle to have a permanent EDM, CP symmetry must be violated in some measure[3]. As explained in Section 1.2.4, the only known source of CP violation within the Standard Model is the complex phase δ_{13} in quark mixing, which may give a small contribution to the EDMs of point-like particles such as electrons ($\delta_e \lesssim 10^{-40}\,e\,\mathrm{cm}$ [23]) and quarks ($\delta_q \lesssim 10^{-34}\,e\,\mathrm{cm}$ [24]) via beyond-tree-level diagrams. Composite particles such as baryons are accorded some leeway on account of their finite size: the weak interaction between quarks inside the neutron, for instance, contributes to a possible EDM up to $\delta_n \lesssim 10^{-31}\,e\,\mathrm{cm}$ [25].

[3]This line of reasoning only applies to systems that are parity eigenstates. Water molecules are notoriously polar, but their EDMs do not violate any fundamental symmetry because the molecule's ground state is a superposition of parity-even and parity-odd eigenstates.

In all cases, the predicted SM contributions are orders of magnitudes below the sensitivity reached by current generation experiments. For all intents and purposes, the observation of a non-zero permanent EDM in a baryon would imply the discovery of a BSM source of CP violation.

1.3.2 MDMs

The magnetic dipole moment (MDM) $\vec{\mu}$ of a system can be interpreted as the measure of how intense a torque the system experiences when crossing a magnetic field $\vec{B}$:

$$\vec{\tau} = \vec{\mu} \times \vec{B}. \tag{1.24}$$

Unlike the case of EDMs, the extension of MDMs from classical to quantum physics is less extreme, as long as one acknowledges the affinity between angular momentum and a particle's intrinsic spin. A classical rotating body with charge q, mass m and angular momentum $\vec{L}$ gains an MDM in the form

$$\vec{\mu} = \frac{q}{2m}\vec{L}, \tag{1.25}$$

assuming charge and mass are identically distributed. A very similar relation holds for a non-classical, point-like spin-$\frac{1}{2}$ particle [22]:

$$\vec{\mu} = g\frac{\mu_B}{2}\vec{s}. \tag{1.26}$$

Here g is the dimensionless *gyromagnetic factor* accounting for the transition from classical to quantum physics, whereas μ_B and $\vec{s}$ are the same particle magneton and spin polarization vector defined in equations (1.19) and (1.20) respectively.

Similary to EDMs, MDMs also induce a spin rotation when subjected to a magnetic field $\vec{B}$, introducing a Hamiltonian term

$$H_{\text{MDM}} = -\vec{\mu} \cdot \vec{B}. \tag{1.27}$$

Under parity and time reversal transformations, the MDM $\vec{\mu}$ behaves in the same way as the EDM $\vec{\delta}$, both being dependent on the particle's spin $\vec{S}$ (even under $\hat{P}$, odd under $\hat{T}$). In contrast with $\vec{E}$, however, the magnetic field $\vec{B}$ behaves in the *same* way as $\vec{\mu}$, effectively cancelling out their signs when the Hamiltonian (1.27) is acted upon:

$$H_{\text{MDM}} \xrightarrow{\hat{P}} H_{\text{MDM}}, \tag{1.28}$$

$$H_{\text{MDM}} \xrightarrow{\hat{T}} H_{\text{MDM}}. \tag{1.29}$$

Factoring in the CPT theorem, this result entails that a non-zero intrinsic MDM for fundamental particles does not imply CP violation. For this reason, measurements of MDMs are instead used as precision tests of the CPT theorem, since their values should have same magnitude and opposite sign for a particle and its antimatter partner.

1.3.3 Measurement of EDMs and MDMs

For the purposes of this thesis, the measurement of EDMs and MDMs of a particle is performed by exploiting the precession of spin in an electromagnetic field [26]. In the laboratory frame, a neutral particle flying with velocity $\vec{\beta}$ through homogeneous electromagnetic fields $\vec{E}$ and $\vec{B}$ experiences a precession of the non-relativistic spin polarization vector $\vec{s}$ described by the equation

$$\frac{d\vec{s}}{dt} = \vec{s} \times \vec{\Omega}, \qquad \vec{\Omega} := \vec{\Omega}_{\mathrm{EDM}} + \vec{\Omega}_{\mathrm{MDM}}. \tag{1.30}$$

The angular velocity vector $\vec{\Omega}$ is itself the sum of two contributions due to the respective intrinsic dipole moments of the particle:

$$\vec{\Omega}_{\mathrm{EDM}} = \frac{d\mu_B}{\hbar}\left(\vec{E} - \frac{\gamma}{\gamma+1}(\vec{\beta}\cdot\vec{E})\vec{\beta} + \vec{\beta}\times\vec{B})\right), \tag{1.31}$$

$$\vec{\Omega}_{\mathrm{MDM}} = \frac{g\mu_B}{\hbar}\left(\vec{B} - \frac{\gamma}{\gamma+1}(\vec{\beta}\cdot\vec{B})\vec{\beta} - \vec{\beta}\times\vec{E})\right). \tag{1.32}$$

Assuming $\vec{E} = 0$, as will be the case in the experimental setup employed in this work, the angular velocity simplifies to

$$\vec{\Omega} = \frac{\mu_B}{\hbar}\left[d\vec{\beta}\times\vec{B} + g\left(\vec{B} - \frac{\gamma}{\gamma+1}(\vec{\beta}\cdot\vec{B})\vec{\beta}\right)\right]. \tag{1.33}$$

An analytical solution of the above system of equations is possible under the approximation that the precession of the particle spin depends only on the integrated value of the magnetic field $\vec{B}$ along the particle's flight path l. In the absence of field gradients, dictated by the homogeneity requirement, such integrated field $\vec{D}$ can be written as

$$\vec{D} := \int_0^l dl' \vec{B}(\vec{r}_0 + \hat{\beta}l') \approx \langle\vec{B}\rangle\, l, \tag{1.34}$$

where $\hat{v}$ labels the normalized vector of $\vec{v}$. The time evolution of the spin polarization vector $\vec{s}$ ($\vec{s}(0) = \vec{s}_0$) is

$$\vec{s}\,(t) = \left(\vec{s}_0\cdot\hat{\Omega}\right)\hat{\Omega} + \left[\vec{s}_0 - \left(\vec{s}_0\cdot\hat{\Omega}\right)\hat{\Omega}\right]\cos\left(\left|\vec{\Omega}\right| t\right) + \left(\vec{s}_0\times\hat{\Omega}\right)\sin\left(\left|\vec{\Omega}\right| t\right). \tag{1.35}$$

From an experimental point of view, measurement of time isn't trivial; instead, one can efficiently measure the flight length of an unstable particle $l = \beta c t$ during its lifetime. The equation describing the spin precession as a function of l has a very similar form to (1.35):

$$\vec{s}\,(l) = \left(\vec{s}_0 \cdot \hat{\Phi}\right) \hat{\Phi} + \left[\vec{s}_0 - \left(\vec{s}_0 \cdot \hat{\Phi}\right) \hat{\Phi}\right] \cos\left|\vec{\Phi}\right| + \left(\vec{s}_0 \times \hat{\Phi}\right) \sin\left|\vec{\Phi}\right|, \tag{1.36}$$

with precession angle vector

$$\vec{\Phi} = \frac{\mu_B}{|\vec{\beta}|\hbar c}\left[d\vec{\beta} \times \vec{D} + g\left(\vec{D} - \frac{\gamma}{\gamma+1}(\vec{\beta}\cdot\vec{D})\vec{\beta}\right)\right] \tag{1.37}$$

and $\vec{D}$ defined as in (1.34).

Equation (1.36) provides a way to measure the values of EDMs and MDMs for neutral particles by studying the change in polarization after their flight through a magnetic field. For unstable particles, the polarization at the time of decay can be inferred in a fairly straightforward way from the angular distribution of their products. Conversely, theoretical knowledge or measurement of the original spin polarization $\vec{s}_0$ of the particle are both far from easy tasks in a general setting.

1.4 Proposal of a measurement of the Λ^0 electromagnetic dipole moments with the LHCb detector

The Λ^0 baryon, also historically known as the Λ^0 hyperon[4] and sometimes labelled only as Λ, is a spin-$\frac{1}{2}$ baryon with (u, d, s) valence quarks. As the first identified baryon beyond the two nucleons, it played a key role in the discovery and christening of the strange quark: its mass of $\approx 1116\,\mathrm{MeV}/c$ [3], the lightest among s-bearing baryons, meant its only viable decay channels were mediated by the flavour-changing weak interaction, giving the Λ^0 a much longer half-life than expected; this property was dubbed *strangeness*, a name later inherited by the new quark that indirectly caused it.

The Λ^0 baryon is a prime candidate to probe CP violation. Unlike in the

[4] A *hyperon* is a baryon with one or more strange quarks, but no heavier quarks. The nomenclature emerged in the period following the discovery of the strange quark, when no further quarks besides the first three were known; nowadays, the term is rarely used.

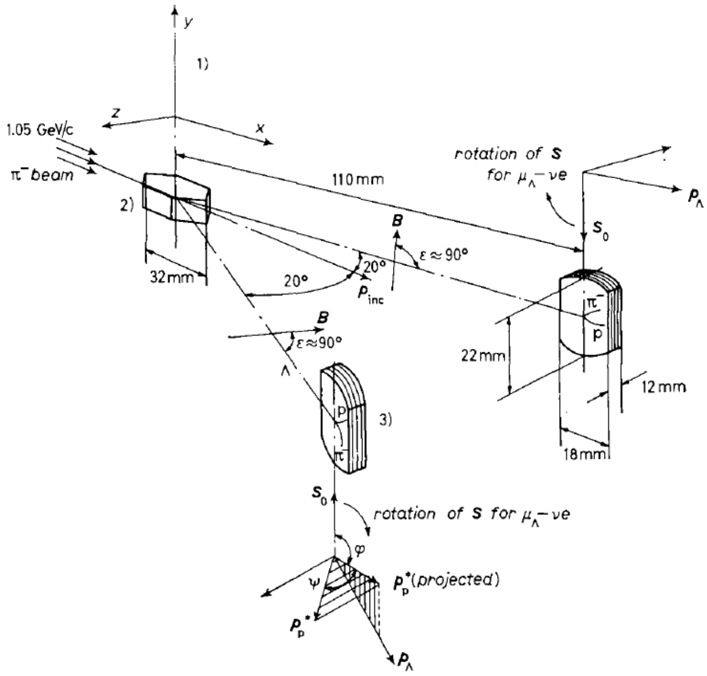

Figure 1.2: Experimental layout used for the 1971 Λ^0 EDM/MDM measurements [28].

case of the prospective discovery of a neutron EDM[5], a non-zero Λ^0 baryon EDM could not be explained by any phenomena within the Standard Model and would therefore imply the existence of BSM physics.

1.4.1 Highlights from previous measurements of the Λ^0 dipole moments

Among the first meaningful measurements of the Λ^0 electromagnetic dipole moments were conducted in the early seventies at CERN near Geneva, Switzerland, by means of nuclear emulsion experiments [28] [29]. The experimental layout is sketched in Figure 1.2: Λ^0 baryons are produced via reaction

$$\pi^- + p \to \Lambda^0 + K^0, \tag{1.38}$$

[5] Quantum chromodynamics allows for a CP-violating term proportional to the QCD vacuum angle θ. Current measurements of the neutron EDM [27] constrain $\theta \lesssim 10^{-10}$, a fine-tuning suppression known as the *strong CP problem*; nevertheless, experimental discovery of a non-zero neutron EDM could be traced back to this term and would not necessarily require the introduction of new physics.

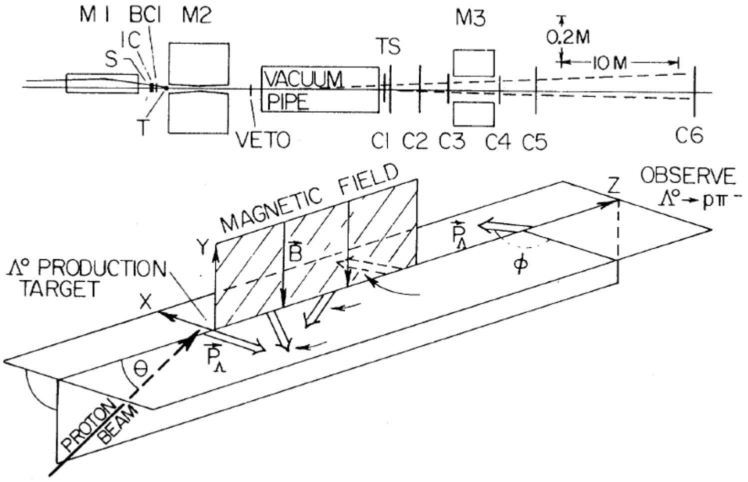

Figure 1.3: Side view of the experimental apparatus (*top*) and perspective illustration of the coordinate system (*bottom*) of the Fermilab setup for the Λ^0 EDM/MDM measurements [30].

running a 1.05 GeV/c π^- beam from the CERN Proton Synchrotron accelerator into a fixed polyethylene target. The production cross section has a maximum value of 0.8 mb and the resulting Λ^0 have $\approx 100\%$ transverse polarization over a large angular production region in the reaction reference frame. The Λ^0 angular acceptance was restricted to 18°–22°, near the maximum production angle of 21°, to amplify the signal-to-background ratio; this corresponds to Λ^0 with $|\vec{p}| \in [500\,\mathrm{MeV/c}, 800\,\mathrm{MeV/c}]$. Traversing a 20 T transverse pulsed magnetic field, Λ^0 baryons become spin-polarized as described in Section 1.3.3 before decaying into a $p\pi^-$ pair. The final polarization direction is probed through the angular distribution of the above decay products, detected by 1.2 mm thick Ilford K5 nuclear emulsion stacks. The measured Λ^0 magnetic dipole moment, improving an order of magnitude over the previous world average value, was

$$\mu_\Lambda = (-0.66 \pm 0.07)\,\mu_N, \tag{1.39}$$

with μ_N being the nuclear magneton [28]. The Λ^0 EDM was measured at

$$\delta_\Lambda = (-5.9 \pm 2.9) \times 10^{-15}\ e\ \mathrm{cm}, \tag{1.40}$$

the 95% confidence level upper limit being found at $\delta_\Lambda \lesssim 10^{-14}\ e$ cm [29].

These results were improved during the late seventies and early eighties with the neutral hyperon spectrometer at Fermilab in Batavia, Illinois [30] [31]. Figure 1.3 depicts the experimental setup: the incident 300 GeV proton beam impacts on a beryllium target with an angle determined by the M1 upstream magnet; outgoing particles are focused by a brass collimator and cross the M2 magnetic field, serving the dual purpose of purging the beam of charged particles and triggering the Λ^0 spin precession in the horizontal plane; finally, the $\Lambda^0 \to p\pi^-$ decay products within a defined volumetric acceptance are detected by the C1–C6 multi-wire proportional chambers. With a much lower Λ^0 initial polarization ($\approx 8\%$ on average) with respect to the CERN emulsion experiments, the Fermilab team was nonetheless able to best their results owing to a tenfold increase in Λ^0 statistics and precise measurement of the integrated magnetic field. The extracted value for the MDM [30] was

$$\mu_\Lambda = (-0.6138 \pm 0.0047)\,\mu_N, \tag{1.41}$$

while the EDM measurement [31] was

$$\delta_\Lambda = (-3.0 \pm 7.4) \times 10^{-17}\ e\ \text{cm}, \tag{1.42}$$

setting the upper limit to $\delta_\Lambda < 1.5 \times 10^{-16}\ e$ cm [3]. At the time of writing, this is the current best limit on the Λ^0 electric dipole moment. This is still orders of magnitudes removed from the SM upper limit of

$$\delta_\Lambda < 4.4 \times 10^{-26}\ e\ \text{cm}, \tag{1.43}$$

computed from the experimental upper limit on the neutron EDM [32].

1.4.2 Proposal overview

My work in this thesis is directed towards the prospective measurement of the Λ^0 baryon electromagnetic dipole moments with the LHCb experiment[6] at the Large Hadron Collider (see Chapter 2), exploiting the spin precession technique outlined in Section 1.3.3 [26]. The unique features of the LHCb experimental setup and a careful selection of the Λ^0 production channel will allow for significant simplifications of the general equation (1.36) for neutral unstable particles.

The LHCb detector is equipped with a magnetic field directed along the laboratory frame y axis[7] used for tracking purposes. Gradient field effects for the $\vec{B}$ field within the detector acceptance are negligible, being estimated at [26]

$$\frac{\hbar}{2mc}\frac{\beta\gamma}{\gamma+1}\frac{|\nabla B|}{B} \approx 7.4 \times 10^{-16}, \tag{1.44}$$

[6]LHCb is also active in the measurement of permanent electric dipole moments of other baryons. Measurement of Λ_c^+ and Ξ_c^+ EDMs exploiting the spin precession of positively-charged particles channeled through bent crystals is specifically under consideration [26].

[7]The remainder of this chapter assumes the standard right-handed LHCb coordinate system, see Section 2.2.

with $B \coloneqq |\vec{B}|$. Assuming production near the beam collision point, the Λ^0 baryon's average mean life of $\approx 2.6 \times 10^{-10}\,\mathrm{s}$ [3] allows a sizeable number of them to traverse at least part of the LHCb magnetic field region (roughly ranging $z = 2.5\,\mathrm{m}$–$7.95\,\mathrm{m}$) before decaying. Spin precession can thus be measured, provided we know both initial and final polarization states.

1.4.3 Polarization measurements

The problem of the Λ^0 initial polarization measurement is circumvented by selecting Λ^0 produced through the weak decay of the bottom baryon Λ_b^0

$$\Lambda_b^0 \to J/\psi\ (\to \mu^+\mu^-)\ \Lambda^0\ (\to p\pi^-), \tag{1.45}$$

as well as its charge-conjugate[8]

$$\bar{\Lambda}_b^0 \to J/\psi\,(\to \mu^+\mu^-)\,\bar{\Lambda}^0\,(\to \bar{p}\pi^+). \tag{1.46}$$

Parity violation in this decay produces Λ^0 with almost 100% longitudinal polarization [33], meaning that the original polarization is aligned to the Λ^0 momentum in the Λ_b^0 helicity frame (see Figure 1.5 and related discussion).

The forward nature of the LHCb detector implies that Λ^0 baryons will mostly fly along the laboratory frame z axis, and therefore the initial polarization can be written as $\vec{s_0} = (0, 0, s_0)$. Equation (1.36) for the Λ^0 spin precession after the magnetic field region can thus be simplified assuming a field $\vec{B} = (0, B_y, 0)$:

$$\vec{s} = \begin{cases} s_x = -s_0 \sin\Phi \\ s_y = -s_0 \frac{d\beta}{g} \sin\Phi \\ s_z = s_0 \cos\Phi \end{cases}, \tag{1.47}$$

with

$$\Phi = \frac{D_y \mu_B}{\beta\hbar c}\sqrt{d^2\beta^2 + g^2} \approx \frac{g D_y \mu_B}{\beta\hbar c}, \tag{1.48}$$

$\beta \coloneqq \left|\vec{\beta}\right|$ and

$$D_y \coloneqq D_y(l) = \int_0^l dl' B_y. \tag{1.49}$$

Note from equation (1.47) that a non-vanishing intrinsic EDM introduces a s_y component to the final polarization, the MDM precession of which would otherwise be confined to the xz plane.

[8]For the sake of brevity, charge-conjugate notation will be omitted in the rest of this thesis except where relevant to the topic at hand.

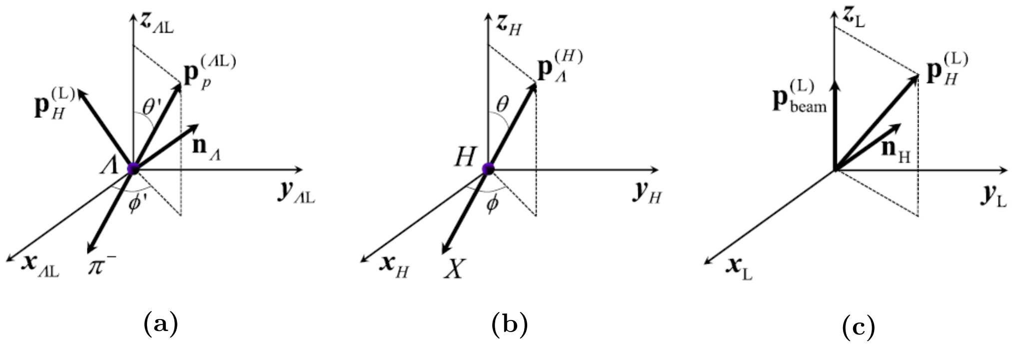

Figure 1.4: Frames of reference for the $\Lambda_b^0 \to J/\psi\ (\to \mu^+\mu^-)\ \Lambda^0\ (\to p\pi^-)$ decay [26]: *(a)* the Λ^0 helicity frame $S_{\Lambda L}$; *(b)* the Λ_b^0 (heavy hadron) helicity frame S_H; *(c)* laboratory frame S_L. $\vec{p}_H$ is the Λ_b^0 momentum, $\vec{p}_\Lambda$ is the Λ^0 momentum (corresponding to solid angle (θ, ϕ) in the S_H frame) $\vec{p}_p$ is the proton momentum (corresponding to solid angle (θ', ϕ') in the $S_{\Lambda L}$ frame), $\vec{p}_{beam}$ is the proton beam momentum, while $\vec{n}_\Lambda$ and $\vec{n}_H$ are the normals to the Λ^0 and Λ_b^0 production planes respectively.

The polarization after the magnetic field can be probed by studying the angular distribution of the $\Lambda^0 \to p\pi^-$ decay products. The expected angular distribution for said decay [26] [34] [35] is

$$\frac{dN}{d\Omega'} = 1 + \alpha \vec{s} \cdot \hat{k}', \tag{1.50}$$

where $\Omega' := (\theta', \phi')$ is the solid angle in the Λ^0 helicity frame (see Figure 1.4a), corresponding to the momentum direction of the proton and pointing along the unit vector

$$\hat{k}' = \begin{pmatrix} \sin\theta' \cos\phi' \\ \sin\theta' \sin\phi' \\ \cos\theta' \end{pmatrix}, \tag{1.51}$$

whereas $\alpha \approx 0.732$ [3] is the decay asymmetry parameter. The combined measurements of the initial polarization (from the momenta of Λ^0 produced via decays (1.45) and (1.46)) and the final polarization (from angular distribution (1.50)) allow for a study of Λ^0 electromagnetic dipole moments based on the single components of the precession (1.47).

Deviations from this simplified treatment ought to be considered when taking into account the different relevant frames of reference, three of which are sketched in Figure 1.4:

- the two Λ^0 helicity frames $S_{\Lambda L}$ (Figure 1.4a) and S_Λ. These are functionally the same frame of reference, the difference being that the z axis is defined in the direction of the Λ^0 momentum in S_L and S_H respectively;

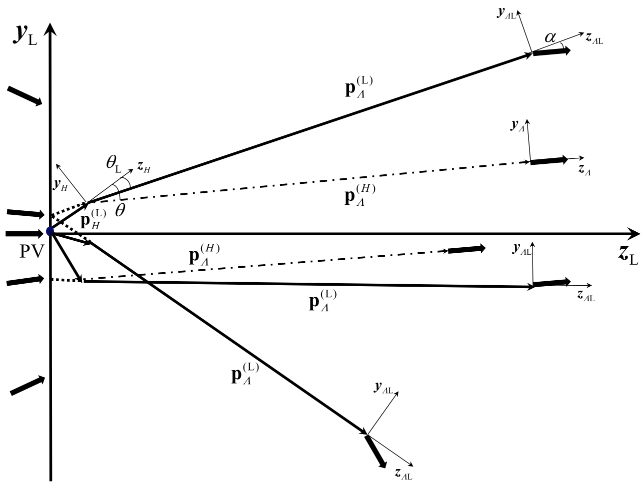

Figure 1.5: Sketch of the Λ_b^0 production at the primary vertex (PV) and its decay into Λ^0 in the three S_H, S_Λ and $S_{\Lambda L}$ frames of reference, as seen from the S_L yz plane [26]. Particle momenta are represented as *solid* lines for S_L, *dash-dotted* lines for S_H. The Λ^0 polarization vector (*thick arrows on the right*) is aligned to the S_Λ z axis and rotated by Wick angle α in $S_{\Lambda L}$. *Short-dashed* lines trace the $p_\Lambda^{(L)}$ back to the $z = z_{PV}$ plane, identifying the apparent production point of the Λ^0 in S_L (impact parameter). These points correlate with the Λ^0 helicity angle θ computed in S_H, also pictured in S_L as θ_L. By virtue of (1.52), this imprints a correlation between Λ^0 impact parameter and Wick rotation of its polarization vector, pictorially highlighted by the *thick arrows on the left.*

- the heavy hadron Λ_b^0 helicity frame S_H (Figure 1.4b), with the z axis given by the Λ_b^0 momentum in S_L and the x axis parallel to the normal to its production plane;
- the laboratory frame S_L (Figure 1.4c), with the z axis along the proton beam and the y axis along the vertical coordinate.

The polarization given by the equation of motion derived in Section 1.3.3 refers to the comoving rest frame of the Λ^0 (also known as the *canonical frame)*, related to the S_L frame by a Lorentz boost. By contrast, Equation (1.50) for the angular distribution is computed with the solid angle Ω' in the particle helicity frame $S_{\Lambda L}$. Canonical and helicity frames are related by a rotation angle, meaning that $\vec{s_0}$ is not fixed to be perpendicular to $\vec{B}$, as assumed in the solution of system (1.33). This effect arises in the case of Λ^0 not directed along the S_L z axis and is expected to be negligible in the single-arm geometry of the LHCb detector.

More significant is the Wick rotation (see Figure 1.5), owing to the orientation discrepancy between S_Λ frame (where the Λ^0 has the maximal longitudinal polarization) and $S_{\Lambda L}$ (where the angular distribution of Λ^0 decay products is measured). This phenomenon introduces a dilution effect to the precession measurement: a Λ^0 with polarization $\vec{s_0} = s_0 \hat{z}_\Lambda$ in the S_Λ frame gains in the $S_{\Lambda L}$ frame a transverse component of magnitude $s_0 \sin\alpha$, where

$$\sin\alpha = \frac{m_\Lambda}{m_H} \frac{\left|\vec{p}_H^{(L)}\right|}{\left|\vec{p}_\Lambda^{(L)}\right|} \sin\theta \tag{1.52}$$

and θ is the Λ^0 helicity angle, i.e. the angle formed by the Λ^0 momentum in S_H with respect to the frame z_H axis [36]. As seen from Figure 1.5, the helicity angle θ is related to the impact parameter with respect to the primary vertex in the S_L frame [37]. Since θ determines the magnitude of Wick angle α, this relation can be exploited to select ensembles of Λ^0 with similar initial polarization, so that the Wick effect on the particles within a specific ensemble can be neglected. The dilution can also be circumvented by computing the angular distribution directly in the S_Λ frame, which is the solution I adopted in Chapter 5.

1.4.4 Closing remarks

The LHCb tracking dipole magnet provides an integrated field $D_y \approx \pm 4\,\mathrm{T\,m}$ [38], allowing for a maximum precession angle of $\Phi_{\max} \approx \pm\frac{\pi}{4}$ for Λ^0 baryons traversing the entire region and reaching about 70% of the maximum s_y component in equation (1.47).

Dedicated sensitivity studies [26] show that the projected sensitivity on the Λ^0 gyroelectric factor scales with the number $N_\Lambda^{\mathrm{reco}}$ of reconstructed $\Lambda_b^0 \to J/\psi\,\Lambda^0$ events and initial polarization s_0 as

$$\sigma_d \propto \frac{1}{s_0\sqrt{N_\Lambda^{\mathrm{reco}}}}. \tag{1.53}$$

With the $9\,\mathrm{fb}^{-1}$ integrated luminosity[9] provided by the LHC Run[10] 1 and 2 data collected with the LHCb detector and a global event reconstruction efficiency of $\varepsilon = 0.2\%$, the attainable sensitivity on the Λ^0 gyroelectric factor d has been estimated at $\sigma_d \approx 1.5\times10^{-3}$, to be compared with the current best limit of 1.7×10^{-2} [31]. Assuming the $50\,\mathrm{fb}^{-1}$ luminosity projected for the end of Run 4 and an efficiency $\varepsilon = 1\%$ achievable with the upgraded LHCb trigger system (see Section 2.4), this limit can further be improved to $\approx 3\times10^{-4}$ [26]. A precision measurement of the gyromagnetic factor g for Λ^0 and $\bar{\Lambda}^0$ baryons could also serve as a further precision test of the CPT theorem.

[9] See Section 2.2 for a formal definition of luminosity and its role in particle colliders.
[10] *Run* is the conventional term for data-taking periods at LHC, see Section 2.1.

Chapter 2

The LHCb experiment

2.1 The Large Hadron Collider

The Large Hadron Collider (LHC for short) is the largest and most powerful particle collider in the world. When the LHC was first approved by the European Organization for Nuclear Research (CERN) in 1994, it was originally going to be built with an initial center-of-mass collision energy $\sqrt{s} = 10\,\mathrm{TeV}$, with the plan to upgrade it to $14\,\mathrm{TeV}$ at a later stage; however, after negotiations with nonmember states, in 1996 the CERN council approved the construction at $14\,\mathrm{TeV}$ energy in one stage [39].

LHC is located at the CERN laboratory near Geneva, Switzerland, housed in the underground tunnel previously occupied by the LEP experiment. Its structure, sketched in Figure 2.1, consists of two counterrotating rings hosting beams for particle-particle collisions (mainly protons, but LHC is also used for ion collisions).

Four main experiments are stationed at the LHC ring intersection points: ATLAS and CMS are high-luminosity[11] experiments focused on general purpose proton-proton collisions; ALICE is optimized for lead-on-lead collisions with lower center-of-mass energy and luminosity compared to the former two; finally, LHCb is dedicated on the study of b hadrons and will be the focus of the rest of this chapter. Beyond the above four, a number of small-scale, more specialized experiments also work with LHC, such as TOTEM, MilliQan and MoEDAL.

The LHC schedule alternates data collection phases (*Runs*) with maintenance work phases (*Long Shutdowns*, LS for short); while the shutdowns are designed for consolidation and improvement of the collider itself, mainstay experiments usually take advantage of the hiatus to upgrade their detectors

[11] See Section 2.2 for a formal definition of luminosity and its role in particle colliders.

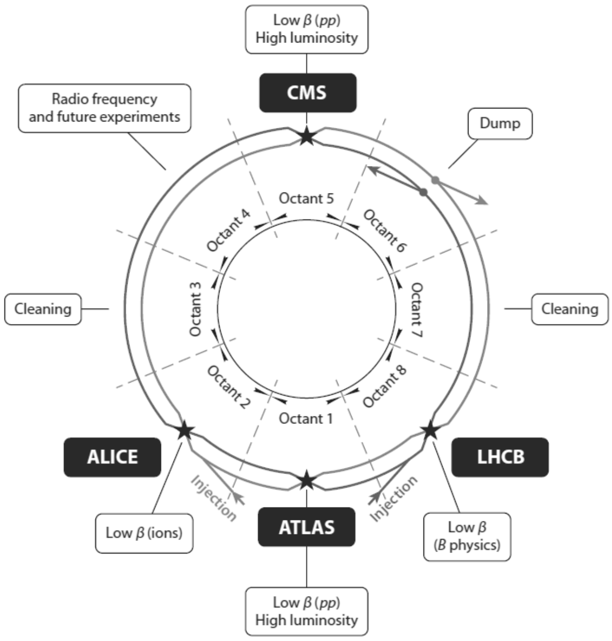

Figure 2.1: Layout of the Large Hadron Collider with its four main experiments [39].

in both hardware and software. Run 1 began in 2010 and continued until early 2013, during which period the LHC provided a center-of-mass energy of $\sqrt{s} = 7$–8 TeV. After the 2-year-long interruption for LS1, operations resumed in 2015 for Run 2 with an upgraded $\sqrt{s} = 13\,\text{TeV}$. The collider was once again shut down at the end of 2018 (LS2) and work began towards the High Luminosity (HiLumi) upgrade of the LHC. After suffering delays due to the COVID-19 pandemic, Run 3 is currently scheduled to start in the second quarter of 2022 with $\sqrt{s} = 14\,\text{TeV}$, finally reaching its maximum collision energy by design.

2.2 The LHCb experiment and detector

LHCb (the b stands for *beauty*[12]) is a single-arm detector designed to study heavy-flavour physics at the LHC, with the main objective of providing precision measurements of CP violation and rare decays of b and c hadrons [41].

[12]Before settling on the names *top* and *bottom* for the third generation of quarks, the names *truth* and *beauty* were among those proposed. While they never gained enough momentum in the scientific community, echoes of the failed nomenclature are still present in heavy quark vocabulary, for instance in the alternative name *truth* for the *topness* flavour number mentioned in Section 1.1.2, as well as in the official name for the LHCb experiment.

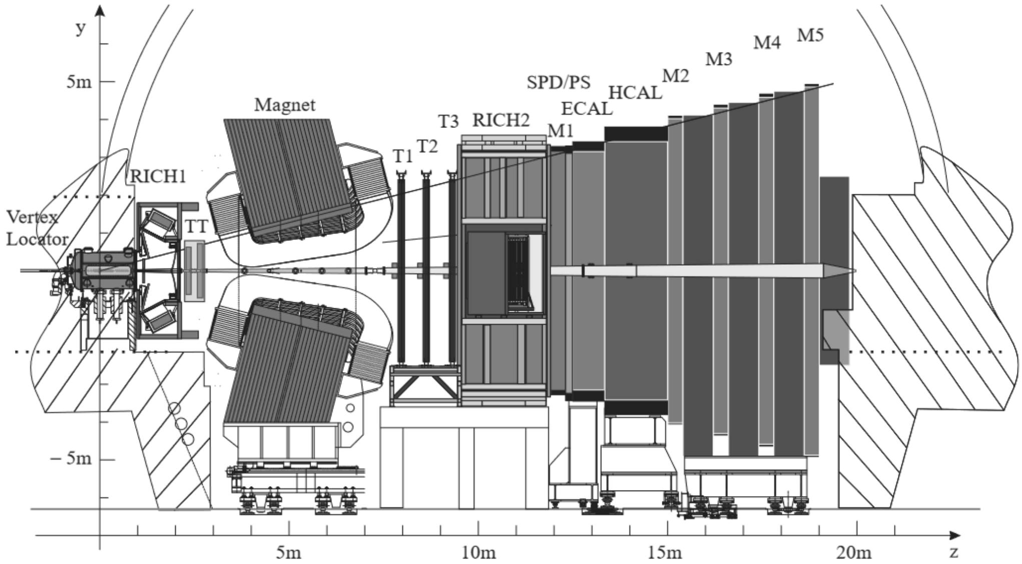

Figure 2.2: Side view of the LHCb detector used for LHC Runs 1 and 2 [40].

Unlike the other three main experiments at LHC, LHCb has a forward-optimized geometry shown in Figure 2.2, with an angular acceptance of 10–300 mrad in the bending plane and 10–250 mrad in the non-bending plane. Such a layout, more reminiscent of fixed target experiments than beam colliders, is motivated by the fact that $b\bar{b}$ pairs produced at high energies are usually collimated in the same forward/backward cone. A more in-depth look at the tracking and particle identification systems will be taken in Sections 2.2.1 and 2.2.2 respectively. The standard LHCb coordinate system, used as reference for the rest of this thesis, is a right-handed system centered on the beam interaction point, with the z axis along the the beam pipe and y axis directed vertically upwards.

An important parameter for detectors is *istantaneous luminosity*, also often cited as simply *luminosity*. At a beam collider such as LHC, luminosity $\mathcal{L}$ is defined as

$$\mathcal{L} = \frac{f_{\mathrm{BC}} N_1 N_2 F}{4\pi\sigma_x\sigma_y}, \tag{2.1}$$

with f_{BC} being the collision frequency of proton bunches, $N_{1,2}$ the number of protons in each beam and $\sigma_x\sigma_y$ the beam cross-section in the transverse plane; geometrical factor F parameterizes the crossing angle between the two beams. *Integrated luminosity* $\int \mathcal{L}\,dt$ is used to quantify the magnitude of data collected in a definite timespan. Table 2.1 reports instantaneous and integrated luminosities for the foreseen LHCb schedule up until 2040. In Runs 1 and 2,

	Run 1	Run 2	Run 3	Run 4	Run 5	Run 6
Years	2011–12	2015–18	2022–24	2027–30	2032–34	2036–40
Collider	LHC			HiLumi-LHC		
Detector	Current		Upgrade I	Upgrade Ib	Upgrade II	
$\mathcal{L}$	$2 \times 10^{32}\,\mathrm{cm}^{-2}\,\mathrm{s}^{-1}$		$2 \times 10^{33}\,\mathrm{cm}^{-2}\,\mathrm{s}^{-1}$		$2 \times 10^{34}\,\mathrm{cm}^{-2}\,\mathrm{s}^{-1}$	
$\int \mathcal{L}\,dt$	$3\,\mathrm{fb}^{-1}$	$6\,\mathrm{fb}^{-1}$	$25\,\mathrm{fb}^{-1}$	$50\,\mathrm{fb}^{-1}$	$300\,\mathrm{fb}^{-1}$	

Table 2.1: Key detector and collider parameters for planned LHCb Runs until 2040. Values for Run 3 and beyond are based on projections.

LHCb has operated at a luminosity two orders of magnitude below the peak achievable LHC luminosity used by ATLAS and CMS; this decision was taken to reduce the particle flux in the acceptance region, which would otherwise create occupancy problems and shorten the detector lifespan due to radiation damage.

By all accounts, LHCb has been an incredibly successful experiment, reaching its 600th publication by the end of 2021 and leading to state-of-the-art results both within and outside of its intended research framework. Among the main results achieved by the LHCb Collaboration in the field of CP symmetry violation are world-class precision measurements of heavy quark mixing [42] [43], the first observation of CP violation in the charm sector [44] and competitive measurements of the CKM unitarity triangle parameters [45]. LHCb has also been active in the study of rare b-hadron decays [46], as well as in conventional and exotic hadron spectroscopy [47], particularly concerning evidences of new pentaquark states [48]. Finally, LHCb has the distinction of being the only current LHC experiment with the ability to use a fixed-target setup by exploiting the SMOG internal gas target [49], originally developed for precise luminosity measurements; ever since 2015, the adoption of noble gas targets has allowed the Collaboration to obtain b-physics results involving nuclear collisions [50].

2.2.1 Tracking

LHCb dipole magnet

In order to measure the momenta of charged particles through their bending curve, LHCb employs a warm dipole magnet [51] consisting of two trapezoidal coils bent at 45° on the two transverse sides, seen in Figure 2.2 around $z \approx 5\,\mathrm{m}$ (the magnet is placed so that the line connecting the centers of the pole faces

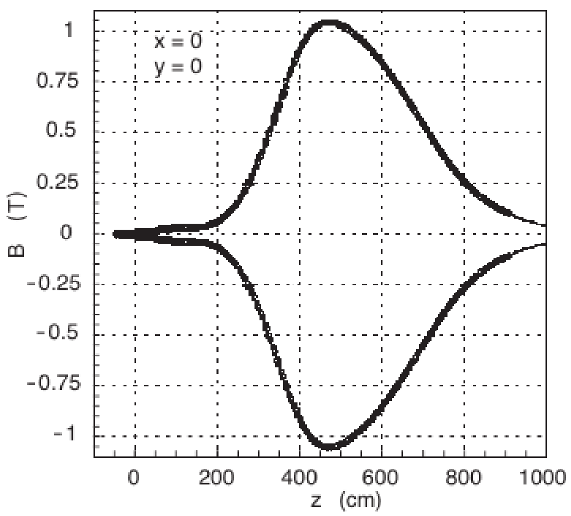

Figure 2.3: LHCb magnetic field along the z axis [51].

crosses $z = 5.3\,\mathrm{m}$).

The LHCb magnet provides an integrated field of $\int Bdl \approx \pm 4\,\mathrm{T\,m}$ for $10\,\mathrm{m}$ tracks[13]. Most of this field is contained in the $z \in [2.5, 7.95]$ m region, with a small fraction ($\int Bdl \approx 0.12\,\mathrm{T\,m}$) upstream of $z = 2.5\,\mathrm{m}$. This design was the result of a compromise between a $\leq 2\,\mathrm{mT}$ field requirement inside the RICH envelopes (see Section 2.2.2) and the desire for the highest intensitity possible in the tracking regions between the VELO and T1–T3 stations (see later in this section).

Intensity of the magnetic field along the three cartesian directions was measured using an array of 60 sensor cards covering a $80\,\mathrm{mm} \times 80\,\mathrm{mm}$ grid and compared to simulations with TOSCA[14]. The sensor cards each contained three Hall effect probes and were calibrated up to a 10^{-4} precision. Measurements were conducted in all tracking station regions, as well as inside the magnetic shielding of the two RICH detectors. The field map along z, measured with a precision of 4×10^{-4}, is shown in Figure 2.3 for $x = y = 0$. Dishomogeneities in the xy plane for fixed z are estimated at $\lesssim 6\%$ within the LHCb detector acceptance. Measurements are in $\leq 1\%$ agreement with the TOSCA model, except in the VELO and RICH1 regions of the detector, where a larger $\approx 3.5\%$ discrepancy was attributed to the vicinity of the iron reinforcements in the

[13] The $\pm$ sign is due to the fact that the magnet operates alternatively in up and down polarities, inverting the sign of the magnetic field.

[14] Analysis package for the solution of non-linear magnetostatic field problems, part of the OPERA-3d environment developed by Vector Field.

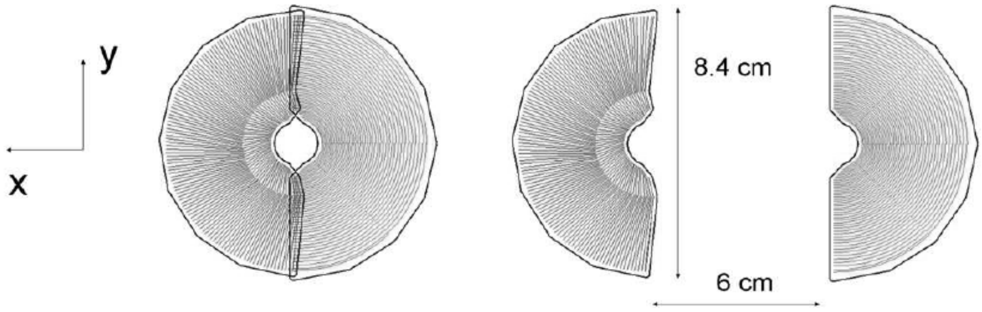

Figure 2.4: Front view diagram of the VELO detector in fully closed (*left*) and fully open (*right*) configurations [52].

concrete of the hall housing the LHCb detector.

VELO

As the name suggests, the VErtex LOcator (VELO) system [52] is designed to provide precision measurements of charged tracks near the beam interaction point, in order to correctly reconstruct detached secondary vertices typical of b- and c-hadron decays.

The VELO detector comprises 42 silicon modules along the beam direction, each consisting of a pair of half discs measuring the radial and azimuthal track coordinates respectively. These modules cover the $1.6 < \eta < 4.9$ positive pseudorapidity range, as well as some negative pseudorapidity portion to improve primary vertex[15] reconstruction, and are able to detect particles emerging from primary vertices with $|z| < 10.6\,\text{cm}$. Primary vertex resolution on the primary vertex is 10–40 µm in x and y and 50–250 µm in z, while impact parameter[16] resolution is in the 10–90 µm range. In all cases, resolutions improve when PV track multiplicity (number of tracks originating from the primary vertex) of the event increases [53].

Due to high risk of radiation damage during beam injection from the Super Proton Synchrotron (SPS) into LHC, these modules can be retracted by 3 cm in so-called *fully open* configuration, whereas during collision phase the VELO operates in *fully closed* configuration (see Figure 2.4).

Figure 2.5 shows the xz plane cross-section of the VELO modules; the two halves of the detector are z-shifted by 1.5 cm to ensure full azimuthal acceptance, resulting in the partial overlap seen in fully closed configuration.

[15] In LHCb, the *primary vertex* (PV) is the proton-proton interaction point.

[16] The *impact parameter* of a track is defined as its closest distance to the event primary vertex.

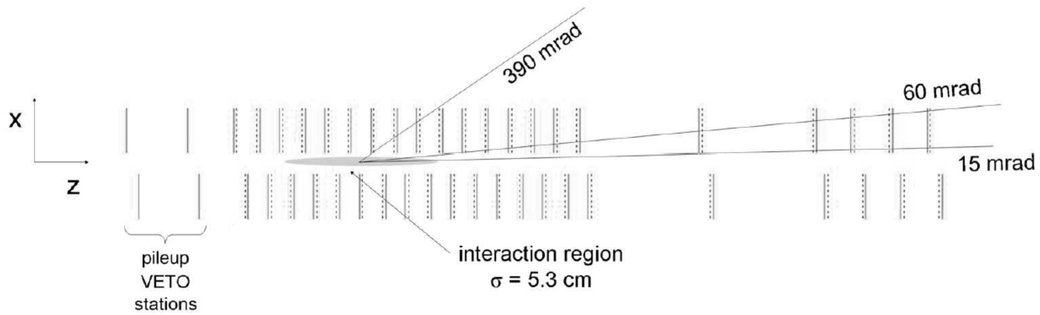

Figure 2.5: Cross-section diagram of the fully closed VELO detector in the xz plane at $y = 0$ (top view). Radial sensors are depicted as *solid* segments, azimuthal sensors as *dashed* segments [52].

Four radial-only *pile-up sensors*, part of the Level-0 hardware trigger system (see Section 2.3), are placed upstream to help veto multiple-interaction events.

Tracker Turicensis

The Tracker Turicensis (TT) [54], formerly known as Trigger Tracker, is a 150 cm × 130 cm tracking station located just upstream of the dipole magnet. Its placement serves the main purpose of tracking low-momentum particles ($|\vec{p}| \lesssim 1.5\,\mathrm{GeV/c}$) that would otherwise be bent out of the detector by the magnet without reaching the T stations.

The TT consists of four readout layers of silicon microstrip sensors arranged in a x-u-v-x configuration (vertical in the first and last layers, rotated by a stereo angle of $\mp 5°$ in the second and third layer respectively) for a total active area of $\approx 8.4\,\mathrm{m}^2$. A 200 µm strip pitch ensures a single-hit resolution $\lesssim 50\,\mu\mathrm{m}$.

The third TT layer is depicted in front view in Figure 2.6. The basic unit of a layer is the *half module*, covering half the LHCb height acceptance. Each half module consists of a row of seven sensors bonded together to form either three or two *readout sectors*. Modules near the beam pipe are of the former category, with four sensors bonded in the L sector, two in the intermediate M sector and a single sensor for the K sector closest to the beam (4–2–1 modules); other modules forgo the K sector and bond the spare sensor in the M sector (4–3 modules). Front-end readout hybrids, one for each sector, are placed at the L-end of the half modules, outside of the detector acceptance, connected directly to the L sector and indirectly to the M and K sectors via Kapton flex cables.

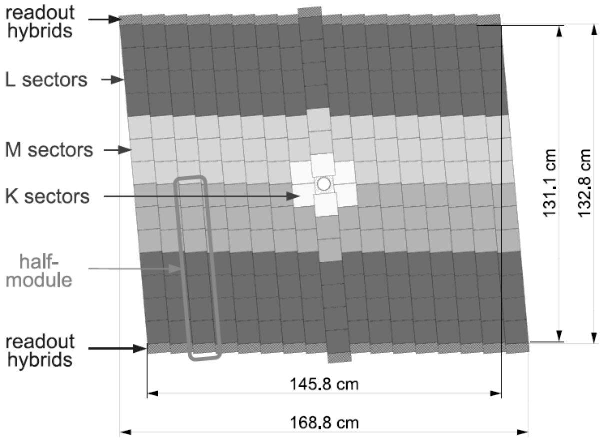

Figure 2.6: Front view of the third TT layer (different readout sectors are labeled with different shadings) [41].

T stations

The three T stations, labeled as T1–T3, are the last line of defense for LHCb tracking purposes, covering the $z \approx 7.7$–9.4 m region downstream of the dipole magnet [55]. Each T station is composed of an Inner Tracker for the region near the beam pipe and an Outer Tracker for the farther regions, as sketched in Figure 2.7.

The Inner Tracker (IT) [55] shares many similarities with the TT design, being developed in conjuction with it under the common Silicon Tracker (ST) project. Sporting the same four layers of silicon microstrips in x-u-v-x configuration, it covers a comparatively smaller $120\,\mathrm{cm} \times 40\,\mathrm{cm}$ cross-shaped surface (see Figure 2.8) for a total active area of $\approx 4\,\mathrm{m}^2$, less than half the TT. As a consequence, individual modules only include one or two sensors connected to the readout hybrids via a pitch adapter.

The much larger Outer Tracker (OT) [56] is a drift detector consisting of an array of $\mathrm{Ar/CO_2}$ straw-tube modules. Each module contains two layers of straw tubes with 4.9 mm inner diameter, ensuring a 50 ns drift time and 200 µm spatial resolution. Within a single T station, said modules are arranged in four layers in x-u-v-x configuration (see Figure 2.7a) with $\pm 5°$ vertical tilt for u and v layers respectively. The OT covers the entire 300/250 mrad LHCb detector acceptance.

Track classification and the problems with T tracks

As seen in Figure 2.9, charged particles crossing all three detector stations (VELO, TT and T1–T3) are excellently measured at LHCb, with momentum

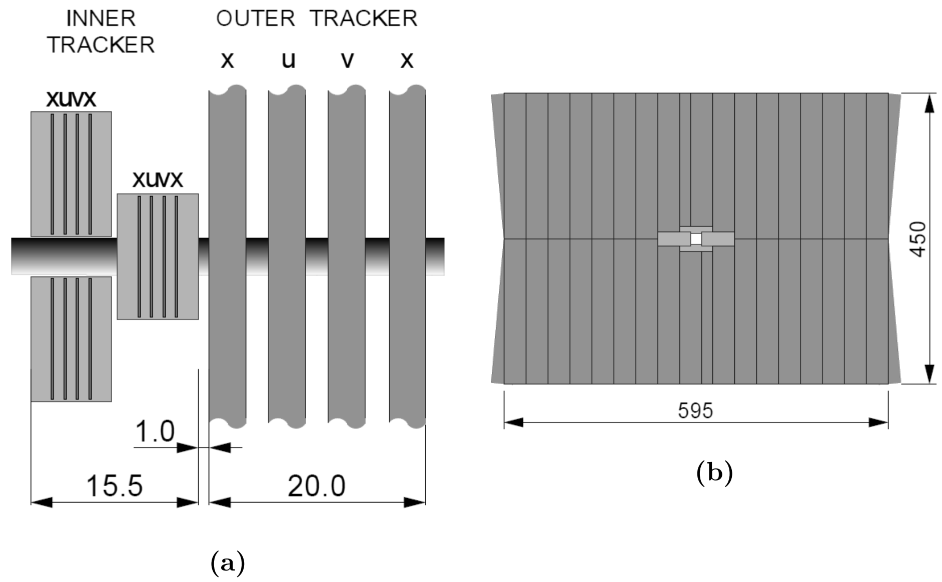

Figure 2.7: Top (*left*) and front (*right*) views of a T tracking station [55]. IT and OT are labeled with lighter and darker shades of grey respectively. Dimensions are given in cm; for the top view, lateral dimensions are not to scale.

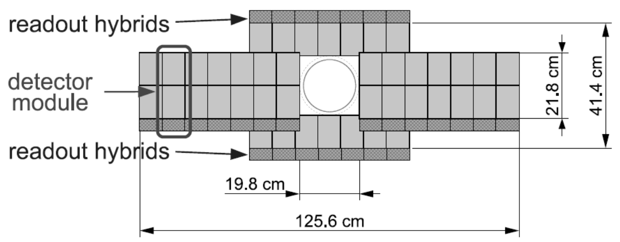

Figure 2.8: Front view of an x detector layer in the T2 Inner Tracker [41].

relative resolution going from 0.5% for low energy tracks to 1% for high energy tracks (up to 200 GeV/c) [38]. These tracks also have very high reconstruction efficiency, besting 96% in the 5–200 GeV/c momentum range [57].

However, not all particles enjoy this luxury: low momentum particles ($|\vec{p}| \lesssim 1.5\,\mathrm{GeV/c}$) are unable to reach the T stations due to the sharp magnet bending curve, while daughters of longer-lived particles with $c\tau \gtrsim 30\,\mathrm{cm}$ will miss the VELO and possibly even the TT detector.

Thus, in spite of the great efficiency, it's useful to define track categories in the LHCb working environment depending on what hits were recorded in which detectors:

- *Long* tracks are reconstructed from hits in the VELO and T stations,

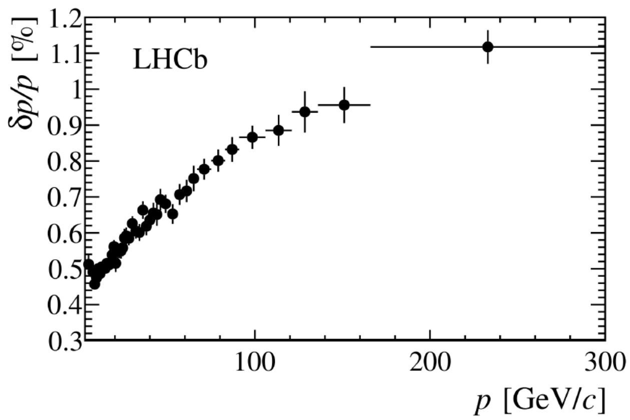

Figure 2.9: Relative momentum resolution for Long tracks as a function of $p \coloneqq |\vec{p}|$ [38].

with TT hits being optional. They are the most commonly used tracks for physics analysis in LHCb, exploiting the full performance of the detector tracking system; the long distance between VELO and T detectors means that only stable or quasi-stable charged particles can aim for this classification.

- *Upstream* tracks are reconstructed from hits in the VELO and TT detectors. As previously discussed, low-momentum particles usually fall in this category due to inability to reach the T stations.

- *VELO* tracks are reconstructed from hits in the VELO detector alone. These are often large-angle or backward tracks, valuable to correctly identify the primary vertex of the event.

- *Downstream* tracks are reconstructed from hits in the TT and T1–T3 detectors. This is the most common category to study long-lived particles (LLP) decaying after the VELO, such as Λ^0 baryons and K^0_S mesons.

- *T* tracks are only reconstructed from hits in the three T stations. Since missing both VELO and TT is a rare occurrence, these tracks largely come from LLPs with $c\tau \gtrsim 5\,\mathrm{m}$ decaying after the dipole magnet.

Sketches of tracks satisfying the above requirements are depicted in Figure 2.10.

Among the four, T tracks have seen the least use over LHC Runs 1 and 2. The main reason is related to their key property of only having measured constraints after the magnet: in order to reconstruct their origin vertex, T tracks have to be extrapolated through several meters of intense magnetic field,

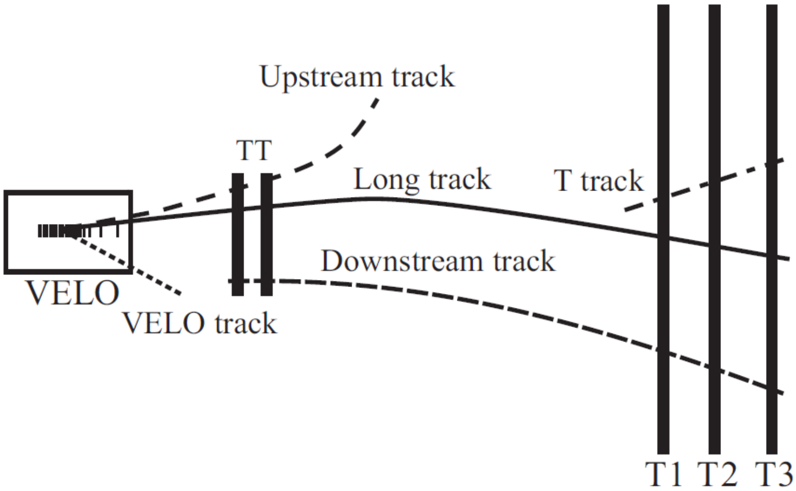

Figure 2.10: Side view diagram of the LHCb tracking systems for LHC Runs 1 and 2 with sketched examples of the main track classification categories.

an operation that has ripercussions in terms of both accuracy and timing. On top of that, the further a charged particle is produced after the dipole magnet, the less the residual magnetic field will be able to imprint a significant bending radius, negatively affecting the momentum resolution at T station level.

Over the ten years of detector operation there has been little physics incentive to fix or mitigate these issues, as most decaying particles relevant to LHCb can already be studied using Long and Downstream tracks. The Λ^0 EDM/MDM measurement proposal outlined in Section 1.4 is one of the atypical cases where T tracks are downright essential, since the technique hinges on the measurement of the spin precession of the baryon traversing the magnetic field before decaying in the $p\pi^-$ pair. Over the course of the following chapters, I'll delve into more detail on the approaches adopted to overcome the problems associated with T tracks in view of competitive measurements of the Λ^0 electromagnetic dipole moments.

2.2.2 Particle identification

While tracking outgoing particles is obviously of paramount importance for physics analysis, knowledge of *what* particles are being tracked is also crucial. The ability to distinguish protons, pions and kaons is of particular interest at LHCb due to its research objectives in CP violation and b physics, requiring precise flavour tagging and physical background rejection. For the above reasons, a complex ecosystem of detectors dedicated to particle identification (PID) is in place.

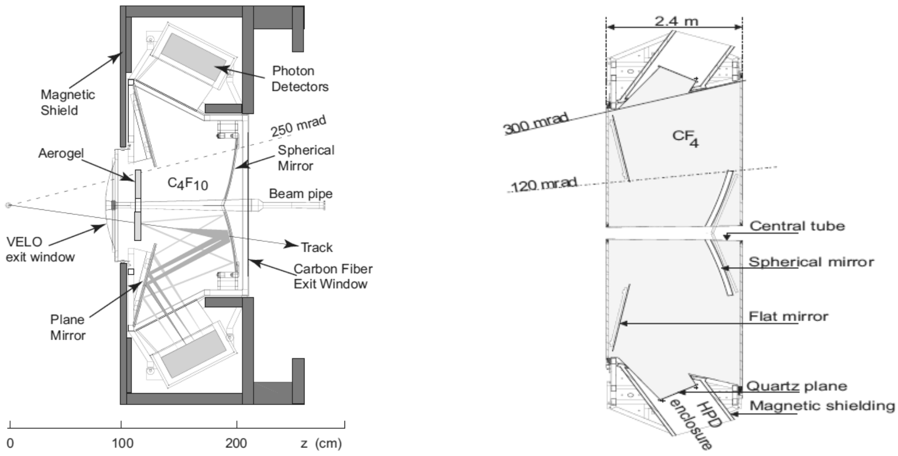

(a) **(b)**

Figure 2.11: Top view of the RICH 1 (*left*) and RICH 2 (*right*) detectors [41].

RICH

Roughly 90% of pions, protons and kaons from B meson decays have momentum in the 2–150 GeV/c range [57]. Since their momentum distributions depend on the polar angle of production, LHCb employs two Ring Imaging CHerenkov (RICH) detectors [58] to cover the full momentum range for these particles.

The RICH 1 detector, sketched in Figure 2.11a, is located upstream of the dipole magnet, wedged between the VELO and TT tracking detectors. The detector exploits the different spectra of Cherenkov angles as a function of momentum for different kinds of particles. During Run 1, RICH 1 used two radiator materials: an aerogel layer ($n = 1.03$) and a C_4F_{10} gas layer ($n = 1.0014$). This allowed RICH 1 to perform π/K identification in the 1–60 GeV/c range. Due to occupancy problems, the silica aerogel radiator providing identification in the low momentum range $|\vec{p}| \lesssim 10\,\text{GeV/c}$ was removed for Run 2; since the kaon Cherenkov threshold in C_4F_{10} is $\approx 9.7\,\text{GeV/c}$, they can still be identified by operating RICH in so-called *kaon veto mode*, whereby kaons are marked by the lack of Cherenkov light [57] [59]. RICH 1 covers from 25 mrad (lower limit imposed by the beryllium beam pipe section) up to the full LHCb acceptance.

Acting as complement to its partner, RICH 2 (Figure 2.11b) operates downstream of the T tracking stations and is optimized for a high momentum range, providing PID from $\approx 15\,\text{GeV/c}$ up to and beyond $100\,\text{GeV/c}$. Its lower limit of acceptance is $\approx 15\,\text{mrad}$, dictated by the required clearance of 45 mm around the beam pipe.

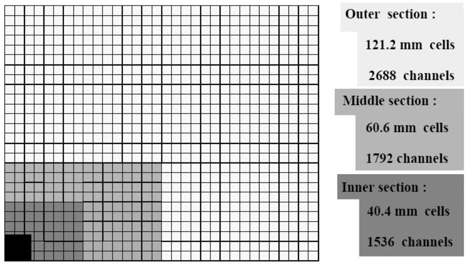

(a)

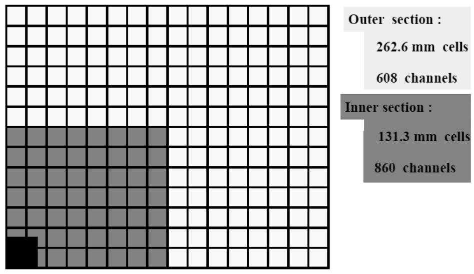

(b)

Figure 2.12: Front view of the lateral segmentation of SPD/PS and ECAL (*left*) and HCAL (*right*) calorimeters [41]. Only a quarter of the detector is depicted. Dimensions are given for the ECAL in the left figure.

Calorimeter

The LHCb calorimeter system [60] serves the dual purpose of identifying hadrons, electrons and photons and measuring their energies. Its design follows the standard high energy physics approach of an electromagnetic calorimeter (ECAL) for the detection of electrons and photons, followed by a hadronic calorimeter (HCAL) for the detection of charged and neutral hadrons.

Placed at 12.5 m from the beam interaction point, the ECAL employs a shashlik layout[17], alternating layers of absorber (2 mm thick lead) and sampler (4 mm thick polystyrene scintillator tiles) perpendicular to the beam axis. Due to the steep dependence of hit density from the distance from the beam pipe, the calorimeter adopts a variable cell size and is segmented in three distinct sections outlined in Figure 2.12a. The ECAL is approximately $25X_0$ long, with X_0 being the radiation length; this allows for the full containment of electromagnetic showers from high energy photons, which is of paramount importance for energy resolution.

Electron detection is particularly tricky due to the significant pion background, both of the charged and neutral variety. To combat this, two ancillary detectors are located upstream of the ECAL proper: the scintillator pad detector (SPD) selects charged particles to veto π^0, while the preshower detector (PS) rejects $\pi^\pm$. Collectively, the SPD/PS detectors consist of two scintillator pads enclosing a 15 mm thick lead plate with a $7.6\,\mathrm{m} \times 6.7\,\mathrm{m}$ sensitive area. Transverse segmentation is designed to projectively match the ECAL segmentation down to the individual cell size.

[17]The nomenclature references the *shashlik*, or *šašlyk*, a traditional meat dish consisting of skewers threaded with alternating pieces of meat, fat and vegetables. The dish is popular throughout the Caucasus and Central Asia regions, including the former Soviet Union, where the shashlik calorimeter technology was first developed.

The HCAL is a sampling calorimeter as well, employing iron as absorber and scintillating tiles as active material. In contrast to the ECAL and SPD/PS detectors, however, the scintillating tiles run parallel to the beam axis, interspersed with 1 cm thick layers of iron; meanwhile, the longitudinal structure alternates scintillating tiles with iron spacers, both of length $\lambda_I \approx 20\,\text{cm}$, λ_I being the hadron interactiorn length in steel. The transvese segmentation of the detector, sketched in Figure 2.12b, envisages one less section and a comparatively larger cell size than ECAL, owing to the differing sizes of electromagnetic and hadronic showers. Since competitive hadron energy resolution does not require full containment of the shower, the HCAL only extends for ≈ 5.6 interaction lengths.

In all four subdetectors, scintillating light is conveyed through wavelength-shifting fibres to photomultiplier tubes for conversion and magnification; due to the lower light yield of HCAL modules, their phototubes operate at a higher gain.

Muon system

The final components of the PID system are the five muon stations M1–M5 [61], providing trigger and limited tracking for muons in LHCb. Stations M2–M5 are placed downstream of the calorimeter system, separated from each other by 80 cm of iron; these absorber layers select muons on the basis of penetration, with a 6 GeV/c momentum threshold required to cross the fifth station. The lone M1 station precedes the calorimeter system with the goal of improving transverse momentum measurement. The muon system provides acceptance in the 20–306 mrad region in the bending plane and 16–258 mrad region in the non-bending plane, in line with the global LHCb acceptance.

A side view diagram of the muon system is depicted in Figure 2.13: each station is divided in four R1–R4 regions with increasing distance from the beam pipe. While transverse spatial resolution progressively worsens in outer regions, the growing influence of large angle multiple scattering means it would be limited anyway.

The most sensitive area is the R1 region of the M1 station, since the large particle flux imposes strict limits on radiation hardness to prevent ageing effects during the LHC projected lifetime. For this reason the M1-R1 region alone employs gas electron multiplier foils, while the remainder of the muon system consists of multi-wire proportional chambers with a $Ar/CO_2/CF_4$ gas mixture.

Overall, the five stations combined cover a total area of $435\,\text{m}^2$. Stations M1–M3, by virtue of their high spatial resolution along the x coordinate, are used to determine the direction of the candidate muon track and compute

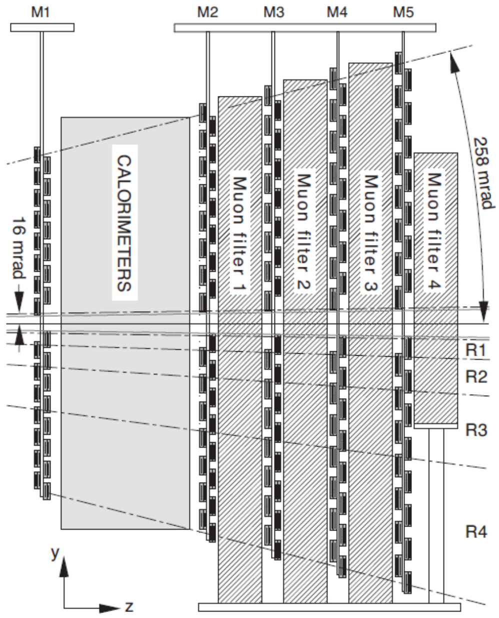

Figure 2.13: Side view diagram of the muon system [41].

the transverse momentum with $\approx 20\%$ resolution; stations M4–M5 have lower performance on this front and their contribution mainly consists in the identification of highly penetrating particles.

2.3 The LHCb data flow

Considering the complexity of the LHCb detector environment, as seen in Section 2.2, it should come to no surprise that the data elaboration process is equally multifaceted. Figure 2.14 sketches the data flow approach during LHC Run 2; while a full discussion of the mechanics is beyond the scope of this thesis, this section aims to provide a basic understanding of the different steps in order to grasp key concepts relevant to the following work.

2.3.1 Trigger

The trigger system [62] provides the first triage of all data recorded by the LHCb detector. LHC collides proton-proton bunches at a nominal 40 MHz rate, with $\approx 1\%$ resulting in $b\bar{b}$ events of interest for LHCb. Furthermore, only $\approx 15\%$ of these events will produce a reconstructible b hadron (i.e. with all decay products within the detector acceptance) [57], and studies on topics such as CP violation are likely to require decays with small ($\lesssim 10^{-3}$) branching

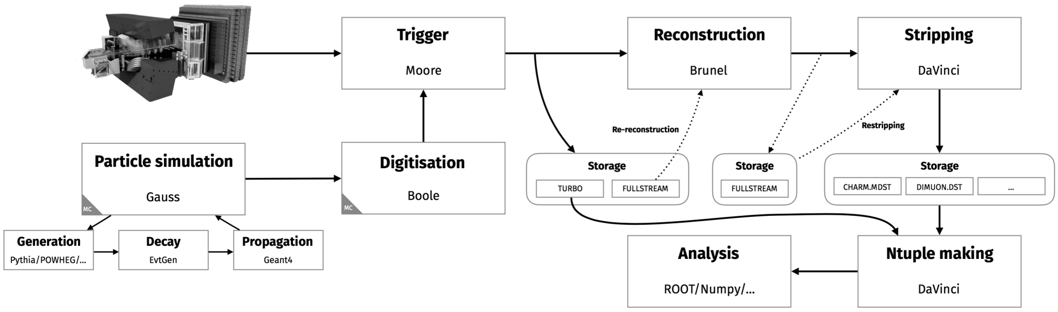

Figure 2.14: Diagram of the LHCb Run 2 data flow.

ratios. Peak writing speeds for data storage are in the order of a few kHz, making it impossible to save all information even forgoing the high costs this would entail in terms of storage space. The LHCb trigger system therefore has to skim out the vast majority of uninteresting events with high efficiency, and it needs to be fast about it.

The trigger system employed during LHC Runs 1 and 2 can be broken down into three distinct phases, or *levels*. First comes Level-0 (L0), which is implemented directly on hardware via custom-made electronics. Working synchronously with the 40 MHz bunch-crossing rate, the L0 trigger is only able to read three parts of the LHCb detector independently: the VELO pile-up radial modules, used to reject events with multiple primary proton-proton interactions; the calorimeter trigger (L0-Calorimeter), which selects hadron, photon and electron candidates; and the muon trigger (L0-Muon), which obviously selects muons.

The L0-Calorimeter trigger is based on information from all four subdetectors of the calorimeter system (SPD, PS, ECAL and HCAL) and uses it to compute the transverse energy E_{T} deposited by incoming particles. Events with a large number of charged tracks are vetoed based on the number of hits in the SPD to manage the limited computation time allotted for the subsequent trigger levels. Based on the E_{T} measurement, the trigger builds hadron, electron and photon candidates.

Each of the four L0-Muon trigger processors selects the two highest p_{T} tracks from its assigned quadrant among candidates crossing all five muon stations. The single muon trigger sets a threshold on the highest transverse momentum p_{T} of the pair, while the dimuon trigger does so on the product of p_{T} of both candidates.

After combining all information, the L0 trigger outputs at a maximum rate of 1 MHz fixed by front-end electronics, the majority being used for muon and hadron triggers (electrons and photons only take up $\approx 15\%$ of the L0 output rate). These data are then sent to the event filter farm (EFF), where the software-based high level trigger (HLT) algorithms, implemented in the Moore application, process them to further reduce the rate for storage: the first stage (HLT1) gets the rate down to 100 kHz, while the second (HLT2) outputs at roughly 12.5 kHz. Both HLTs are divided in independently operating *trigger lines*, each line consisting of specific selection instructions for a determined class of events.

HLT1 reconstructs charged particles with $p_{\mathrm{T}} > 500\,\mathrm{MeV}$, starting with Long tracks. First it combines VELO hits to form straight line tracks, then it looks for ≥ 3 TT hits in a region around the straight line extrapolation of the VELO tracks. The small upstream portion of magnetic field allows for momentum determination with a 20% resolution used to reject low-p_{T} tracks. After that, the tracks are extrapolated at the T stations, looking for hits in IT and OT on one side of the straight line VELO-TT extrapolation (depending on the charge estimate). Other track types are fit with the same general approach: Downstream tracks start with T1–T3 segments and look for matching hits in the TT, Upstream tracks follow the Long track process but require incompatibility with T station hits, and T tracks are reconstructed last using T1–T3 segments that didn't match any previous track types. All tracks are fit with a Kalman filter with a simplified detector geometry; at this stage, particle identification is only possible for muons on account of the tight timing constraints.

Owing to the rate reduction performed by HLT1, HLT2 is able to reconstruct the entire event: reconstruction of charged tracks with $p_{\mathrm{T}} > 80\,\mathrm{MeV}$ is performed using all tracking sub-detectors (see Section 2.2.1), along with reconstruction of neutral clusters and implementation of the full particle identification system (Section 2.2.2).

2.3.2 From reconstruction to analysis

The data flow reaches a fork after HLT2. While the trigger output can be used for data analysis, the hectic timing requirements for said phase mean that only information on the decay of interest for the related HLT2 trigger line is reconstructed, leaving the rest as raw data.

The *full stream* branch rectifies this by performing a slower-paced, offline re-reconstruction of the full decay tree controlled by the Brunel application. Resulting data are saved in Data Summary Tape (DST) format, with a single event occupying $\approx 150\,\mathrm{kB}$ of space. These DST files undergo the *stripping* process, carried out by the DaVinci application: this applies dedicated loose selection algorithms (*stripping lines*) and groups events in *streams* (the dimuon stream for $\mu^+\mu^-$ events, for instance) to ease access for data analysis.

The resulting DST files, also referred to as *full* DSTs to distinguish from *reduced* DSTs output by Brunel, can then be processed by the end user through DaVinci to apply their own filter algorithms and extract ROOT nTuples[18] suitable for physics studies.

During Run 1, the full stream path was the only one available, because HLT2 performed a significantly worse reconstruction than Brunel even on the implemented decays. This changed in Run 2 with the introduction of the parallel *Turbo stream* [64], i.e. the storage of HLT2 output for direct usage by analysts through DaVinci. The EFF upgrade conducted during the LS1 increased the HLT2 allotted computation time enough to match Brunel performances; the key difference between the full and turbo streams is that the latter only saves information on the decay of interest for the related HLT2 trigger line to save storage space, preventing future offline reconstruction of the full decay tree by Brunel.

This change was motivated by the increase in center-of-mass collision energy from 8 TeV to 13 TeV: the higher b- and c-production cross-sections mean that more events of interest for LHCb are produced in Run 2 despite the same bunch-crossing frequency. The Turbo stream allows more saved data to be ready for analysis, while the slower Brunel offline process fulfills the need for reconstruction of decays outside of those implemented in HLT2 trigger lines.

2.3.3 Monte Carlo simulations

The comparison between experimental results and theory predictions is a critical aspect of physics analysis. In the case of high-energy physics experiments, the latter rely on the correct simulation of events from collision to detector interaction.

In LHCb, the production of Monte Carlo (MC) data is controlled by the Gauss application, which is in charge of coordinating the several cogs of the simulation machine: proton-proton collisions are simulated via MC generator software such as Pythia [65] and POWHEG [66]; the decay of generated particles is described by EvtGen [67], while the Geant4 toolkit [68] simulates the propagation and interaction with the material using a detailed modelization of the LHCb detector.

As the final step, the simulated hits from the virtual detector in Geant4 are digitized using the Boole application, which aims to mimic the real output from the LHCb detector. This allows simulated data to be processed with the

[18]ROOT [63] is an C++ open-source data analysis toolkit developed developed at CERN and popular within the high-energy physics community. A key feature of ROOT is the `TTree` class (*tree* for simplicity), a C++ object container organized in independent *branches*, or *columns*, and optimized for large data sets. The `TNtuple` class is a `TTree` with float variables only.

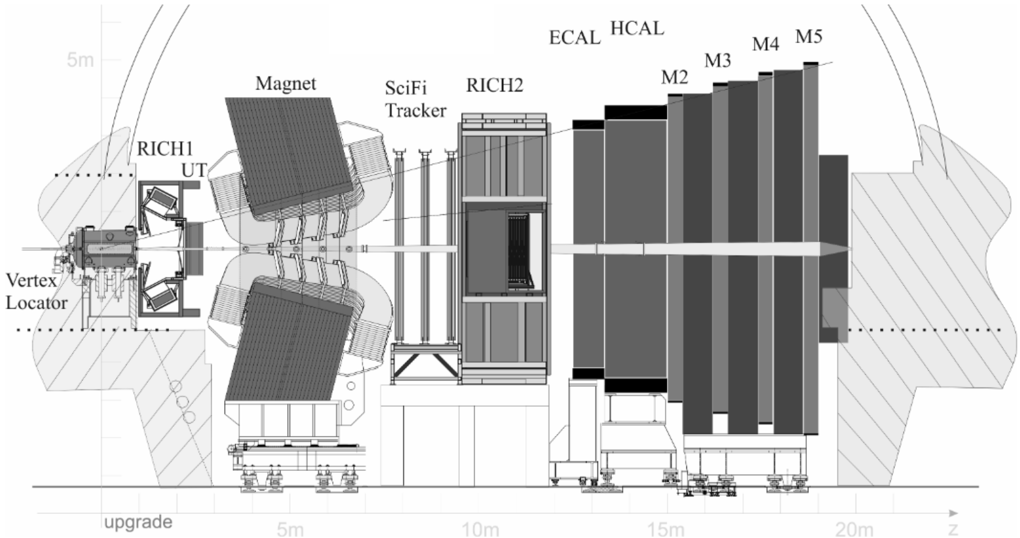

Figure 2.15: Side view of the upgraded LHCb detector for future usage in LHC Run 3 [69].

same software as the real one, as described in the earlier paragraphs of this section.

2.4 LHCb detector upgrade for Run 3

During LHC Runs 1 and 2, the LHCb experiment has collected $\approx 9\,\mathrm{fb}^{-1}$ of data. As much as this has allowed the LHCb Collaboration to achieve impressive results in the heavy-flavour sector and beyond, as touched upon in Section 2.2, many ongoing analyses are still limited by low statistics. For this reason, during the LS2, work has been carried out to upgrade the detector in software and hardware with the goal of reaching a $25\,\mathrm{fb}^{-1}$ integrated luminosity by the end of Run 3 [69].

The main feature of this upgrade will be the removal of the L0 hardware trigger in favour of a fully software trigger [70]. After the performance match between HLT2 and Brunel achieved in Run 2, the high level trigger will see an even more central stage in Run 3, being tasked with full reconstruction of all events of interest in the context of a five-fold increase in operational luminosity (up to $2 \times 10^{33}\,\mathrm{cm}^{-2}\,\mathrm{s}^{-1}$). To prevent trigger yield saturation with such an increase in luminosity, the LHCb readout rate will be augmented from the current 1 MHz to the LHC bunch crossing rate of 40 MHz.

Many parts of the LHCb detector will concurrently be upgraded or partially rebuilt, as seen in Figure 2.15, with the most significant changes concerning the tracking system. The upgraded VELO, also known as VELO Pixel, will replace the silicon microstrip technology with hybrid pixel modules with integrated CO_2 cooling, ensuring better radiation hardness, impact parameter resolution and tracking times [71]. Upstream of the magnet, the Upstream Tracker (UT) will take over from the TT, featuring four high granularity silicon microstrip layers with improved coverage of the LHCb angular acceptance. Finally, both inner and outer trackers of the T1–T3 stations will be replaced by the Scintillating Fiber Tracker (SFT or SciFi), based on 2.4 m plastic scintillating fibers read out by silicon photo-multipliers [72]. This global upgrade is projected to reduce reconstructed fake tracks by as much as 70%, drastically shortening trigger timing [69].

The PID system will also undergo modifications, albeit less substantial ones [73]. Current hybrid photon detectors used in the RICH system cannot be disentangled from the embedded readout electronics operating at 1 MHz and will thus be replaced by commercial multianode photomultipliers; the optical layout of RICH1 will also be updated to spread gas rings over the entire detector plane, reducing particle occupancy problems[19]. Whereas the calorimeter system will largely stay the same, muon station M1 will be removed and additional shielding will surround the beam pipe in the M2 region to improve radiation hardness.

2.5 Data used for this thesis

In the following chapters of this thesis, I will employ data collected during LHCb Run 2, corresponding to an integrated luminosity of $6\,\mathrm{fb}^{-1}$, to conduct studies related to the measurement of the Λ^0 baryon electromagnetic dipole moments pursuing the approach described in Section 1.4. The exclusive decay chosen for the analysis is the Λ_b^0 channel

$$\Lambda_b^0 \to J/\psi\ (\to \mu^+\mu^-)\ \Lambda^0\ (\to p\pi^-), \tag{1.45 revisited}$$

exploiting the $\approx 100\%$ longitudinal polarization of the Λ^0. This comparatively rare channel (BR $\approx 10^{-5}$) is selected at HLT level via the inclusive $J/\psi \to \mu^+\mu^-$ detached[20] trigger line. The need to measure spin precession in the magnetic field restricts the available Λ^0 to those decaying after the LHCb dipole magnet, implicitly requiring its decay products $p\pi^-$ to be T tracks.

[19] This is an issue specific to RICH1, being much closer to the interaction point than its downstream counterpart.

[20] The *detached* requirement adds a selection criterium on the muon impact parameters, enforcing their incompatibility with the lowest-χ^2 primary vertex.

The $\tau \approx 1.5 \times 10^{-12}\,\mathrm{s}$ mean life of the Λ_b^0 [3] places its decay vertex well inside the VELO detector; in conjunction with the high efficiency reconstruction of muons in LHCb, this justifies a Long track requirement in their case. The Λ_b^0 vertex accuracy afforded by the J/ψ half of the decay chain enables us to impose kinematic constraints on the Λ^0, partially offsetting some of the problems with T tracks I have pointed out in Section 2.2.1.

Along with Run 2 data, simulated samples of (1.45) events are used to study the effect of the different steps of signal selection requirements. These have been generated with Pythia [65] using the LHCb-specific configuration implemented in Gauss [74], and have been digitized following the procedure detailed in Section 2.3.3.

Chapter 3

Λ_b^0 and Λ^0 decay vertex reconstruction

This chapter details my work towards the improvement of the vertex reconstruction process for decays involving T tracks. Section 3.1 delves into a deep study of the vertexing process at LHCb and the two algorithms employed in this thesis; Section 3.2 introduces the problem of low vertexing efficiency for the decay of interest $\Lambda_b^0 \to J/\psi\,\Lambda^0$; Section 3.3 presents my efforts in the characterization of decays with failed vertex fit in search for the root cause of the non-convergence; Section 3.4 proposes my solution to improve the signal yield through partial recovery of non-reconstructed events; finally, Section 3.5 features an analysis of $\Lambda^0 \to p\pi^-$ decay vertex resolution in the simulated signal dataset and a description of the main known sources of bias. Section 3.6 provides a short summary of the main results obtained in the chapter.

3.1 Vertex reconstruction algorithms at LHCb

3.1.1 Vertex Fitter algorithm

The Vertex Fitter (VF) [75], implemented as part of the LoKi analysis toolkit, is the main vertexing algorithm used for the reconstruction of the Λ_b^0 decay.

Under VF formalism, each daughter particle is represented by a 7-dimensional vector[21]

$$\vec{p} = \begin{pmatrix} \vec{r} \\ \vec{q} \end{pmatrix} = \begin{pmatrix} r_x \\ r_y \\ r_z \\ p_x \\ p_y \\ p_z \\ E \end{pmatrix}, \tag{3.1}$$

containing its 4-momentum $\vec{q}$ computed at a certain reference point $\vec{r}$. Parameter vector $\vec{p}$ has an associated covariance matrix V, which can be written in block structure as

$$V = \begin{pmatrix} V_r & V_{rq} \\ V_{rq}^T & V_q \end{pmatrix}. \tag{3.2}$$

It is also convenient to identify its formal inverse matrix $G := V^{-1}$, which has an analogous block form:

$$G = \begin{pmatrix} G_r & G_{rq} \\ G_{rq}^T & G_q \end{pmatrix} = \begin{pmatrix} V_r & V_{rq} \\ V_{rq}^T & V_q \end{pmatrix}^{-1}. \tag{3.3}$$

Taking the daughter particles as inputs, the Vertex Fitter returns the best fit value $\vec{x}$ for the common origin vertex, along with its covariance matrix C and the χ^2 which can be used to evaluate the goodness of fit.

The algorithm builds the decay tree from the bottom up via a «leaf-by-leaf» approach, fitting one vertex at a time (e.g. $J/\psi \to \mu^+\mu^-$, $\Lambda^0 \to p\pi^-$) and then moving upwards (e.g. $\Lambda_b^0 \to J/\psi\,\Lambda^0$). The process is blind to the downstream leaves and only considers kinematic information of the immediate daughter particles, without accounting for momenta and mass constraints throughout the decay tree.

Iterating paradigm

The basic unit of recursion of the Vertex Fitter is the *iteration*: the algorithm is set to repeat the vertexing process until either a convergence condition is satisfied (see later) or the fit reaches the set number of allowed iterations, 10 by default. In the latter case, a non-convergence error is thrown and the candidate event is discarded.

[21] This chapter assumes the standard right-handed LHCb coordinate system, see Section 2.2.

At the beginning of each iteration, the final vertex covariance matrix C_n^{i-1} from the previous iteration[22] is shrinked by a factor $s^2 = 10^{-4}$ to decrease its relative importance in further vertex computations:

$$C_0^i = C_n^{i-1} \times s^2. \tag{3.4}$$

The algorithm then performs a *proper transportation*, a dedicated routine in which all daughter particles are extrapolated to the z component of the current (tentative) position of the common production vertex $\vec{x}_n^{i-1}$.

As mentioned in Section 2.2.1, extrapolation using T tracks is a sensitive affair: unlike the case for other track types, no constraints are available besides the downstream measurement performed by the T tracking stations, meaning the tracks have to be propagated through several meters while accounting for the intense and non-homogeneous LHCb magnetic field $\vec{B}$. For this analysis, said extrapolation was performed via numerical solution of the track propagation equations using an approach based on the Runge-Kutta (RK) method [76]. In the RK formalism, the track state at a given z is parameterized with a five-dimensional representation

$$\vec{x} = \begin{pmatrix} x \\ y \\ t_x \\ t_y \\ \frac{Q}{P} \end{pmatrix}, \tag{3.5}$$

with $t_x := \frac{dx}{dz}$ (the same holds for t_y) and $\frac{Q}{P}$ is the charge-to-momentum ratio. When extrapolating the track for a distance Δz, the new track state is computed with a fifth-order RK expansion

$$\vec{x}(\Delta z) = \vec{x}_0 + \sum_{m=1}^{6} c_m \frac{d\vec{x}^m}{dz} \Delta z, \tag{3.6}$$

with

$$\vec{x}^m = \sum_{n=1}^{m-1} b_{mn} \frac{d\vec{x}^n}{dz} \Delta z \tag{3.7}$$

and Cash-Karp parameters c_m and b_{mn} chosen to obtain a precision of $(\Delta z)^6$ [77]. The higher Δz accuracy makes this technique more suitable for T track propagation in the high-$\vec{B}$ region with respect to the parabolic extrapolation commonly used in LHCb.

[22] The subscript n identifies the final step number, see later.

Step

Within an individual iteration i, denoted by a superscript, the Vertex Fitter algorithm proceeds by *steps* denoted by subscripts, with each step k coinciding with the addition of the k-th daughter particle.

Given information on the vertex position $\vec{x}_{k-1}$ obtained using the first $k-1$ particles, track k is added through the following recursive procedure. First the inverse vertex covariance matrix is updated:

$$(C_k^i)^{-1} = (C_{k-1}^i)^{-1} + (G_k^i)_r \tag{3.8}$$

where the reference point inverse covariance matrix $(G_k^i)_r = (V_k^i)_r^{-1}$ has been updated at the beginning of the iteration as part of the the proper transportation.

If $(C_k^i)^{-1}$ can successfully be inverted, the algorithm updates the current best estimate of the common origin vertex by combining information from the previous step ($\vec{x}_{k-1}^i$) with information from the properly transported current particle (reference point $\vec{r}_k^i$ from representation (3.1)) through the associate inverse covariance matrices:

$$\vec{x}_k^i = C_k^i \left[(C_{k-1}^i)^{-1} \vec{x}_{k-1}^i + (G_k^i)_r \vec{r}_k^i \right]. \tag{3.9}$$

New vertex $\vec{x}_k^i$ doubles as reference point for the k-th particle until the next transportation, ergo track momentum is also updated to match it[23]

$$\vec{q}_k^i \coloneqq \vec{q}_k^i - (V_k^i)_{rq} (G_k^i)_r \left(\vec{r}_k^i - \vec{x}_k^i \right). \tag{3.10}$$

To conclude the step, the vertex χ^2 is updated to the account for the new position:

$$\begin{aligned} (\chi^2)_k^i = {} & (\chi^2)_{k-1}^i \\ & + \left(\vec{r}_k^i - \vec{x}_k^i \right)^T (G_k^i)_r \left(\vec{r}_k^i - \vec{x}_k^i \right) \\ & + \left(\vec{x}_k^i - \vec{x}_{k-1}^i \right)^T (C_{k-1}^i)^{-1} \left(\vec{x}_k^i - \vec{x}_{k-1}^i \right) \end{aligned} . \tag{3.11}$$

The two new terms quantify the χ^2 increase due to the displacement of the current vertex with respect to the two previous positions it was computed from, as seen in (3.9).

Seeding

The recursive procedure requires, at each step, a previous estimated vertex position $\vec{x}_{k-1}^i$, an associated inverse covariance matrix $(C_{k-1}^i)^{-1}$ and a $(\chi^2)_{k-1}^i$. In particular, step $k = 1$ demands the existence of $\vec{x}_0^i$, $(C_0^i)^{-1}$ and $(\chi^2)_0^i$.

[23]In this equation, $\coloneqq$ stands for the assignment operator.

For iterations $i > 1$, such roles are filled by the final vertex computed during the previous iteration. This leaves out the crucial $i = 1, k = 1$ step; to make up for it, at the beginning the algorithm extracts a *vertex seed*, a first estimate of the decay vertex position, through a dedicated procedure depending on decay topology and properties of particles involved.

In the case of interest of the $\Lambda^0 \to p\pi^-$ two-body decay, said procedure is a single simplified iteration that uses the initial $\vec{p}$ track measurement performed by the T stations:

$$(C_0^1)^{-1} = \sum_{j=p,\pi} G_{rj}, \tag{3.12a}$$

$$\vec{x}_0^1 = C_0^1 \sum_{j=p,\pi} G_{rj}\vec{r}_j. \tag{3.12b}$$

Update of momenta is handled in the same way as equation (3.10). A new χ_0^2 is computed for each particle:

$$(\chi^2)^1_{0(p)} = \left(\vec{r}_p - \vec{x}_0^1\right)^T G_{rp} \left(\vec{r}_p - \vec{x}_0^1\right), \tag{3.13a}$$

$$(\chi^2)^1_{0(\pi)} = \left(\vec{r}_\pi - \vec{x}_0^1\right)^T G_{r\pi} \left(\vec{r}_\pi - \vec{x}_0^1\right), \tag{3.13b}$$

conventionally choosing $(\chi^2)^1_0 \coloneqq (\chi^2)^1_{0(p)}$.

Termination and smoothing

The two VF convergence conditions are both based on comparisons between the vertex position computed at the end of the current iteration with the one from the previous iteration, with convergence being called if either one of them is satisfied.

The first condition is placed on the absolute distance between the vertices:

$$\left\|\vec{x}_n^i - \vec{x}_n^{i-1}\right\| \leq d_1 \tag{3.14}$$

where $d_1 = 1\,\mu\text{m}$ by default. The second condition, by far the one more commonly satisfied when reaching convergence using T tracks[24], concerns vertex distance «in χ^2 units»:

$$\left(\vec{x}_n^i - \vec{x}_n^{i-1}\right)^T (C_n^i)^{-1} \left(\vec{x}_n^i - \vec{x}_n^{i-1}\right) \leq d_2 \tag{3.15}$$

with $d_2 = 0.01$. While condition (3.14) can be satisfied at any point in the vertexing process, (3.15) additionally requires $i > 1$, excluding the very first iteration.

[24]This doesn't happen using Long tracks, suggesting that the $d_1 = 1\,\mu\text{m}$ threshold is too strict given the scale of uncertainties in T station measurements. Nevertheless, increasing d_1 does not improve the vertex reconstruction efficiency discussed in Section 3.2.

When convergence is reached at iteration N, the algorithm applies a smoothing process: for each daughter particle k, the reference point $\vec{r}_k$ is fixed to the final vertex position $\vec{x}_n^N$ and momentum $\vec{q}_k$ is updated accordingly as

$$\vec{q}_k = \vec{q}_k^N - (V_k^N)_{rq} (G_k^N)_r \left(\vec{r}_k^N - \vec{x}_n^N \right), \tag{3.16}$$

with $\vec{r}_k^N$ being the last computed reference point with related $\vec{q}_k^N$.

Last comes the evaluation of the relevant covariance matrices. The vertex covariance matrix C is obviously fixed at C_n^N; the algorithm also computes for each entry the correlation matrix $E_k \coloneqq \mathrm{corr}\left(\vec{x_n^N}, \vec{q}_k \right)$ between the vertex position and the particle momentum

$$E_k = -F_k C, \tag{3.17}$$

and the particle $\vec{q}_k$ covariance matrix

$$D_k = (V_k^N)_q - (V_k^N)_{rq} (G_k^N)_r (V_k^N)_{rq}^T + F_k C F_k^{-1}, \tag{3.18}$$

with

$$F_k = -V_{rq_k} V_{r_k}^{-1} \tag{3.19}$$

being an auxiliary matrix.

Mother particle creation

Assuming the found vertex is inside the LHCb fiducial volume, the fit is validated and a χ^2 is determined by taking the last step value from (3.11) and adding the χ^2 from any short-lived daughter particle. Degrees of freedom (DOFs) for χ^2 reduction are computed as follows:

- each track contributes 2 DOFs;
- each ρ^+-like particle[25] contributes 2 DOFs;
- each sub-vertex contributes 3 DOFs plus further DOFs from the downstream decay tree;
- the sum total is reduced by 3.

[25] A ρ^+-like particle is a particle resulting from the combination of 1 long-lived particle and ≥ 2 photons. The category identifier is owed to the topology of the $\rho^+ \to \pi^+\pi^0$ decay with $\pi^0 \to \gamma\gamma$.

A mother particle is subsequently created using the (3.1) representation with reference point $\vec{x}_{\text{mother}}$ fixed to the new-found vertex coordinates. Its 4-momentum is computed as a simple sum of the 4-momenta of its daughters extrapolated at the vertex:

$$\vec{q}_{\text{mother}} = \sum_{k \in \text{daughters}} \vec{q}_k. \tag{3.20}$$

The parameter vector covariance matrix (3.2) is determined as follows:

$$V_r^{\text{mother}} = C, \tag{3.21}$$

$$V_q^{\text{mother}} = \sum_{k \in \text{daughters}} \left[D_k + \sum_{\substack{j \in \text{daughters} \\ j \neq k}} \left(F_k C F_j^T + F_j C F_k^T \right) \right], \tag{3.22}$$

$$V_{rq}^{\text{mother}} = \sum_{k \in \text{daughters}} E_k, \tag{3.23}$$

with D_k, E_k and F_k for each daughter resulting from (3.18), (3.17) and (3.19) respectively.

Finally, the mother particle measured mass M_{mother} is computed as magnitude of 4-vector $\vec{q}_{\text{mother}}$ in the $(-,-,-,+)$ metric

$$M_{\text{mother}} = \sqrt{E^2_{\text{mother}} - p_x{}^2_{\text{mother}} - p_y{}^2_{\text{mother}} - p_z{}^2_{\text{mother}}}, \tag{3.24}$$

Its associated uncertainty is defined as

$$\sigma_M^{\text{mother}} = \sqrt{\frac{1}{4M^2_{\text{mother}}} v^T H v}, \tag{3.25}$$

with

$$v := \frac{dM^2_{\text{mother}}}{d\vec{q}} = \begin{pmatrix} -2p_{x_{\text{mother}}} \\ -2p_{y_{\text{mother}}} \\ -2p_{z_{\text{mother}}} \\ 2E_{\text{mother}} \end{pmatrix} \tag{3.26}$$

and

$$H := \sum_{k \in \text{daughters}} V_{q_k}. \tag{3.27}$$

3.1.2 Decay Tree Fitter algorithm

While the leaf-by-leaf approach adopted by the Vertex Fitter is fast, it brings alongside it the significant drawback of forgoing upstream information when fitting the downstream branches of a decay. This is especially notable for decays like $K_S^0 \to \pi^0\pi^0 \to \gamma\gamma\gamma\gamma$, where the final state has no tracks to form a vertex with. Even in the relatively more traditional case of the $\Lambda_b^0 \to J/\psi\,\Lambda^0$ decay, however, the VF algorithm still limits our options. In particular, it prevents the placing of *mass constraints* on mother particles, where the fit fixes the invariant mass of daughter pair to the PDG value for mother particle mass.

To compensate for this, all reconstructed events in this analysis undergo a refit process based on the Decay Tree Fitter (DTF) algorithm [78] first developed in BaBar. This algorithm fits the entire decay chain simultaneously, fixing the decay vertices to the values found by the Vertex Fitter, and allows to place mass constraints on $p\pi^-$ and $\mu^+\mu^-$ invariant masses to match $m(\Lambda^0)$ and $m(J/\psi)$ respectively.

This process unfortunately introduces another filtering step to account for, further reducing the prospective signal yield. DTF convergence efficiency with the double mass constraint is relatively uneven across the z_Λ^{vtx} spectrum, starting at $\approx 50\%$ for $z_\Lambda^{\text{vtx}} \approx 6\,\text{m}$ and growing up to $\approx 85\%$ for $z_\Lambda^{\text{vtx}} \approx 7.5\,\text{m}$ (see Figure 4.15). Despite the significant event loss, DTF proves invaluable for our physics motivations as it mitigates the most problematic drawback of T track usage, momentum resolution: using both J/ψ and Λ^0 mass constraints improves $\vec{p}$ resolution from 20–30% to $\approx 10\%$ for protons and pions alike.

3.2 Reconstruction efficiency of the Λ_b^0 and Λ^0 decays

To compute the vertex reconstruction efficiency for the Λ_b^0 decay chain, it is useful to conceptualize our event selection as a five step process:

1. reconstruction of associated tracks for all charged daughter particles;
2. reconstruction of Λ^0 and Λ_b^0 decay vertices[26];
3. preliminary selections based on kinematic variables to filter out most background (see Section 4.1);

[26] J/ψ vertex reconstruction is is a prerequisite for event selection in the detached $J/\psi \to \mu^+\mu^-$ trigger line (see Section 2.5) and does not factor in the vertexing efficiency.

4. Decay Tree Fitter refit with appropriate mass constraints for the analysis at hand (usually J/ψ and Λ^0);

5. further selections applied to events passing all previous steps. Detailed in Chapter 4, these include physical background vetoes and signal selection via a trained multivariate classifier.

For the purposes of this section, we are interested in the first two steps (track and vertex reconstruction).

Efficiencies are computed with respect to *reconstructible* particles, a flag attributed during the simulation process based on the number of hits (charged clusters with defined positions) in specific modules of the LHCb detector. A track is said to be reconstructible as VELO track with hits in ≥ 3 VELO modules, while it's reconstructible as T track with ≥ 1 hits in both the x and stereo layers of each T station. If these conditions are satisfied simultaneously, the track qualifies for reconstructibility as Long track [79].

At Monte Carlo level, a track is deemed to be *reconstructed* if it can be successfully matched to at least one MC particle; for T and Long tracks, this is true if at least 70% of the hits from the respective relevant detectors for reconstructibility are shared between reconstructed and true track. For $\Lambda_b^0 \to J/\psi\,\Lambda^0$ events with a true $z_{\text{vtx}}^{\Lambda} \in [6.0\,\text{m}, 7.6\,\text{m}]$, this results in a track reconstruction efficiency

$$\varepsilon_{\text{reconstruction}} := \frac{n_{\text{reconstructed}}}{n_{\text{reconstructible}}} \tag{3.28}$$

in the 60% to 80% range.

When considering how many of these reconstructed charged particles pass the vertex reconstruction (*vertexing*) process, efficiency

$$\varepsilon_{\text{vertexing}} := \frac{n_{\text{vertexed}}}{n_{\text{reconstructed}}} \tag{3.29}$$

is much lower. Figure 3.1 plots Λ_b^0 and Λ^0 vertexing efficiency through the whole true z_{vtx}^{Λ} spectrum, showing it never manages to get past the 50% threshold. This means that over half of candidate signal events are lost during the second step of the five-step selection process.

Available information does not distinguish between $\Lambda_b^0 \to J/\psi\,\Lambda^0$ and $\Lambda^0 \to p\pi^-$ vertexing efficiencies. Nevertheless, the rare usage of T tracks for physics analysis in LHCb suggests that problems are likelier to arise in the $\Lambda^0 \to p\pi^-$ vertexing and then cascade into $\Lambda_b^0 \to J/\psi\,\Lambda^0$ reconstruction. In the following sections I'll thus focus on the $\Lambda^0 \to p\pi^-$ decay with the goal of understanding the problem and improving signal yield.

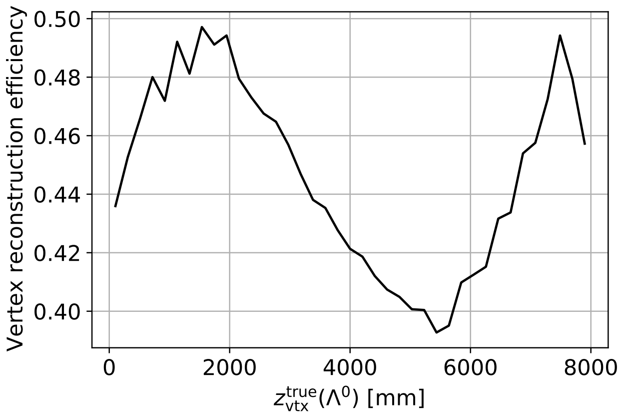

Figure 3.1: Reconstruction efficiency of simulated $\Lambda_b^0 \to J/\psi\ (\to \mu^+\mu^-)\ \Lambda^0\ (\to p\pi^-)$ events as function of the z component of the true Λ^0 decay vertex. Given that $J/\psi \to \mu^+\mu^-$ events are reconstructed as part of the trigger step, the low efficiency is attributed to failure in reconstructing Λ^0 and Λ_b^0 decay vertices.

3.3 Characterization of non-converged events

In order to narrow down the possible origin of the vertexing deficiency in $\Lambda^0 \to p\pi^-$ events, I conducted a series of comparative studies to characterize non-converged events and their differences to reconstructed ones. The full simulated $\Lambda_b^0 \to J/\psi\,\Lambda^0$ dataset constructed for the measurement of the Λ^0 electromagnetic dipole moments omits a lot of technical information on the decays, the retention of which would make storage and quick access impractical. Furthermore, a lot of the work in this and the next sections required direct changes to the vertexing algorithm for debugging and event recovery, which in turn required data to be reprocessed. For these reasons, the studies in the following sections were conducted on a smaller sample of $\approx 110\,000$ Λ_b^0 decays (about 4600 of which are reconstructed) in sign $B_y = +1$ configuration, where $\vec{B}$ is the LHCb magnetic field.

3.3.1 Decay kinematics before and after interaction with the detector

No difference between converged and failed $\Lambda_b^0 \to J/\psi\,\Lambda^0$ events emerges at Monte Carlo level when considering the true values of basic kinematic variables such as daughter particle momenta and decay vertices locations of the three unstable particles Λ_b^0, Λ^0 and J/ψ. Moreover, there doesn't seem to be a critical decay geometry associated to the drop in vertexing efficiency; for instance, there is no evidence that $\Lambda^0 \to p\pi^-$ decays lying largely in the xz

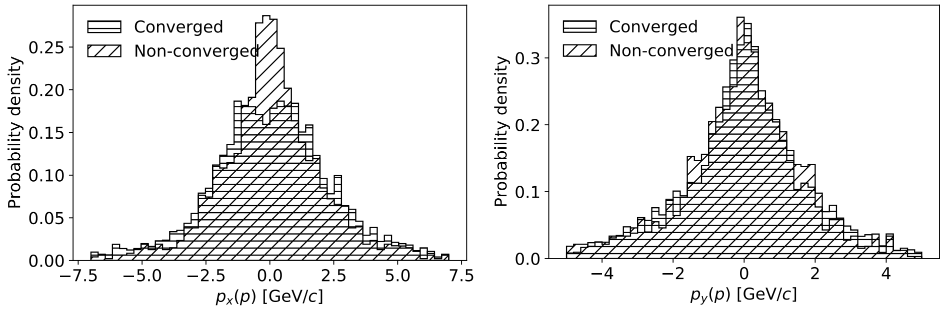

(a) **(b)**

Figure 3.2: Normalized distributions of proton protoparticles p_x *(a)* and p_y *(b)* components in simulated $\Lambda^0 \to p\pi^-$ events. Distributions of events with converging vertex fit are depicted with *horizontal hatching*, non-converging fit with *diagonal hatching*.

plane, a setup quite unfriendly to the VF algorithm (see Section 3.5), have any disproportionate representation amongst non-converged events. This rules out the hypothesis that the failure of vertex fit convergence be caused by particle characteristics at production, such as protons and pions with unusually low transverse momentum p_{T}.

I also considered the possibility that kinematic asymmetries between converged and failed events may arise after interaction with the LHCb detector; one example of this would be the case where failed events correlate with hits in a specific sections of the IT or OT trackers. To this end I studied the event *protoparticles*, data structures created during the LHCb event reconstruction process to encapsulate relevant information for the associated particle: particle identification from the RICH and muon detectors, results from calorimeter hits and track information.

Protoparticles associated to charged tracks store momentum and energy evaluated in a certain reference point which, for stable particles, corresponds to the position of first measurement of the track. Figure 3.2a depicts the only major discrepancy between converged and failed events I found in the protoparticle analysis: non-converged Λ_b^0 decays have a proton protoparticle p_x distribution concentrated in $p_x \approx 0$, while converged decays show even dispersion of the central peak in the $[-1\,\mathrm{GeV}, 1\,\mathrm{GeV}]$ region. This contrasts with p_y, the other component of the protoparticle transverse momentum, whose two distributions are almost overlapping (Figure 3.2b). Pions do not appear to show similar discrepancies in their protoparticles. Given the significant overlap between the distributions in Figure 3.2a, however, the overabundance of low p_x of proton protoparticles in non-converged events does not appear to be a deciding factor for the Vertex Fitter failure.

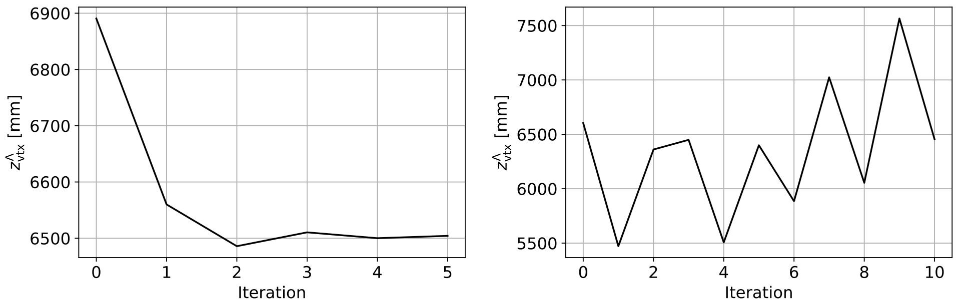

(a) **(b)**

Figure 3.3: Best values of tentative $\Lambda^0 \to p\pi^-$ vertex z component at the end of each Vertex Fitter iteration for examples of converged *(a)* and failed *(b)* events.

3.3.2 Behaviour through VF iterations

The VF process reaches convergence if either condition (3.14) or (3.15) is satisfied, i.e. if the vertex position estimated at iteration i and the one from iteration $i-1$ are «close enough» either in absolute distance or χ^2 distance, up until $i_{\max} = 10$. This is predicated on the principle that the algorithm refines its vertex estimate after each iteration, homing in on the candidate vertex with the lowest $\tilde{\chi}^2_{\text{vtx}}$[27].

Such a behaviour is not found in non-converging (henceforth also known as *failed*) events. This can be seen by increasing $i_{\max} = 100$, which causes a negligible $\approx 2\%$ increase in converged events. It follows that, for the vast majority of missing events, failure of convergence is not a product of low computation time and must instead result from some internal malfunction of the vertexing process.

This becomes apparent when studying the vertex positions throughout the iterating process for instances of converged and failed events of simulated signal. Figure 3.3 compares the values of z^{Λ}_{vtx}, the z component of the $\Lambda^0 \to p\pi^-$ decay vertex, as reconstructed by the VF in iterations $i = 0$ to 10 ($i = 0$ being the starting seed). Figure 3.3a (converged) exhibits the expected behaviour, with the algorithm refining its vertex estimate after every iteration and finally converging as early as $i = 5$. By contrast, Figure 3.3b (failed) presents an oscillating behaviour of z^{Λ}_{vtx}, swinging by as much as 1 m in the opposite direction after an iteration completes. While a particularly tricky instance of the first type of event may potentially benefit by an increased $i_{\max}$, no amount of allotted computations can lead the second type to convergence.

We can gain more insight into the nature of this oscillation by approaching the problem from a more topological point of view. Figure 3.4 shows the

[27] $\tilde{\chi}^2_{\text{vtx}}$ is the reduced χ^2_{vtx}, i.e. χ^2_{vtx} divided by the number n_d of degrees of freedom.

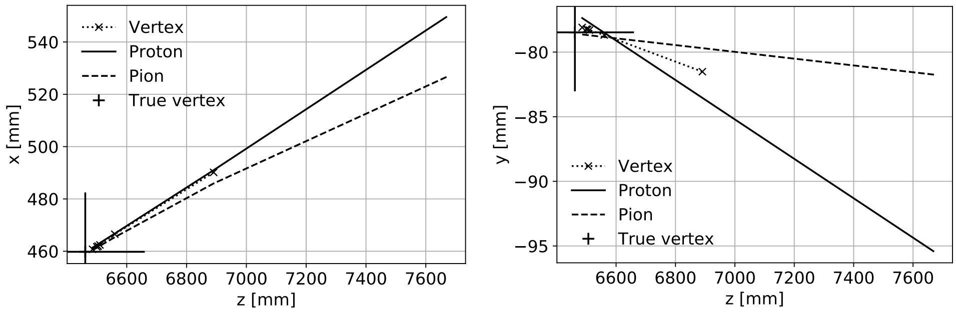

(a) **(b)**

Figure 3.4: $\Lambda^0 \to p\pi^-$ decay topology for an instance of converged event, projected in the *xz (a)* and *yz (b)* planes. The temporary best vertex locations chosen by the Vertex Fitter at the end of each iterations are marked with *diagonal crosses* and linked by the *dotted line* in iteration order (the second iteration best vertex is connected to the first, the third to the second and so on). The reconstructed vertex, while not explicitly represented, can be identified by the cluster of vertex point markers. At the beginning of each iteration, daughter particles are extrapolated at the z of the best vertex of the previous iteration: proton (*solid line*) and pion (*dashed line*) tracks are drawn joining the respective reference points after transportation in order of decreasing z (i.e. not in iteration order). The true vertex is marked by the *large Greek cross.*

topology of the converged event from Figure 3.3a in the bending xz and non-bending yz planes. While the points of closest distance between the tracks in the two planes are not exactly matched, the algorithm manages to converge on a vertex position that is reasonably close to the true generated decay vertex.

The behaviour for the non-converged event from Figure 3.3b, shown in Figure 3.5, is drastically different. The dotted line following the best vertex estimate through iterations in the bending plane (Figure 3.5a) shows that the algorithm gravitates *around* the point of closest distance between proton and pion tracks ($z \approx 6.25\,\mathrm{m}$), never outright choosing it as candidate. On the other hand, in the yz plane (Figure 3.5b) the two tracks cross at a much more downstream point ($z \approx 7.5\,\mathrm{m}$), which the Vertex Fitter also largely ignores during the iteration process.

Failed convergence in this event cannot be attributed to the comparatively larger gap between proton and pion tracks at their point of closest distance in the bending plane. The VF algorithm has shown to be capable of bridging an imperfect track extrapolation: the converged event shown in Figure 3.6 has a closest track distance of some 40 cm, an order of magnitude greater than the track distance seen in Figure 3.5. Despite the large gap, the VF is able to recognize $z \approx 3\,\mathrm{m}$ as the best candidate for the vertex. This hap-

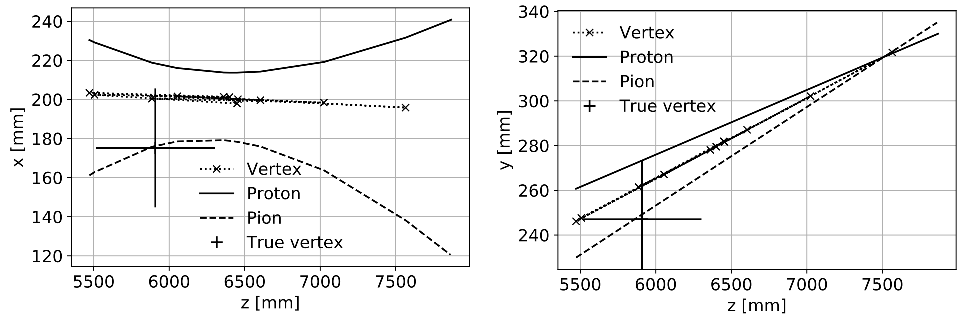

(a) (b)

Figure 3.5: $\Lambda^0 \to p\pi^-$ decay topology for an instance of non-converged event, projected in the xz *(a)* and yz *(b)* planes. Notation follows the one in Figure 3.4.

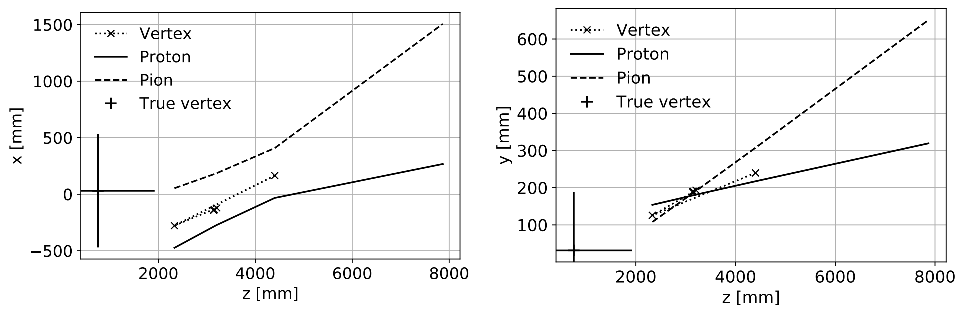

(a) (b)

Figure 3.6: $\Lambda^0 \to p\pi^-$ decay topology for an instance of converged event with large track gap in the xz plane, projected in the xz *(a)* and yz *(b)* planes. Notation follows the one in Figure 3.4.

pens despite the large distance between this point and the true $\Lambda^0 \to p\pi^-$ vertex: the discrepancy is due to poor initial momentum measurement for the tracks and demonstrates the flexibility of the VF algorithm, converging even in circumstances that are far from ideal.

The more convincing explanation for the vertex oscillation is therefore that the candidate vertices in the xz and yz planes are too far apart for the VF to reconcile the two; the algorithm is not equipped to favour one over the other, leading to meter-wide swings when it strays too far off from either of them. Convergence failure in Figure 3.5 can thus be interpreted through the lens of *conflicting information.*

In this section I have focused the analysis on one particular event for didactic purposes. All the outlined patterns are nonetheless commonplace throughout failed events I have examined, with the oscillating vertex behaviour in particular being a constant in all of them. While it would be reckless to conclude that every $\Lambda^0 \to p\pi^-$ vertexing failure must be the fault of xz and yz track mismatch, I have been able to use these findings, along with other from the following paragraphs, to devise a partial solution in Section 3.4.

3.3.3 Decay kinematics after extrapolation

As will be later discussed in Sections 3.4 and 3.5, reconstruction of the Λ^0 vertex is affected by a significant positive bias of median value[28] $\mu_{\frac{1}{2}}\,(z_\Lambda^{\text{reco}} - z_\Lambda^{\text{true}}) \approx 40\,\text{cm}$. In spite of such a discrepancy, the standard modus operandi for kinematics-at-vertex analyses usually compares true momenta (evaluated at the true vertex) with reconstructed momenta (evaluated at the reconstructed vertex), ignoring the discrepancy.

For this section I have followed a different approach, opting to transport via Runge-Kutta extrapolator the reconstructed p and π^- at the true $\Lambda^0 \to p\pi^-$ vertex position, injected from Monte Carlo information. Tracks are transported to a given z within extrapolator tolerance, leaving x and y coordinates (*reference points*, henceforth) dependent on the initial measured momentum.

Since the extrapolator takes raw protoparticles as inputs, this process bypasses any smoothing applied during the fit process and, given an observable f (particle reference points and momenta, for instance), it allows for a comparison between the true value f_{true} and the RK-extrapolated value f_{RK} at the actual z_{vtx}^{Λ}, circumventing the effect of vertex bias. Any potential mismatch will be normalized in terms of *pulls*

$$\frac{f_{\text{RK}} - f_{\text{true}}}{\sigma_f^{\text{RK}}}, \tag{3.30}$$

with σ_f^{RK} being the uncertainty computed by the RK extrapolator. Assuming correct estimation of such uncertainties, we expect the pulls to follow a standard normal distribution.

Figure 3.7 shows p_z pulls for proton and pions extrapolated at the Λ^0 true decay vertex, juxtaposing converged and non-converged event distributions. The first takeaway is that VF-reconstructed events have remarkably non-Gaussian distributions, with slightly positive means and asymmetric tails. Moreover, Figure 3.7b highlights the fact that pion tracks from non-converged events generally sport a strong negative bias on p_z.

Transverse momenta of proton and pions after transport show no similar biases when both $\Lambda^0 \to p\pi^-$ and $\bar{\Lambda}^0 \to \bar{p}\pi^+$ events are considered. A significant

[28] Throughout the thesis, the *median value* of a distribution is defined as the value separating the lower and upper halves of the distribution, i.e. the $\mu_{\frac{1}{2}}$ operator. Since even a small number of outliers can skew the arithmetic mean, this gives a better representation of the average value for many variables used in this analysis.

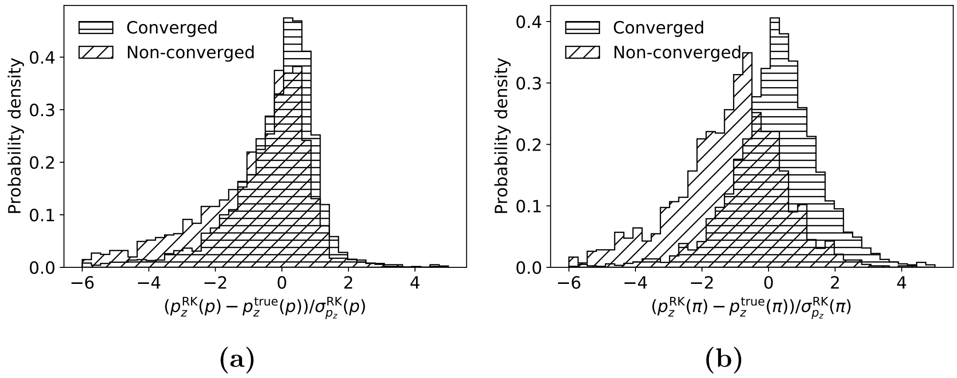

Figure 3.7: Normalized distributions of proton *(a)* and pion *(b)* p_z pulls after track extrapolation at the true simulated $\Lambda^0 \to p\pi^-$ vertex. Distributions of events with converging vertex fit are depicted with *horizontal hatching*, non-converging fit with *diagonal hatching.*

bias in the extrapolated p_x of both particles instead becomes visible when including only the former or latter class of events. The situation for Λ^0 decays is shown in Figure 3.8a: converged events bear a $\leq 1\sigma$ positive p_x bias for pions, while failed events are negatively biased with a much larger dispersion; the signs of both biases are reversed in $\bar{\Lambda}^0 \to \bar{p}\pi^+$ decays, as seen in Figure 3.8b.

This behaviour of the p_x pulls also reflects on the x components of the particle reference points after extrapolation, whose pulls are depicted in Figure 3.9. For each class, x_{ref} bias is opposite to the corresponding p_x bias (e.g. $x_{\mathrm{ref}}^{\mathrm{RK}} > x_{\mathrm{ref}}^{\mathrm{true}}$ and $p_x^{\mathrm{RK}} < p_x^{\mathrm{true}}$ for pions in non-converging $\Lambda^0 \to p\pi^-$ events) and its sign flips when switching from matter to antimatter.

Bearing in mind that data for this analysis are simulated in magnet-up detector configuration, the discrepancies in x_{ref} and p_x pulls after extrapolation can be read as consequence of the p_z systematic underestimation in non-converged decays seen in Figure 3.7. A particle's p_z is intertwined with the bending curve imprinted by the magnetic field, as particles with higher p_z will proportionally bend less (this is usually the case for protons, which carry most of the Λ^0 momentum in its $p\pi^-$ decay). The underestimation of p_z thus results in overstated bending, and vice versa an overestimation of the bending curve during extrapolation will cause a lower p_z at the true vertex; this impacts in turn the x component of the particle's reference point, introducing a bending-dependent offset with respect to the true vertex position. This interpretation, illustrated in Figure 3.10 with a simplified diagram, links all three observed biases (p_z, p_x and x_{ref}), explains the mirrored behaviour of Λ^0 and $\bar{\Lambda}^0$ decays (bending direction is inverted due to opposite charge) and justifies the

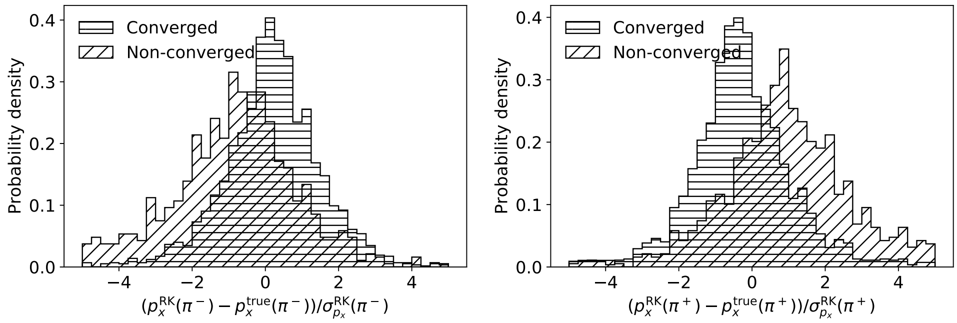

(a) **(b)**

Figure 3.8: Normalized distributions of pion p_x pulls in simulated $\Lambda^0 \to p\pi^-$ *(a)* and $\bar{\Lambda}^0 \to \bar{p}\pi^+$ *(b)* events after track extrapolation at the true $\Lambda^0/\bar{\Lambda}^0$ decay vertex. Distributions of events with converging vertex fit are depicted with *horizontal hatching*, non-converging fit with *diagonal hatching*.

stronger impact on pions as opposed to protons, whose tracks are much more akin to straight lines due to higher average momentum.

Finally, the underestimation of pion p_z is relevant to the problem of low vertex reconstruction efficiency. The xz and yz propagation planes are affected differently by p_z underestimation on account of the magnet bending in the former. This can potentially result in the conflict between xz and yz topologies observed in non-converged events, the current leading hypothesis to explain the oscillatory behaviour of the VF algorithm which prevents decay convergence. Considering the information gathered so far, the most plausible cause of this p_z bias appears to be poor momentum measurement at T station level.

3.4 Recovery of non-converged events through refit with rescaled uncertainties

As outlined in Section 3.3.2, vertexing failures in the $\Lambda^0 \to p\pi^-$ decay can be attributed to candidate vertices in different planes providing conflicting information. To circumvent this phenomenon, my proposal for the recovery of these failed events involves performing an additional fit of the vertex (also referred to as *refit* in the following pages) with a slightly altered version of the standard Vertex Fitter algorithm designed to attribute greater importance to a specific propagation plane.

The reasonable choice for this plane would be the yz plane, since extrapolation of tracks does not need to be concerned with magnet bending and is therefore expected to be less prone to error. However, this would penalize

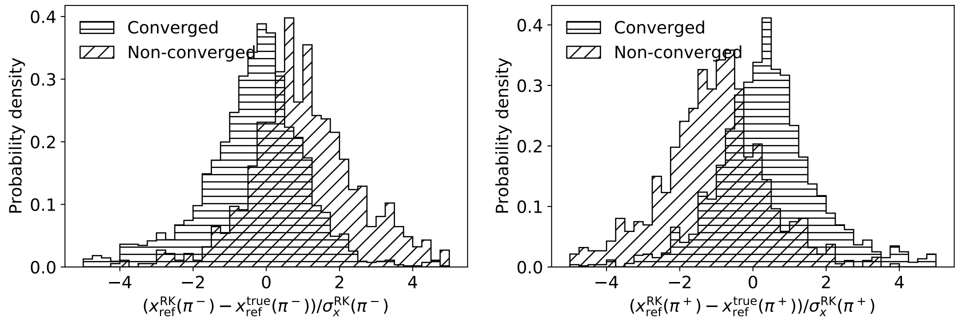

Figure 3.9: Normalized distributions of the x component pulls of the pion reference point in simulated $\Lambda^0 \to p\pi^-$ *(a)* and $\bar{\Lambda}^0 \to \bar{p}\pi^+$ *(b)* events after track extrapolation at the true $\Lambda^0/\bar{\Lambda}^0$ decay vertex. Distributions of events with converging vertex fit are depicted with *horizontal hatching*, non-converging fit with *diagonal hatching*.

events with poor yz protoparticle reconstruction, for instance events with parallel or diverging tracks in said plane. To maximize the recovery efficiency of my solution, I have elected to perform three separate refits on non-converging events, prioritizing $yz \to xz \to xy$ planes in this order. In a worst-case scenario, this would quadruple the time complexity of the vertexing process; in practice, half of all events converge with the standard VF, and about $\approx 15\%$ more converge after the first refit attempt (yz plane).

Considering the yz plane as an example, we can prioritize available track information in this plane by artificially increasing the uncertainty σ_x of the x component of the candidate vertex position $\vec{x}$. At each step in a VF iteration, $\vec{x}$ is updated according to (3.9). Uncertainties enter the computation through three terms:

1. $(C_{k-1}^i)^{-1}$, the inverse vertex covariance matrix computed at the previous step (or final step of the previous iteration);

2. $(G_k^i)_r$, the inverse covariance matrix of reference point $\vec{r}_k^i$, computed at the true transport of particle k;

3. C_k^i, the current vertex covariance matrix, inverted from the matrix sum of the previous two terms as in (3.8).

Ergo, the best approach to increase σ_x while minimizing additional computation time is to act on the individual components of $(C_{k-1}^i)^{-1}$ and $(G_k^i)_r$ just before the (3.8) sum.

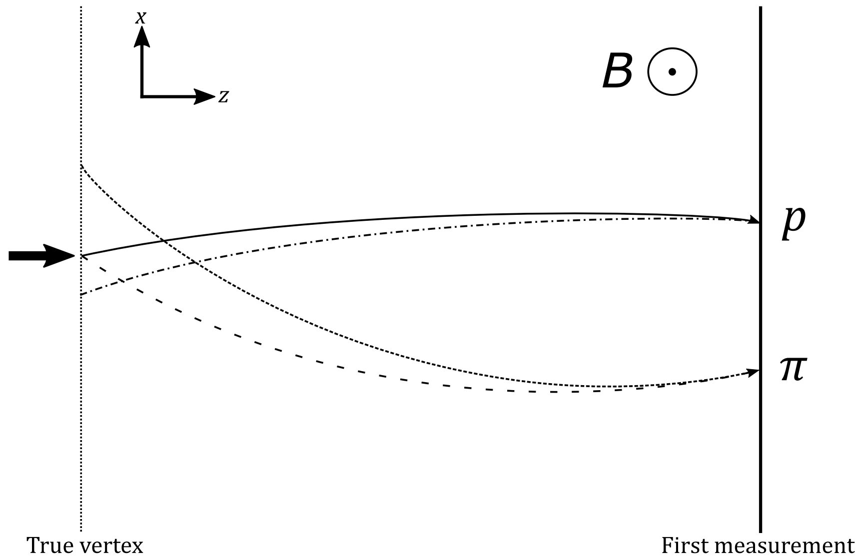

Figure 3.10: Simplified $\Lambda^0 \to p\pi^-$ diagram demonstrating the relation between p_z underestimation and bias on π^- x components of reference point and momentum after track extrapolation at the true vertex, denoted by the *thick arrow on the left* and whose z coordinate is traced with the *vertical dotted line.* The true (extrapolated) proton track is drawn as a *solid* (*dash-dotted*) arrow, the pion as a *dashed* (*short-dashed*) arrow. The first measurement position, doubling as starting point for the backwards extrapolation, is marked by the *thick vertical line on the right.* The decay is shown in the xz bending plane assuming the LHCb magnet in up polarity.

Assuming Gaussian uncertainties, a standard three-dimensional covariance matrix will have the form

$$C = \begin{pmatrix} \sigma_x^2 & \rho_{xy}\sigma_x\sigma_y & \rho_{xz}\sigma_x\sigma_z \\ \rho_{xy}\sigma_x\sigma_y & \sigma_y^2 & \rho_{yz}\sigma_y\sigma_z \\ \rho_{xz}\sigma_x\sigma_z & \rho_{yz}\sigma_y\sigma_z & \sigma_z^2 \end{pmatrix}, \tag{3.31}$$

where $\rho_{ij} \coloneqq \mathrm{corr}(i, j)$. Its inverse matrix is written as

$$C^{-1} = \frac{1}{K} \begin{pmatrix} \frac{1-\rho_{yz}^2}{\sigma_x^2} & \frac{\rho_{xz}\rho_{yz}-\rho_{xy}}{\sigma_x\sigma_y} & \frac{\rho_{xy}\rho_{yz}-\rho_{xz}}{\sigma_x\sigma_z} \\ \frac{\rho_{xz}\rho_{yz}-\rho_{xy}}{\sigma_x\sigma_y} & \frac{1-\rho_{xz}^2}{\sigma_y^2} & \frac{\rho_{xy}\rho_{xz}-\rho_{yz}}{\sigma_y\sigma_z} \\ \frac{\rho_{xy}\rho_{yz}-\rho_{xz}}{\sigma_x\sigma_z} & \frac{\rho_{xy}\rho_{xz}-\rho_{yz}}{\sigma_y\sigma_z} & \frac{1-\rho_{xy}^2}{\sigma_z^2} \end{pmatrix}, \tag{3.32}$$

with

$$K \coloneqq \frac{\det C}{\sigma_x^2\sigma_y^2\sigma_z^2} = 1 + 2\rho_{xy}\rho_{xz}\rho_{yz} - \rho_{xy}^2 - \rho_{xz}^2 - \rho_{yz}^2. \tag{3.33}$$

Algorithm	Median $\tilde{\chi}^2_{\text{vtx}}(\Lambda^0)$					
	Common events	Exclusive events	Pair-shared events			
			VF	σ_x	σ_y	σ_z
VF	1.35	0.32	–	1.06	1.28	1.36
σ_x	1.36	3.18	1.09	–	1.61	1.84
σ_y	1.38	3.13	1.32	1.63	–	1.96
σ_z	1.41	51.52	1.45	1.88	2.01	–

Table 3.1: Comparison of median $\tilde{\chi}^2_{\text{vtx}}$ of the $\Lambda^0 \to p\pi^-$ vertex fit performed by the Vertex Fitter and the three σ-rescaled algorithms. Performances are reported on common events reconstructed by all four algorithms, on exclusive events reconstructed only by a specific algorithm, and on events reconstructed pairwise by at least two algorithms.

Going back to the yz plane example, we increase σ_x by introducing a multiplicative factor $s_x < 1$ for relevant covariance matrix components as follows:

$$\begin{aligned} C^{-1}_{xx} &= C^{-1}_{xx} \times s_x^2, \\ C^{-1}_{xy} &= C^{-1}_{yx} = C^{-1}_{xy} \times s_x, \\ C^{-1}_{xz} &= C^{-1}_{zx} = C^{-1}_{xz} \times s_x, \end{aligned} \tag{3.34}$$

with other components left as is. This process is also applied to $(G^i_k)_r$ and replicated at each step of the refit algorithm, which I'll refer to as *σ_x-rescaled.* Similarly, the σ_y-rescaled and σ_z-rescaled algorithms prioritize planes xz and xy respectively (their extension from (3.34) is trivial). For the remainder of this section, I'll refer to their sequential application $\sigma_x \to \sigma_y \to \sigma_z$ as the *σ-rescaled refit process.*

As proof of concept, I have analyzed the performance of the σ-rescaled refit approach on the sample of 110 000 MC-generated $\Lambda_b^0 \to J/\psi\,\Lambda^0$ events previously used in this chapter. Choosing $s_i = 0.98, i \in \{x, y, z\}$, which maximizes the number of events recovered by the refit and corresponds to a $\approx 2\%$ increase in vertex uncertainties, I observed a +26.4% increase in reconstructed signal. Given a vertexing efficiency $\lesssim 50\%$, as reported in Figure 3.1, this amounts to roughly a quarter of all missing reconstructible decays. Within these recovered events, 57.1% converge under the σ_x algorithm, 38.1% under the σ_y algorithm and the remaining 4.8% under the σ_z algorithm.

I have also run each individual σ-rescaled algorithm in isolation (without the Vertex Fitter) on the simulated signal to evaluate their performances on

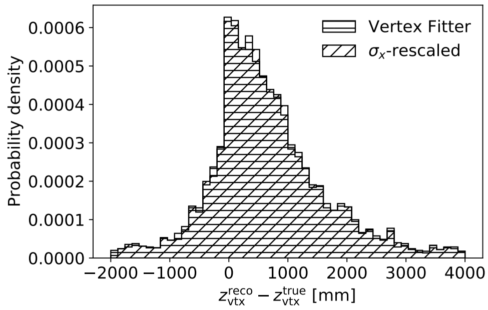

(a)

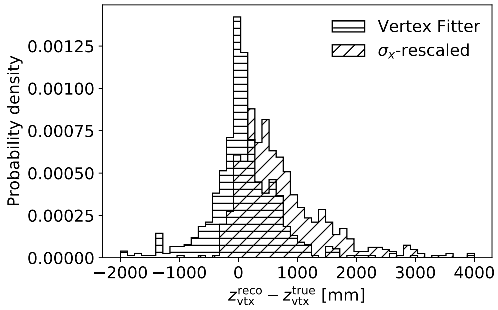

(b)

Figure 3.11: Normalized distributions of bias on the $\Lambda^0 \to p\pi^-$ vertex z component reconstructed by the standard Vertex Fitter (*horizontal hatching*) and σ_x-rescaled (*diagonal hatching*) algorithms. The algorithms were individually run on the same simulated $\Lambda_b^0 \to J/\psi\,\Lambda^0$ sample: *(a)* shows distributions for events reconstructed by both algorithms, *(b)* shows distributions for events only reconstructed by one or the other.

all events, including standard-converging ones. Before proceeding, a digression is in order to better understand the meaning of *performance* when comparing the algorithms. Table 3.1 shows the median $\chi^2_{\rm vtx}$ of the reconstructed vertices on specific subsamples of events:

- *common* events converging under Vertex Fitter and all three σ-rescaled algorithms;
- *pairwise shared* events converging under (at least) two algorithms (e.g. VF and σ_x-rescaled, including events that may also converge under σ_y-rescaled);
- *exclusive* events only reconstructed by one particular algorithm.

For common events, algorithm performances show very little variation, with a marginal performance hierarchy of VF $> \sigma_x > \sigma_y > \sigma_z$. The aforementioned hierarchy also holds in pairwise shared events: for instance, VF-σ_x events have VF vertices with median $\tilde{\chi}^2_{\rm vtx}$ of 1.06, slightly lower than the 1.09 of σ_x vertices.

Where algorithm performances truly diverge is in exclusive events. Events only converging under VF have a median $\tilde{\chi}^2_{\rm vtx}$ of 0.32, while both σ_x and σ_y hover around a subpar ≈ 3 and the σ_z algorithm reaches an off-scale value of 51. This discrepancy is also seen from a different perspective in Figure 3.11: the $z^{\Lambda}_{\rm vtx}$ residual distributions for VF and σ_x-rescaled algorithms on shared events are indistinguishable (Figure 3.11a), while σ_x-exclusive events have a significant positive bias compared to the unbiased VF-exclusive ones (Figure

Algorithm	Statistics increase	Median $\tilde{\chi}^2_{\text{vtx}}(\Lambda^0)$	Median bias	
			z^{Λ}_{vtx} [mm]	$p_z^{\text{DTF}}(p)$
VF	–	1.0	399	+0.02%
σ_x	+15.0%	6.1	541	−0.48%
σ_y	+18.9%	5.8	573	−1.12%
σ_z	+20.7%	9.2	729	−0.71%
Sequential	+26.4%	7.1	604	−0.81%

Table 3.2: Performance comparison of the three σ-rescaled algorithms with $s_i = 0.98$, their sequential application ($\sigma_x \to \sigma_y \to \sigma_z$) and the standard Vertex Fitter algorithm. Median values for shown variables are computed on recovered events for σ-rescaled algorithm, standard reconstructed events for the Vertex Fitter. Proton p_z is computed using the Decay Tree Fitter algortihm with J/ψ and Λ^0 mass constraints.

3.11b). This means that, while a minor hierarchy in fit quality does exist in the σ-rescaled algorithms, justifying the selected $\sigma_x \to \sigma_y \to \sigma_z$ refit order, large discrepancies in performances are due to differences in the converging events themselves. The most likely explanation for the diminishing fit quality in σ-rescaled algorithms is poor track information in the relevant propagation planes: for instance, an event only converging with the σ_z-rescaled algorithm must have subpar information in the xz and yz planes (preventing convergence with VF, σ_x- and σ_y-rescaled algorithms), and favouring information in the xy plane when deciding the best vertex will lead to poor resolution in z^{Λ}_{vtx}. This interpretation also explains the large fit quality gap between exclusive σ_x- and σ_y-converging events ($\tilde{\chi}^2_{\text{vtx}}(\Lambda^0) \approx 3$) and exclusive σ_z-converging events ($\tilde{\chi}^2_{\text{vtx}}(\Lambda^0) \approx 51$), as the latter algorithm forgoes most information for the crucial z axis.

With this in mind, Table 3.2 reports the performance of the three σ-rescaled algorithms and the full σ-rescaled refit process on recovered events, compared to the VF performance on standard reconstructed events. The overall $\tilde{\chi}^2_{\text{vtx}}$ of the $\Lambda^0 \to p\pi^-$ vertex for recovered events is significantly worse than the expected 1.0 value obtained by the VF; likewise, the median $\approx 40\,\text{cm}$ z^{Λ}_{vtx} bias in VF events (discussed more in detail in Section 3.5) is still 20 cm lower than in recovered events (also shown in terms of pulls in Figure 3.12). As discussed in Section 3.3.3, non-converging events show a systematic p_z underestimation in pion T tracks, which also reflects on recovered events in the negative p_z

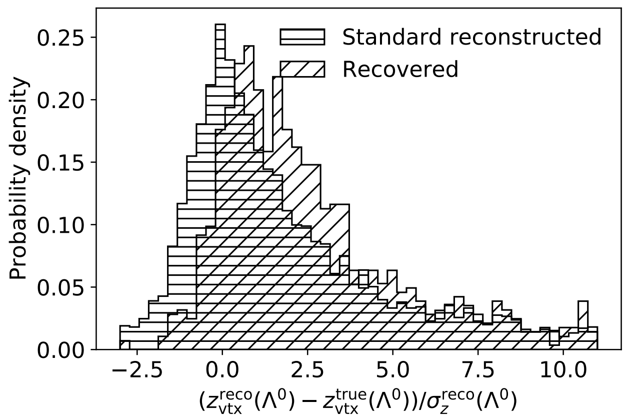

Figure 3.12: Normalized distribution of $z_{\mathrm{vtx}}^{\Lambda}$ pulls in simulated $\Lambda_b^0 \to J/\psi\,\Lambda^0$ events: decays reconstructed with the Vertex Fitter are labeled with *horizontal hatching*, decays recovered via the sequential application of σ-rescaled algorithms with *diagonal hatching*.

bias computed with the Decay Tree Fitter algorithm using J/ψ and Λ^0 mass constraints (Table 3.2). This phenomenon explains the increased $z_{\mathrm{vtx}}^{\Lambda}$ bias, as a lower p_z at T station position translates in an apparent crossing point downstream of the actual vertex (this is exemplified in Figure 3.10).

Tables 3.1 and 3.2 confirm that the σ_z-rescaled algorithm is by far the worse performing of the three. This is a somewhat expected consequence of partially forgoing xz and yz information in the fit, and placing this algorithm last in the process ensures that it only affects events which would not converge under other circumstances. In the context of the proof-of-concept study, I elected to include the σ_z-rescaled algorithm in the refit process to gain a more complete view of its capabilities. However, were the ensuing events to be considered too poorly reconstructed for the Λ^0 analysis, the algorithm could feasibly be omitted as it only contributes a negligible +1.3% of additional signal.

In conclusion, my σ-rescaled refit process allows for a +26.4% increase in reconstructed signal events. While $\tilde{\chi}^2_{\mathrm{vtx}}$ and bias on $z_{\mathrm{vtx}}^{\Lambda}$ are higher compared to events reconstructed via Vertex Fitter, there is sufficient evidence pointing towards this being a problem intrinsic to the non-converged events themselves. Because of the timing requirements to perform a re-reconstruction of the full data sample (described in Section 2.5), I didn't employ recovered events for the remainder of the analysis. The impact of their increased bias on the prospective Λ^0 EDM/MDM measurement will have to be evaluated in dedicated sensitivity studies and possibly incorporated as a source of systematic uncertainty to be accounted for.

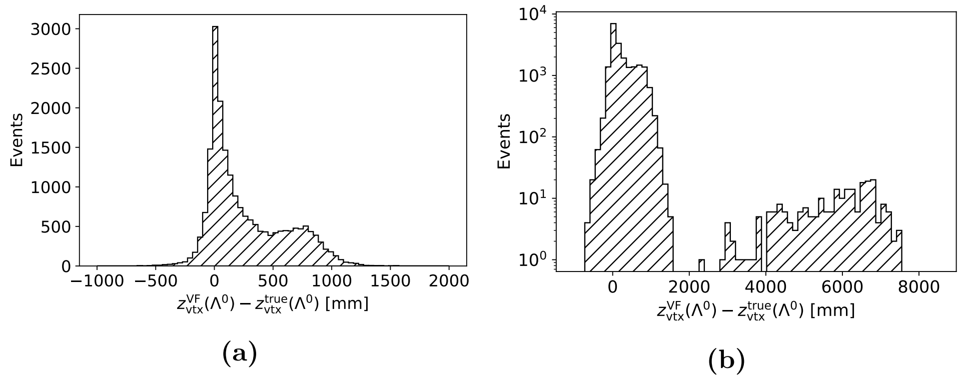

Figure 3.13: Distribution of $z_{\mathrm{vtx}}^{\Lambda}$ bias in linear *(a)* and logarithmic *(b)* scales for simulated $\Lambda_b^0 \to J/\psi\,\Lambda^0$ events after all selection steps.

3.5 Λ^0 decay vertex bias in standard reconstructed events

So far I have focused on the additional bias on $z_{\mathrm{vtx}}^{\Lambda}$ introduced by the newly recovered events. As previously remarked, however, standard reconstructed events are significantly biased as well. The quality of the $\Lambda^0 \to p\pi^-$ vertex reconstruction affects many aspects of the Λ^0 electromagnetic dipole moments measurement outlined in Section 1.4: on top of being fundamental to evaluate how much magnetic field the particle traversed (and thus the extent of spin precession), even the best momentum resolution for protons and pions is worthless if the particles are extrapolated at the wrong point of production. This section will therefore focus on biases in $\Lambda^0 \to p\pi^-$ vertexing affecting already reconstructed events. Since both $x_{\mathrm{vtx}}^{\Lambda}$ and $y_{\mathrm{vtx}}^{\Lambda}$ are fairly well reconstructed, with resolution $\lesssim 1\,\mathrm{cm}$ and no discernible bias, the focus will be on the reconstruction of $z_{\mathrm{vtx}}^{\Lambda}$. The following results are obtained from the complete simulated $\Lambda_b^0 \to J/\psi\,\Lambda^0$ dataset (see Section 2.5) after the full selection process detailed in Chapter 4, unless otherwise specified.

The distribution of $z_{\mathrm{vtx}}^{\Lambda}$ residuals for simulated signal events is shown in Figure 3.13a. Its shape is distinctly non-Gaussian, with a second core towards the positive end of the axis counterbalancing the expected ≈ 0 peak, confirming the presence of a median bias of $\approx 14\,\mathrm{cm}$. This number is of course much lower than the $\approx 40\,\mathrm{cm}$ median bias of Vertex-Fitter-converging events quoted in Table 3.2. Here not only am I directly selecting $z_{\mathrm{vtx}}^{\Lambda} > 5\,\mathrm{m}$, which reduces the extent of possible vertex bias given the position of the T stations around 8 m, but many selection steps are also in place to skim out most badly reconstructed events.

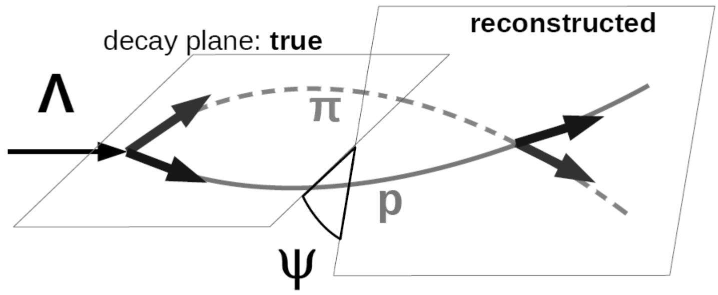

Figure 3.14: Definition of angle ψ as the angle between reconstructed and true $\Lambda^0 \to p\pi^-$ decay planes.

3.5.1 Ghost vertex events

The positive bias core can be interpreted as a mistake the vertexing algorithm commits when confronted with a specific decay geometry. When the $\Lambda^0 \to p\pi^-$ decay plane closely aligns with the xz bending plane, the bending induced by the magnet can produce either *opening* or *closing* tracks (depicted in the top and bottom diagrams respectively in Figure 3.15). In the latter case the tracks will cross again at $z > z^{\Lambda}_{\text{vtx}}$; if y displacement is sufficiently small, the algorithms may converge on this «ghost» vertex instead of the real one. This problem only affects physics analysis with T tracks as that's the only track classification for which the production vertex can be located after the dipole magnet, and thus the only case where the double crossing can occur.

To test out this hypothesis we define the auxiliary variable $\vec{a}$ as the cross product between proton and pion momenta at production vertex:

$$\vec{a} \coloneqq \vec{p}_p \times \vec{p}_\pi. \tag{3.35}$$

This vector is perpendicular to the $\Lambda^0 \to p\pi^-$ decay plane, a property which allows us to compute angle ψ between true and reconstructed decay planes, depicted in Figure 3.14, as the angle between $\vec{a}^{\text{true}}$ and $\vec{a}^{\text{DTF}}$ (the latter resulting from DTF momenta with J/ψ and Λ^0 mass constraints):

$$\psi = \arccos\left(\hat{a}_{\text{true}} \cdot \hat{a}_{\text{reco}}\right). \tag{3.36}$$

We also define the *horizontality* of a $\Lambda^0 \to p\pi^-$ event as follows:

$$h = \operatorname{sign}\left(\Lambda^0_{\text{PID}}\right) \operatorname{sign}\left(B_y\right) \frac{a_y}{|\vec{a}|}, \tag{3.37}$$

where $\operatorname{sign}(B_y)$ is the dipole magnet polarity[29] and $\operatorname{sign}(\Lambda^0_{\text{PID}})$ is the sign of

[29] The LHCb dipole magnet polarity is reversed roughly twice per month to allow for studies on decay asymmetries [80]. The $B_y > 0$ configuration is conventionally known as *magnet up* polarity, $B_y < 0$ as *magnet down*.

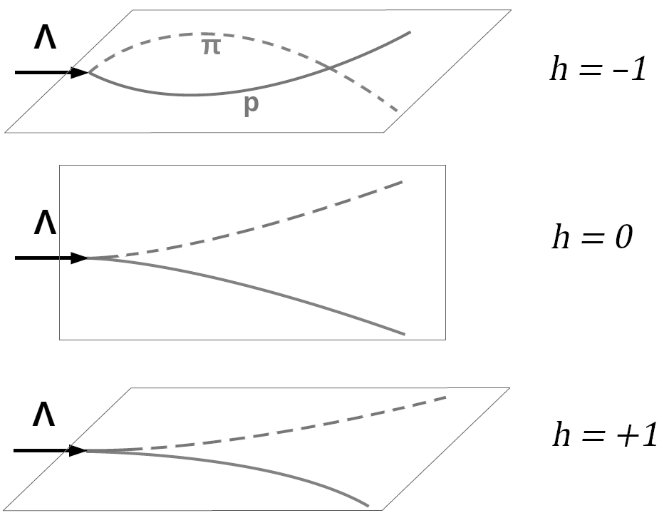

Figure 3.15: Depiction of three $\Lambda^0 \to p\pi^-$ configurations and the associated horizontality values. The horizontal planes in the top and bottom diagrams are aligned to the LHCb xz plane, the vertical plane in the middle diagram to the yz plane.

the PDG Monte Carlo particle numbering scheme of the mother particle (+1 for Λ^0, −1 for $\bar{\Lambda}^0$) [3]. Decays with $h = \pm 1$ lie exactly on the xz bending plane, $h = -1$ events having closing $p\pi^-/\bar{p}\pi^+$ tracks and $h = +1$ events having opening tracks, while $h = 0$ events lie on the yz plane (the three cases are represented in Figure 3.15).

The simplest case resulting in a ghost vertex is an opening-track $\Lambda^0 \to p\pi^-$ event fully lying on the xz plane, whereby y track distance is ≈ 0 throughout the particle lines of flight and the second crossing of the tracks is chosen as the reconstructed vertex; in such a case $h_{\text{true}} = -1$, $h_{\text{DTF}} = +1$ and $\psi = \pi$. Due to poor momentum resolution at the VF level, which fixes the vertex positions for the following DTF refits, this issue affects many more $h_{\text{true}} < 0$ topologies. This is clearly visible in Figure 3.16a: the $h_{\text{true}} < 0$, $\psi \leq 15$ deg region is depleted in favour of an arm-like structure stretching to high ψ values. No equivalent pattern for $h_{\text{true}} > 0$ is present because the vertex scan is performed starting from the T station measurements and moving upstream, converging on the first local minimum encountered; thus it's very unlikely for opening-track events to be reconstructed as closing-track events by selecting an upstream ghost vertex.

To study the impact of ghost vertex events, I have isolated the above struc-

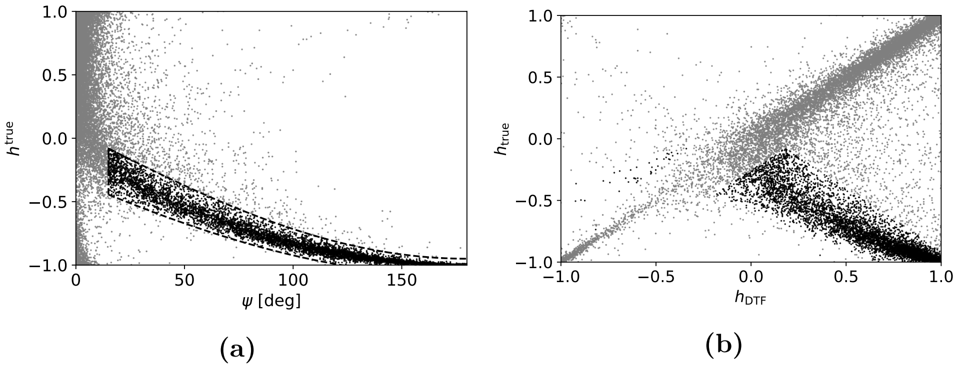

Figure 3.16: *(a)* Distribution of simulated $\Lambda_b^0 \to J/\psi\,\Lambda^0$ events as function of angle ψ defined as (3.36) and true horizontality h defined as (3.37). The *dashed lines* demarcates the ghost vertex locus of points defined in (3.38): events inside the region are marked in *black*. All selection steps are applied. *(b)* Distribution of the same events as function of true and reconstructed horizontality (the latter computed using momenta from the Decay Tree Fitter with J/ψ and Λ^0 mass constraints).

ture by parameterizing the locus of points

$$\Big\{ (\psi, h_{\rm true}) \in \mathbb{R}^2 : \psi \geq 15\,{\rm deg} \wedge f_{\rm bottom}(\psi) \leq h_{\rm true} \leq f_{\rm top}(\psi) \Big\}, \tag{3.38}$$

within the ad hoc horizontality region

$$f_{\rm top}(\psi) = \frac{1}{20} - \sin\frac{\psi\,[{\rm rad}]}{2}, \tag{3.39a}$$

$$f_{\rm bottom}(\psi) = -\frac{2}{25} - \sin\left(\frac{\pi}{12} - \frac{17}{40}\psi\,[{\rm rad}]\right). \tag{3.39b}$$

Events satisfying these requirements amount to 31.6% of the total simulated sample after all selection steps applied. Figure 3.16b highlights the isolated events in the $h_{\rm true}$–$h_{\rm DTF}$ plane, showing that the vast majority of them are $h_{\rm true} < 0$ events reconstructed as $h_{\rm DTF} > 0$ events[30].

The Λ^0 decay vertex residual distributions shown in Figure 3.17a confirm that ghost vertex events are largely responsible for the high-bias core observed in Figure 3.13a. Some asymmetry effects are still visible in the distribution without ghost vertices, with a leftover median bias of $\approx 5.2\,$cm. This suggests that further distorsion effects may be in place either in track reconstruction or in the fitting process and further investigation is warranted.

Ongoing studies conducted by the Milan and Valencia LHCb research groups suggest that ghost vertex convergence in double-crossing tracks can

[30] A pocketful of events are located in the bottom left quadrant, though hard to see due to the meager number. These are rare cases where reconstructed horizontality is lower than the true value due to the low momentum resolution of T tracks.

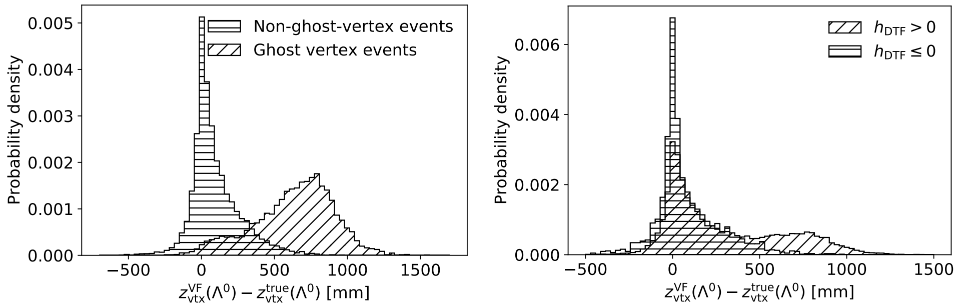

(a) **(b)**

Figure 3.17: Normalized distributions of $z_{\mathrm{vtx}}^{\Lambda}$ bias for simulated $\Lambda_b^0 \to J/\psi\,\Lambda^0$ events with all selection steps applied: *(a)* without (*horizontal hatching*) and with (*diagonal hatching*) Λ^0 ghost vertex, as selected in Figure 3.16a; *(b)* with $h_{\mathrm{DTF}} > 0$ (*horizontal hatching*) and $h_{\mathrm{DTF}} \leq 0$ (*diagonal hatching*), using DTF momenta with J/ψ and Λ^0 mass constraints.

be tempered by tweaking the initial vertex seed. The choice of seed defines the starting point for the Vertex Fitter algorithm: early results show that overriding the seeding process (see Section 3.1.1) to use the true $\Lambda^0 \to p\pi^-$ vertex as seed helps direct the VF towards the absolute χ^2 minimum and reduces the ghost vertex core seen in Figure 3.17a. A similar result could be achieved without access to Monte Carlo information by performing several vertex fits with seeds across the z range and implementing selection criteria to choose the best vertex among the ones found.

An alternative, more drastic approach would be to only retain $\Lambda^0 \to p\pi^-$ events with $h_{\mathrm{DTF}} \leq 0$. As seen from Figure 3.16b, this rejects virtually all ghost vertex events and yields an even lower median bias of $\approx 2.5\,\mathrm{cm}$ with a single cut on reconstructed variables (see Figure 3.17b). The ensuing 89% loss in $\Lambda_b^0 \to J/\psi\,\Lambda^0$ signal makes this solution impractical with Run 2 data, but viable as a last resort on the projected $50\,\mathrm{fb}^{-1}$ dataset at the end of Run 4.

For the purposes of this thesis, no cut on ghost vertex events is applied. Their impact on the resolutions for the proton angular distribution in $\Lambda^0 \to p\pi^-$ decays is studied in Section 5.2.1.

3.5.2 Very high bias events

Most $\Lambda_b^0 \to J/\psi\,\Lambda^0$ events, even those with ghost vertex reconstruction, still maintain a limited $\lesssim 1.0\,\mathrm{m}$ bias on $z_{\mathrm{vtx}}^{\Lambda}$. A smaller substructure with $\geq 2.0\,\mathrm{m}$ bias (median bias $\approx 6.0\,\mathrm{m}$) emerges when plotting the distribution in logarithmic scale, as seen in Figure 3.13b. These events only amount to $\approx 0.5\%$ of the sample after the full selection process. The fraction rises to $\approx 1.7\%$ when

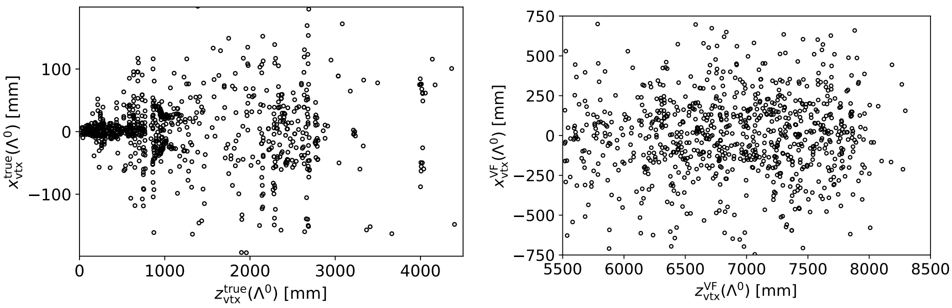

(a) **(b)**

Figure 3.18: Distribution of simulated $\Lambda_b^0 \to J/\psi\,\Lambda^0$ events (only prefilters applied) with $z_\Lambda^{\mathrm{VF}} - z_\Lambda^{\mathrm{true}} \geq 2.0\,\mathrm{m}$ as function of true *(a)* and reconstructed *(b)* $x_{\mathrm{vtx}}^{\Lambda}$ and $z_{\mathrm{vtx}}^{\Lambda}$. This corresponds to a top view of true and reconstructed Λ^0 decay vertices.

only the loose prefiltering selection from Section 4.1 is applied, meaning that most of these events are already rejected in the following selection steps. To maximize statistics, I studied this «very high bias» class of events omitting said steps.

Figure 3.18a provides a top view of the Λ^0 decay vertices for these events, showing the distribution of true $z_{\mathrm{vtx}}^{\Lambda}$ and $x_{\mathrm{vtx}}^{\Lambda}$. Most Λ^0 in high bias events decay in the earlier sections of the detector ($z < 3.0\,\mathrm{m}$); the high spatial concentration in specific regions of the xz plane, such as the «wings» around $z \approx 1.0\,\mathrm{m}$, as well as the consistency between the placement of these structures and the location of the different LHCb subdetectors (cf. Figure 2.2), suggest that they may be the result of interaction with the material.

No dedicated veto on reconstructed variables is possible to filter this class of events: Figure 3.18b shows that the Λ^0 vertices are reconstructed in seemingly arbitrary positions. Their impact on the overall performance on signal is nevertheless neglectable.

3.6 Summary and closing remarks

Since T tracks have seen no usage so far in in physics analyses at LHCb, vertex reconstruction involving this class of tracks has never been the subject of in-depth scrutiny. Given the number of different topics tackled in the present chapter, in this section I offer a more succint recount of the main findings and outline the solutions I have adopted for the remainder of this thesis.

One major challenge to a competitive measurement of Λ^0 electromagnetic dipole moments using the exclusive $\Lambda_b^0 \to J/\psi\,(\to \mu^+\mu^-)\,\Lambda^0\,(\to p\pi^-)$ decay is the $\lesssim 50\%$ efficiency of the Λ^0 and Λ_b^0 vertex reconstruction process, effectively halving the potential signal yield. Topological studies on reconstruction of the $\Lambda^0 \to p\pi^-$ decay in non-converged events expose that the failure of the Vertex Fitter algorithm is caused by the oscillation of the Λ^0 candidate vertex throughout the iterating process, preventing fulfilment of either of convergence conditions (3.14) and (3.15).

Another widespread characteristic of non-converged events is the discrepancy in z coordinate between the point of closest track distance in the xz plane (where tracks are curved due to the magnetic field) and the crossing track point in the yz plane (where tracks are approximately straight lines). The distance between the two, sometimes exceeding 1 m, is consistent with the scale of candidate vertex oscillation in the VF iterating process. This suggests that, at least for a portion of non-converged events, the Vertex Fitter locates two irreconcilable vertex candidates in the xz and yz track propagation planes and is unequipped to choose one over the other.

To address this problem, I developed and implemented a threefold refit process that sequentially favours yz, xz and xy propagation planes by increasing the complementary uncertainty (σ_x, σ_y and σ_z respectively) in the vertex covariance matrix. This results in a +26.4% increase in signal statistics compared to only using the standard Vertex Fitter, recovery roughly one quarter of all non-converged $\Lambda_b^0 \to J/\psi\,\Lambda^0$ events.

The reason for the xz-yz discrepancy, and thus of the oscillation at the heart of vertexing failure, is currently unknown. However, an observed systematic underestimation of p_z for pion tracks in non-converged events suggests it could be linked to poor momentum measurement at T station level. The negative p_z bias affects recovered events as well, imprinting a median bias on z_{vtx}^{Λ} roughly 20 cm greater than standard converged events. Recovered events also have generally worse $\tilde{\chi}^2_{\text{vtx}}$; dedicated studies on algorithm performances point to this being a problem with the event themselves being difficult to fit, rather than to issues with the algorithms.

Given the importance of $\Lambda^0 \to p\pi^-$ vertex bias for the measurement of the Λ^0 dipole moments, I also investigated the reconstruction of the aforementioned decay and identified two main classes of biased events. «Ghost vertex» events are a byproduct of the action of the dipole magnet, which bends proton and pion tracks into a second crossing point mistakenly chosen as the $p\pi^-$ production vertex. These events comprise almost one third of the full dataset and contribute a median 70 cm bias in z_{vtx}^{Λ}; their effect on proton angular resolution is the focus of a study in Section 5.2.1. «Very high bias» events contribute a much larger median bias of 6 m and cannot be singled out using only reconstructed variables, but their impact on the $\Lambda_b^0 \to J/\psi\,\Lambda^0$ analysis is considered to be neglectable, as they only amount to 0.5% of the simulated sample after the full selection process.

Chapter 4

Signal event selection

This chapter outlines the three major steps in the selection of $\Lambda_b^0 \to J/\psi\,\Lambda^0$ events for the study of long-lived Λ^0 baryons in LHCb. Section 4.1 discusses the preliminary kinematic variable selections used to provide a loose selection of signal for further analysis; Section 4.2 gives an overview of the two vetoes used to account for the main source of physical background, the $B^0 \to J/\psi\,K_S^0$ decay; Section 4.3 details my work towards the training, optimization and evaluation of a supervised learning multivariate classifier to perform signal-background discrimination; finally, Section 4.4 brings together all three selection techniques to give proof of $\Lambda_b^0 \to J/\psi\,\Lambda^0$ reconstructibility, fitting the filtered $J/\psi\,\Lambda^0$ invariant mass distributions from simulated signal and Run 2 data.

4.1 Prefiltering

Prefilters, also refered to as *preliminary selections* or simply *pre-selections*, are the foundation of the signal selection process. The main objective of this step is to improve the signal-to-background ratio and reduce the computational workload to analyze data with cuts on kinematic variables.

The most impactful selection at this step is the one applied to $z_{\mathrm{vtx}}^{\Lambda}$, the z component of the $\Lambda^0 \to p\pi^-$ decay vertex, which is required to be in the $[5.5\,\mathrm{m}, 8.5\,\mathrm{m}]$ range. The efficiencies for the left and right cuts as a function of the threshold are shown in Figure 4.1; despite the significant $\approx 68\%$ loss of reconstructed $\Lambda_b^0 \to J/\psi\,\Lambda^0$ events, the $z_{\mathrm{vtx}}^{\Lambda} \geq 5.5\,\mathrm{m}$ cut cannot be avoided as it is required that Λ^0 decay after the dipole magnet in order to observe spin precession.

Other prefilter criteria have a much lower impact on signal, with efficiencies $\gtrsim 80\%$. These include cuts on: transverse momenta of proton and Λ^0, designed to weed out contributions from low-p_{T} secondary collisions; invariant masses

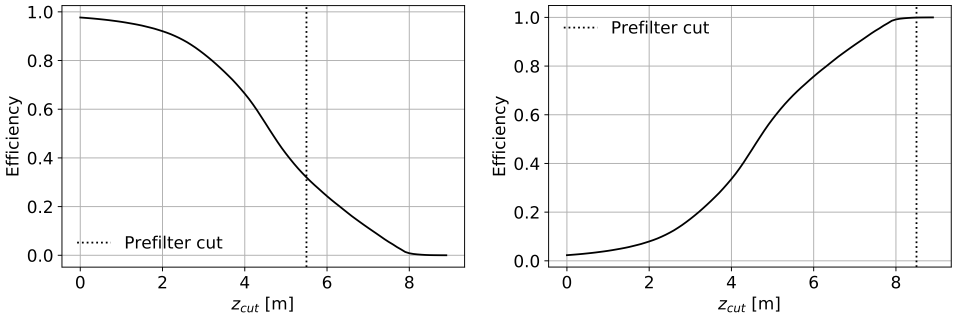

(a) **(b)**

Figure 4.1: Efficiency of the $z^{\Lambda}_{\text{vtx}} \geq z^{\text{left}}_{\text{cut}}$ *(a)* and $z^{\Lambda}_{\text{vtx}} \leq z^{\text{right}}_{\text{cut}}$ *(b)* prefilter selection criteria on $\Lambda^0_b \to J/\psi\,\Lambda^0$ simulated signal, as function of the respective thresholds. The *dotted vertical lines* mark the chosen thresholds.

of $p\pi^-$, $\mu^+\mu^-$ and $J/\psi\,\Lambda^0$, roughly selecting the regions of interest surrounding the mother particle resonances; the cosine of pointing angle ξ_p of Λ^0 and Λ^0_b, defined as the angle between the line connecting a particle's origin and decay vertices and the direction of its momentum computed from the decay products (this helps to recognize real decays); $\Delta\chi^2_{\text{PV}}$ and $\tilde{\chi}^2_{\text{vtx}}$ for Λ^0_b and Λ^0, with $\Delta\chi^2_{\text{PV}}$ being the increase of the primary vertex χ^2 when the particle is included in the fit (helping to weed out particles from secondary interactions) and $\tilde{\chi}^2_{\text{vtx}}$ being the χ^2 of the reconstructed particle decay vertex; the geometrical distance $\chi^2_{\text{dist}}(\Lambda^0)$ between the primary vertex and the Λ^0 decay vertex, expressed in χ^2 units. Details on the applied prefilter criteria are listed in Appendix A. Factoring in the z^{Λ}_{vtx} cuts, the prefilter has an estimated $\approx 26\%$ efficiency on $\Lambda^0_b \to J/\psi\,\Lambda^0$ signal.

As detailed in Section 2.2.1, a key aspect of this analysis is the employment of T tracks for the reconstruction of the Λ^0. The low residual magnetic field for protons and pions produced far from the dipole magnet lowers momentum resolution for the associated tracks down to 20–30%. Resolution can be improved up to $\approx 10\%$ by placing kinematic constraints on $p\pi^-$ and $\mu^+\mu^-$ invariant masses, fixing them to the PDG values of $m(\Lambda^0)$ and $m(J/\psi)$ respectively (these will be henceforth referred to as *mass constraints*). This approach cannot be implemented in the leaf-by-leaf framework of the default Vertex Fitter algorithm for vertex reconstruction; instead each event is refitted with the Decay Tree Fitter (DTF) algorithm in two configurations, single J/ψ and double $J/\psi\,\Lambda^0$ mass constraints (see also Section 3.1.2).

A convergence requirement of the DTF algorithm with the $J/\psi\,\Lambda^0$ mass constraints is therefore added to the prefilter selections. The main drawback of this selection, a steep 45% efficiency on simulated signal events (although raised to 65% when only considering events passing the non-DTF prefilters), is outweighed by the benefits of the improved momentum resolution in the determination of the angular distribution of $\Lambda^0 \to p\pi^-$ decay products.

4.2 Physical background rejection

The main source of physical background for the $\Lambda_b^0 \to J/\psi\ (\to \mu^+\mu^-)\ \Lambda^0\ (\to p\pi^-)$ decay is the similar

$$B^0 \to J/\psi\ (\to \mu^+\mu^-)\ K_S^0\ (\to \pi^+\pi^-). \tag{4.1}$$

The final states of the two decays only differ for a $p \leftrightarrow \pi^+$ change. The K_S^0 meson also has comparable mean lifetime to the Λ^0, thus we expect a sizeable number of K_S^0 decaying after the dipole magnet. To top it off, the B^0 mass ($5279.65\,\mathrm{MeV/c^2}$) is fairly close to that of Λ_b^0 ($5619.60\,\mathrm{MeV/c^2}$) [3], muddying the waters in invariant mass fits.

As discussed in Section 2.2.2, the LHCb detector employs the two RICH systems to identify and distinguish between protons, pions and kaons; in the case of Λ^0 decaying after the dipole magnet RICH1 contributions is impossible, but information from RICH2 would still be available for the vast majority of the decays at hand. Unfortunately, this is where the experimental nature of physics analyses with T tracks becomes relevant once again: due to technical issues in the implementation, RICH2 information for particle identification is currently unavailable for T tracks recorded during LHC Runs 1 and 2[31], making $B^0 \to J/\psi\, K_S^0$ discrimination much more difficult.

4.2.1 Invariant mass veto with pion mass hypothesis

For the first step in B^0 background rejection, all events are refit with the Decay Tree Fitter algorithm using J/ψ and K_S^0 invariant mass constraints and a $p \to \pi^+$ mass hypothesis, i.e. assuming that the proton is a misclassified pion and fitting the entire decay tree as such. The veto rejects an event if the DTF refit converges and $m(J/\psi\ K_S^0)$ is too close in value to the B^0 PDG mass, that is

$$|m(J/\psi\ K_S^0) - m_{\mathrm{PDG}}(B^0)| < m_{\mathrm{thres}}, \tag{4.2}$$

with tunable threshold m_{thres}.

This approach was tested on simulated $\Lambda_b^0 \to J/\psi\,\Lambda^0$ and $B^0 \to J/\psi\,K_S^0$ samples. The variable $m(J/\psi\ K_S^0)$ was chosen as opposed to $m(\pi^+\pi^-)$ due

[31] A large effort by the Milan and Valencia LHCb research groups is underway at the time of writing to implement RICH2 information in T track trigger lines for Run 3.

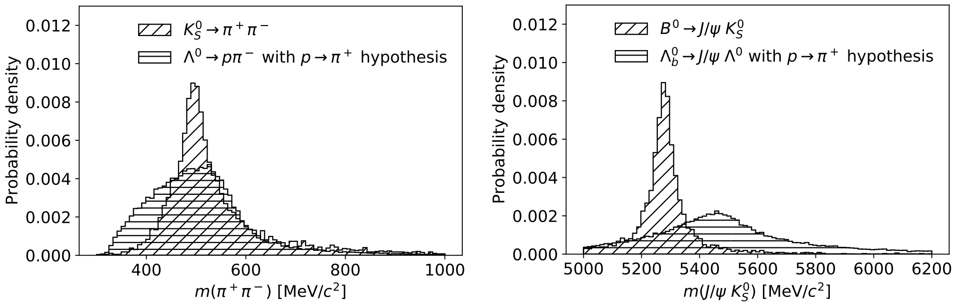

(a) **(b)**

Figure 4.2: Comparison of simulated $m(\pi^+\pi^-)$ *(a)* and $m(J/\psi\ K_S^0)$ *(b)* distributions: $\Lambda_b^0 \to J/\psi\, \Lambda^0$ events with $p \to \pi^+$ mass hypothesis are labeled by *horizontal hatching*, $B^0 \to J/\psi\, K_S^0$ events by *diagonal hatching*.

to the significant overlap between $m(\pi^+\pi^-)$ invariant mass distributions of actual $K_S^0 \to \pi^+\pi^-$ events and $\Lambda^0 \to p\pi^-$ events with $p \to \pi^+$ mass hypothesis (Figure 4.2a); the $m(J/\psi\ K_S^0)$ distributions are comparatively more separate (Figure 4.2b), allowing for a better selection on the variable.

Figure 4.3a shows the veto efficiency on $\Lambda_b^0 \to J/\psi\, \Lambda^0$ signal and $B^0 \to J/\psi\, K_S^0$ physical background as function of the threshold m_{thres}. I optimized m_{thres} to maximize signal significance

$$\frac{S}{\sqrt{S+B}}. \tag{4.3}$$

Usually S and B would be the signal and background event counts after the selection; since yields in Run 2 data are still unknown at this selection step, I instead used the fraction of total signal and physical background events after prefilter selections also passing the invariant mass veto with a specific threshold. Signal significance as function of the threshold is depicted in Figure 4.3b; the chosen value of $m_{\text{thres}} = 70\,\text{MeV}$ retains 87% of signal while rejecting 64% of background.

4.2.2 Armenteros-Podolanski veto

To supplement the invariant mass veto, I introduced a selection criterium on proton and pion momenta based on the Armenteros-Podolanski technique [81] to be applied in conjunction, as part of the global strategy to filter out $B^0 \to J/\psi\, K_S^0$ events. This approach, first proposed in 1954, allows for momentum-based discrimination of $\Lambda^0 \to p\pi^-$ and $K_S^0 \to \pi^+\pi^-$ decays without the need for mass assumptions on the daughter particles.

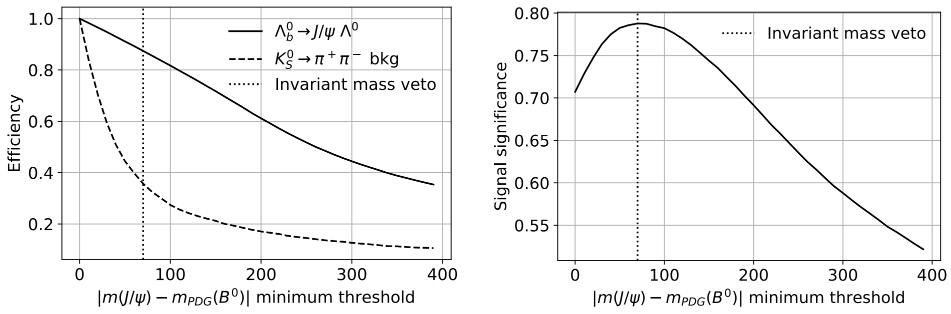

(a) **(b)**

Figure 4.3: *(a)* Efficiency of physical background veto as a function of the invariant mass discrepancy threshold on simulated signal ($\Lambda_b^0 \to J/\psi\,\Lambda^0$, *solid*) and background ($B^0 \to J/\psi\,K_S^0$ with proton mass hypothesis, *dashed*) events. *(b)* Signal significance as a function of the $m(J/\psi\,\Lambda^0)$ threshold. The chosen threshold in both plots is marked by the *dotted line*.

Let $M \to m_1 m_2$ be a two-body decay, shown in the laboratory frame in Figure 4.4a; given the mother particle line of flight, we define longitudinal momentum p_L and transverse momentum p_T for the two daughter particles, with $p_\mathrm{T}^{(1)} = -p_\mathrm{T}^{(2)} \equiv p_\mathrm{T}$. These quantities can be expressed in terms of their values in the center-of-mass frame of the decay (Figure 4.4b) with a Lorentz β boost along the M momentum:

$$p_\mathrm{L} = \gamma\left(p_\mathrm{L}^\star + \beta E^\star\right) \tag{4.4a}$$
$$p_\mathrm{T} = p_\mathrm{T}^\star. \tag{4.4b}$$

Energy $E^\star$ of the daughter particles in the center-of-mass frame are known for two-body decays to be

$$E_1^\star = \frac{1}{2M}\left(M^2 + m_1^2 - m_2^2\right), \tag{4.5a}$$
$$E_2^\star = \frac{1}{2M}\left(M^2 - m_1^2 + m_2^2\right) \tag{4.5b}$$

In turn, $p_\mathrm{L}^\star$ and $p_\mathrm{T}^\star$ are related to the momentum modulus $p^\star := |\vec{p}^{\,\star}|$ of the daughter particle, which is fixed by two-body decay kinematics, via the angle θ between $\vec{p}^{\,\star}_{(1)}$ and $\vec{\beta}$:

$$p_\mathrm{L}^\star = \pm p^\star \cos\theta, \tag{4.6a}$$
$$p_\mathrm{T}^\star = p^\star \sin\theta. \tag{4.6b}$$

The Armenteros-Podolanski technique exploits the predictable physics of a

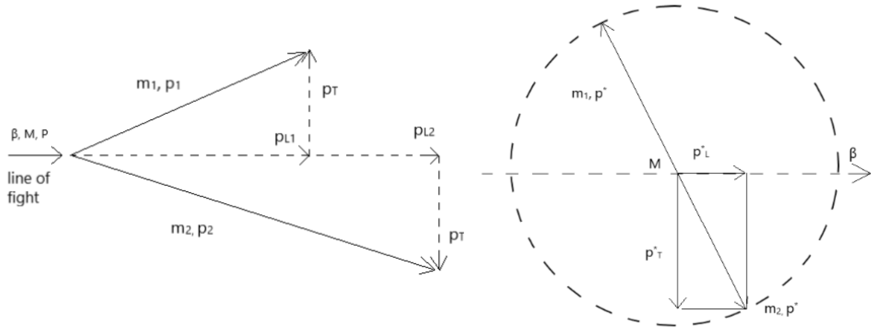

(a) **(b)**

Figure 4.4: Two-body decay kinematics in the laboratory *(a)* and center-of-mass *(b)* reference frames [82].

two-body decay in the Armenteros-Podolanski space defined by the longitudinal momentum asymmetry

$$\alpha \coloneqq \frac{p_{\mathrm{L}}^{(1)} - p_{\mathrm{L}}^{(2)}}{p_{\mathrm{L}}^{(1)} + p_{\mathrm{L}}^{(2)}}, \tag{4.7}$$

and transverse momentum p_{T} of the decay. Substituting (4.4a), (4.6) and (4.5) into (4.7) we obtain

$$\alpha = \frac{m_1^2 - m_2^2}{M^2} + \frac{2p^\star}{\beta M}\cos\theta \equiv \alpha_0 + \frac{r_\alpha}{\beta}\cos\theta, \tag{4.8}$$

with

$$\alpha_0 \coloneqq \frac{m_1^2 - m_2^2}{M^2} \tag{4.9}$$

and

$$r_\alpha \coloneqq \frac{2p_\star}{M}. \tag{4.10}$$

Result (4.8) can further be combined with (4.6b) through the Pythagorean trigonometric identity

$$\cos^2\theta + \sin^2\theta = 1, \tag{4.11}$$

yielding

$$\frac{(\alpha - \alpha_0)^2}{r_\alpha^2} + \frac{p_{\mathrm{T}}^2}{p^{\star 2}} = 1. \tag{4.12}$$

We have thus shown that momenta of daughter particles from a two-body decay define an ellipse in the α–p_{T} Armenteros-Podolanski space, with center

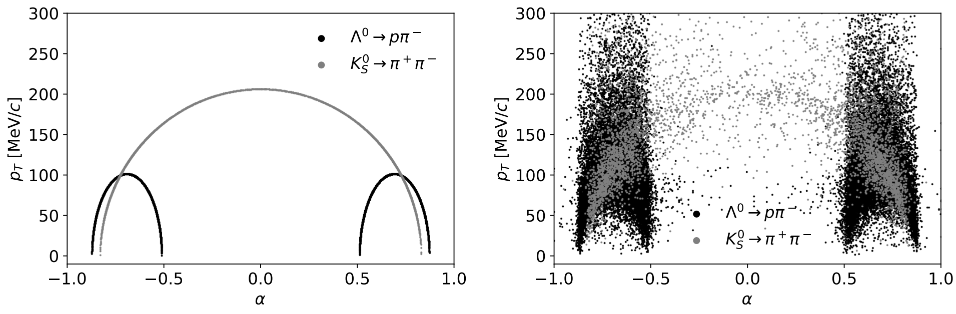

(a) **(b)**

Figure 4.5: Armenteros-Podolanski plots for simulated $\Lambda_b^0 \to J/\psi\,\Lambda^0$ (*black*) and $B^0 \to J/\psi\,K_S^0$ (*grey*) events, using true momenta *(a)* and Decay Tree Fitter momenta with J/ψ mass constraint *(b)*. Longitudinal p_L and transverse p_T momenta are defined here with respect to the Λ^0/K_S^0 lines of flight, with p_L asymmetry α defined as in equation (4.7).

and radii depending on particle masses and momentum distributions. This is verified in Figure 4.5a, which shows the α–p_T scatterplot of $\Lambda^0 \to p\pi^-$ ($K_S^0 \to \pi^+\pi^-$) decays from simulated $\Lambda_b^0 \to J/\psi\,\Lambda^0$ ($B^0 \to J/\psi\,K_S^0$) events, computed with true momenta. In this case α is conventionally computed assigning the positive particle to m_1, which corresponds to p in Λ^0 decays and π^+ in $\bar{\Lambda}^0$ and K_S^0 decays, leading to the two symmetrical ellipses for the $\Lambda_b^0 \to J/\psi\,\Lambda^0$ events.

While a selection criterium based on the K_S^0 and Λ^0 ellipses would appear trivial, momentum resolution needs to be taken into account. Figure 4.5b shows the Armenteros-Podolanski space for the same events using momenta reconstructed with the Decay Tree Fitter algorithm with J/ψ mass constraint[32]. The significant overlap of the two classes of events prevents selection criteria on the p_T axis, but still allows for a criterium on α relatively devoid of false positives.

Given the symmetrical nature of the Armenteros-Podolanski space, I implemented the veto in the form

$$|\alpha| \geq \alpha_\mathrm{thres}. \tag{4.13}$$

Similary to the B^0 veto, I optimized the α_thres threshold to maximize $\Lambda_b^0 \to J/\psi\,\Lambda^0$ signal significance defined in (4.3), considering baseline signal and

[32]While the additional Λ^0 mass constraint used so far drastically improves momentum resolution in $\Lambda_b^0 \to J/\psi\,\Lambda^0$ events, applying it to $B^0 \to J/\psi\,K_S^0$ events is detrimental as it distorts the Armenteros-Podolanski phase space, making $K_S^0 \to \pi^+\pi^-$ events overlap with the $\Lambda^0 \to p\pi^-$ ellipses.

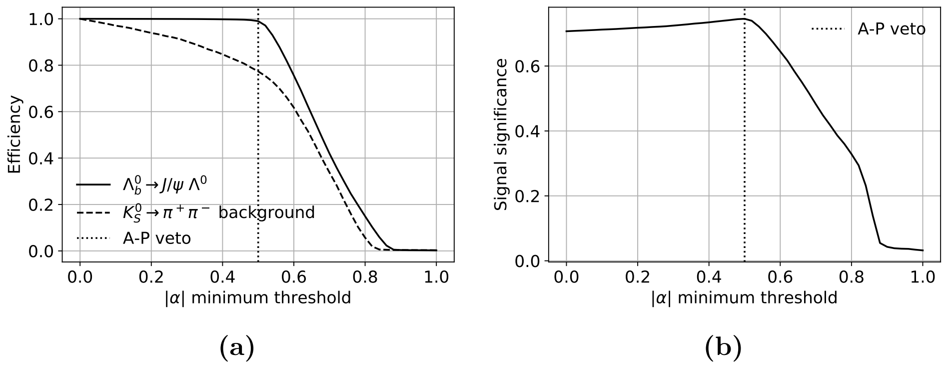

Figure 4.6: *(a)* Efficiency of Armenteros-Podolanski veto as a function of the $|\alpha|$ threshold on simulated signal ($\Lambda_b^0 \to J/\psi\,\Lambda^0$, *solid*) and background ($B^0 \to J/\psi\,K_S^0$, *dashed*) events. *(b)* Signal significance as a function of the $|\alpha|$ threshold. The chosen threshold in both plots is marked by the *dotted line*.

background events passing prefilters and the B^0 veto selection. Figure 4.6a shows the signal and background efficiencies of the veto as a function of α_{thres}, while Figure 4.6b reports the corresponding signal significances. The chosen threshold of 0.5 retains 99% of the $\Lambda_b^0 \to J/\psi\,\Lambda^0$ signal while rejecting 23% of $B^0 \to J/\psi\,K_S^0$ background surviving the B^0 veto. In addition, the Armenteros-Podolanski veto will also remove combinatorial $K_S^0 \to \pi^+\pi^-$ events which the B^0 veto, being based on the $J/\psi\,K_S^0$ invariant mass, is not equipped to deal with.

4.3 HBDT classifier

Even after prefilter selections, combinatorial background exceeds the signal by a 10^3 factor. This section details my work in training and testing a multivariate classifier to discriminate $\Lambda_b^0 \to J/\psi\,\Lambda^0$ events, in order to lower the signal-to-background ratio to acceptable levels for physics analysis. After taking into consideration a wide range of classifiers, a histogram-based gradient boosting classification tree (also referred to as *histogram-based boosted decision tree*, HBDT for short) was chosen by virtue of its superior performance in studies on sample data [83]. Training, optimization and performance testing of the classifier were made with the Scikit-learn 0.24.2 package [84] for Python 3.6.8 [85].

The basic layout of a binary decision tree classifier is sketched in Figure 4.7: a sequence of decision nodes applies binary conditions according to available information on the individual event and eventually reaches a leaf node associated to the *event score* t, in this case the probability that the event is a

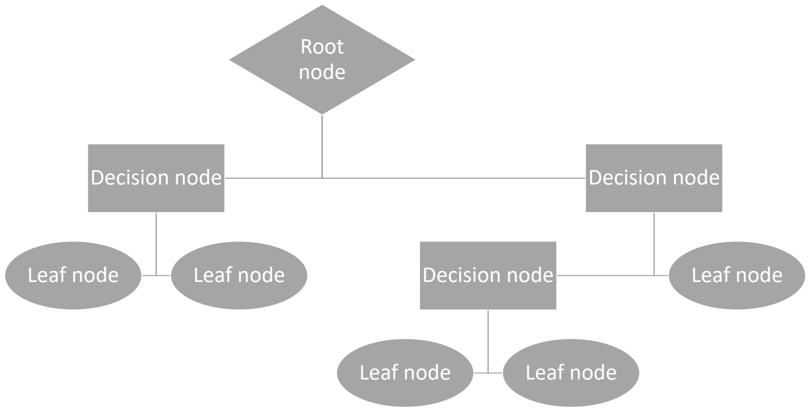

Figure 4.7: Diagrammatic representation of a decision tree classifier.

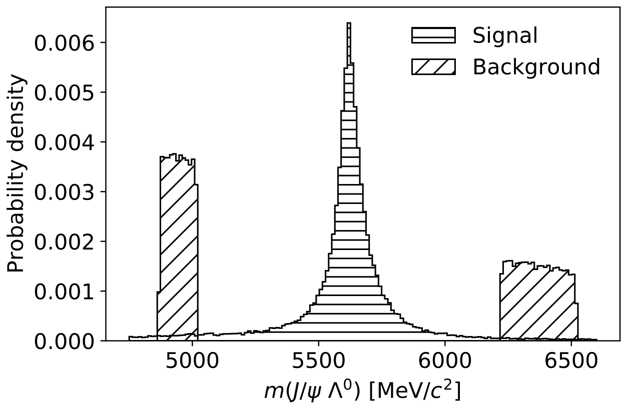

Figure 4.8: Signal (*horizontal hatching*) and background (*diagonal hatching*) data samples used for training the HBDT classifier.

$\Lambda_b^0 \to J/\psi\,\Lambda^0$ decay. Performance of the decision tree can be enhanced with *boosting* [86], whereby the ultimate classifier is built as a weighted average of a large number of weaker trees; the result is known as a boosted decision tree (BDT). In the adaptive boosting (AdaBoost) implementation used in this thesis, each tree T_k is trained on a reweighted data sample that prioritizes events misclassified by tree T_{k-1}. The usage of a histogram-based BDT, arranging input samples into integer-valued bins, allows for much faster estimators when working with large data samples ($n \gtrsim 10^4$).

4.3.1 Training and testing data

Supervised training of a classifier requires signal and background datasets as input to learn to distinguish between the two classes. For signal I used simulated $\Lambda_b^0 \to J/\psi\,\Lambda^0$ events, while for the background I sampled side bands on the left ($[4870.2\,\mathrm{MeV/c^2}, 5020.2\,\mathrm{MeV/c^2}]$) and right ($[6220.2\,\mathrm{MeV/c^2}, 6520.2\,\mathrm{MeV/c^2}]$) of the expected Λ_b^0 peak in the Run 2 data $m(J/\psi\,\Lambda)$ distribution (see Figure 4.8).

I considered two options for the signal-to-background ratio:

- *balanced* training dataset: $\approx 145\,000$ events, evenly split between signal and background;
- *unbalanced* training dataset: $\approx 73\,000$ signal events, ≈ 3.6 million background events.

The standard approach to machine learning calls for a roughly balanced dataset to train the classifier on signal and background alike. Given the disproportionate signal-to-background ratio in the case at hand, however, I also explored the unbalanced approach, aiming for improved background rejection at the price of (reasonably) subpar signal identification. Classifiers trained with balanced or unbalanced datasets showed very similar performances after score threshold optimization (see Section 4.3.4), the main difference being that balanced HBDTs require harsher score selection criteria; since no reason surfaced to favour either approach, I opted to follow the more conventional path and empolyed a balanced training dataset. Testing data for performance evaluation was sampled from the same pool as training data in a 1:9 ratio.

The following kinematic variables (also known as *features*) were used for signal discrimination: transverse and longitudinal momenta of p, π^- and J/ψ; coordinates of the $\Lambda^0 \to p\pi^-$ vertex position; Λ_b^0 and Λ^0 pointing angles ξ_p, i.e. the angle between the particle line of flight and its momentum; $\tilde{\chi}^2_{\mathrm{vtx}}$ of the $\Lambda_b^0 \to J/\psi\,\Lambda^0$ and $\Lambda^0 \to p\pi^-$ vertices; the increase $\Delta\chi^2_{\mathrm{PV}}$ of the primary vertex χ^2 when a particle is included in the fit, for Λ_b^0 and Λ^0; the distances χ^2_{dist} between Λ_b^0 and Λ^0 decay vertices and the primary vertex in χ^2 units. Distributions of the above variables for signal and background in training data are reported in Appendix B.

The momenta for proton and pion are computed with J/ψ mass constraints. While the usage of p, π^- momenta from the Decay Tree Fitter with the additional Λ^0 mass constraint was considered, preliminary tests on classifiers showed a slight degradation of their performance when the double mass constraint was adopted. The standard Vertex Fitter momenta were used for the J/ψ on account of the already great resolution provided by using muons reconstructed as Long tracks.

4.3.2 Hyperparameter optimization

The supervised training process for a classifiers tunes a set of parameters to minimize a given loss function; in the HBDT case, decision node and tree weights are trained according to the output of a logistic loss function. In contrast, *hyperparameters* are parameters governing the learning process itself and thus require separate optimization.

I selected three hyperparameters for optimization:

- learning rate $L \in [0.003, 0.006, 0.010, 0.015]$, the shrinkage factor for the contribution of each tree in the boosting process.
- maximum number of boosting iterations $n_{\max}^{\text{iter}} \in [1500, 2500, 5000]$;
- maximum number of leaves for each tree $n_{\max}^{\text{leaves}} \in [100, 200, 400, 800]$.

Other hyperparameters, such as the maximum number of bins and the minimum number of samples per leaf, were left as the default values of the Scikit-learn implementation.

I performed an exhaustive grid scan of the aforementioned hyperparameter values. Each classifier was evaluated on training data using a stratified k-folds cross validation technique: the training sample is split in $k = 5$ subsamples, the classifier is trained in rotation on $k-1$ samples and tested with the k-th, and the k results are averaged together. For a given score threshold i, we define *precision* P_i and *recall* R_i in terms of the true/false positive/negative rates: precision

$$P_i = \frac{n_{\text{TP}}}{n_{\text{TP}} + n_{\text{FP}}} \tag{4.14}$$

scores how often the classifier mistakes background for signal, while recall

$$R_i = \frac{n_{\text{TP}}}{n_{\text{TP}} + n_{\text{FN}}} \tag{4.15}$$

scores how well the classifier is able to recognize the signal. Performance of cross-validated classifiers on training and testing sub-samples[33] was evaluated using the *average precision* figure of merit

$$\text{AP} = \sum_{i=2}^{n} (R_i - R_{i-1}) P_i \tag{4.16}$$

for a set of n thresholds.

[33]Still working within a cross-validation mindset, here *testing data* is used to refer to the k-th fold in the cross-validation. No actual testing data as defined in Section 4.3.1 was used for the hyperoptimization step.

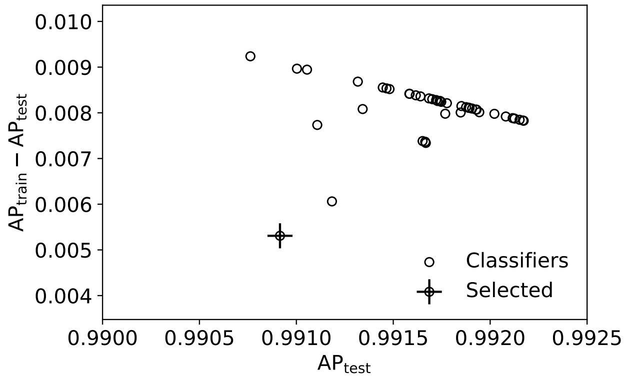

Figure 4.9: Trained HBDT classifiers as a function of the average precision score AP_{test} on test sample and diference $AP_{train} - AP_{test}$ in average precision on training and test samples. The hyperparameter-optimized model used for this thesis is marked with a *cross*.

To select the best classifier, I applied a hard cut on the average precision score on the test sample ($AP_{test} > 0.99$) and chose the model with the least difference in AP score between training and test samples ($AP_{train} - AP_{test} \approx 0.005$). The aim was to strike a balance between the raw performance of the classifier, graded with AP_{test}, and the prevention of significant overtraining, which reflects on $AP_{train} - AP_{test}$. The HBDT classifier used for the remainder of this thesis, with $L = 0.003$, $n_{max}^{iter} = 2500$, and $n_{max}^{leaves} = 100$, is the result of this selection process and highlighted in Figure 4.9.

4.3.3 Performance test

Performance of the trained HBDT optimized as per Section 4.3.2 was evaluated on the smaller test sample described in Section 4.3.1. Figure 4.10 shows the confusion matrices for training and test data with a score threshold of $t_{thres} = 0.5$, meaning events with $t > t_{thres}$ are classified as signal. The matrices summarize the true/false positive/negative rates for the classifier, highlighting the expected slight dip in accuracy when moving from training to test sample.

Comparing the signal and background score distributions (Figures 4.11a and 4.11b respectively) for training and test data samples, I observed a light discrepancy at the end tails. Such a split in favour of performance on training data is usually an early indicator of ovetraining. I investigated this possibility by conducting a two-sample Kolmogorov-Smirnov (K-S) test [87], which computes the probability p that two samples are drawn from the same probability distribution. Conventionally, the K-S is considered passed if $p > 0.05$; this was true for both signal ($p_{sig} \approx 0.30$) and background ($p_{bkg} \approx 0.07$), confirming

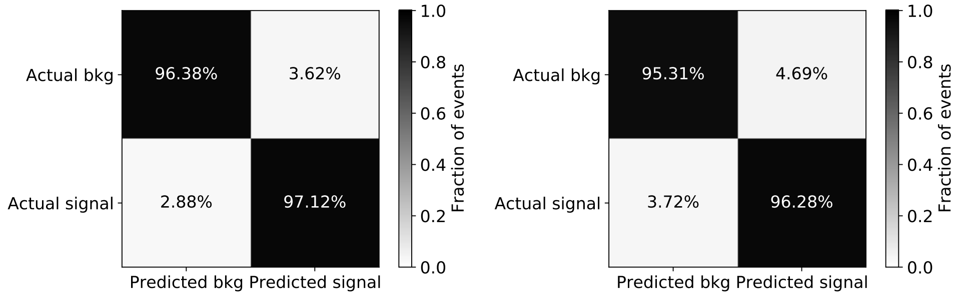

(a) **(b)**

Figure 4.10: Confusion matrices visualizing the performance of the HBDT classifier on training *(a)* and testing *(b)* data samples. Percentages and chromatic scale are normalized to the true event classification: for instance, the top left and top right quadrants of a matrix represent the fraction of true background events reconstructed as background or signal, respectively. Binary classification uses an illustrative response threshold $t_{\text{thres}} = 0.5$.

that the classifier is not significantly ovetrained.

I assessed the classifier performance at different thresholds using the receiving operating characteristic (ROC) and precision-recall curves. The ROC curve, depicted in Figure 4.12a, plots the true positive versus false positive rates for a set of thresholds left as hidden variables: a random classifier would bisect the plot plane, while a perfect classifier would adhere to the axes and cross the $(0, 1)$ point. The integral below the curve is itself a figure of merit, the area-under-curve (AUC), with better classifiers scoring values closer to unity. The precision-recall curve follows a similar principle to the ROC curve, plotting precision (4.14) and recall (4.15) for different thresholds; in this case, a perfect classifier would cross the $(1, 1)$ point. In both instances, the classifier shows great performance and high consistency between training and test samples.

Finally, I evaluated the importance of selected features in signal discrimination. This was achieved by permutating the values of each feature at a time and evaluating the average decrease in the baseline AP score of the classifier over ten of such permutations. Results are shown in Figure 4.13 for training and testing samples: in both cases the most discriminating features, causing the largest drops in AP, are the transverse momentum of the proton, the pointing angle of the Λ_b^0 and the increase in the primary vertex χ^2 when including the Λ_b^0 in the fit.

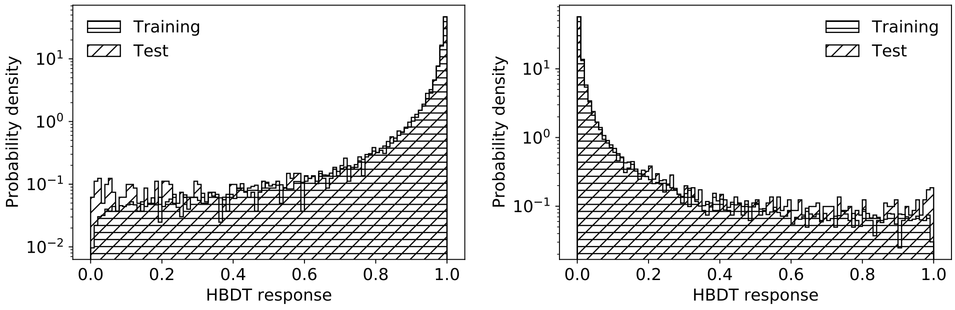

(a) **(b)**

Figure 4.11: Response distribution of the HBDT classifier on signal *(a)* and background *(b)* events. The training sample is represented by *horizontal hatching*, the test sample by *diagonal hatching*.

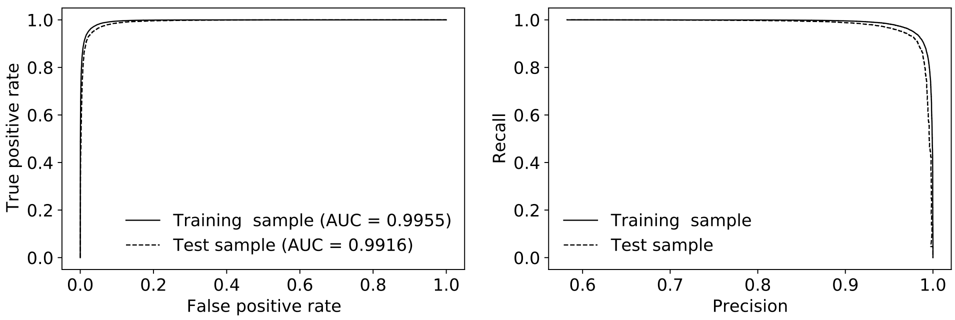

(a) **(b)**

Figure 4.12: Receiving operating characteristic (ROC) curve *(a)* and precision-recall curve *(b)* for the HBDT classifier on training (*solid*) and test (*dashed*) samples. The legend in the ROC plot includes the area-under-curve (AUC) score.

4.3.4 Threshold optimization

The final step in the classifier tuning process was the optimization of the threshold to maximize signal significance (4.3) after the HBDT filter. A simple way to do it would be to fit the $J/\psi\,\Lambda^0$ invariant mass distribution of filtered data with signal and background functions and extract the corresponding rates via integration; however, this has the undesired side effect of heightening the risk of biasing the selection towards our specific data sample.

A different, more general approach was devised to prevent this. I first identified a «soft» score threshold $t_{\text{thres}} = 0.7$, just high enough for the filtered Run 2 data $m(J/\psi\,\Lambda^0)$ distribution (using values from Decay Tree Fitter with mass constraints on both Λ_b^0 daughters) to show the Λ_b^0 resonance peak. I fit the simulated signal $m(J/\psi\,\Lambda^0)$ distribution with a double-tailed asymmetric

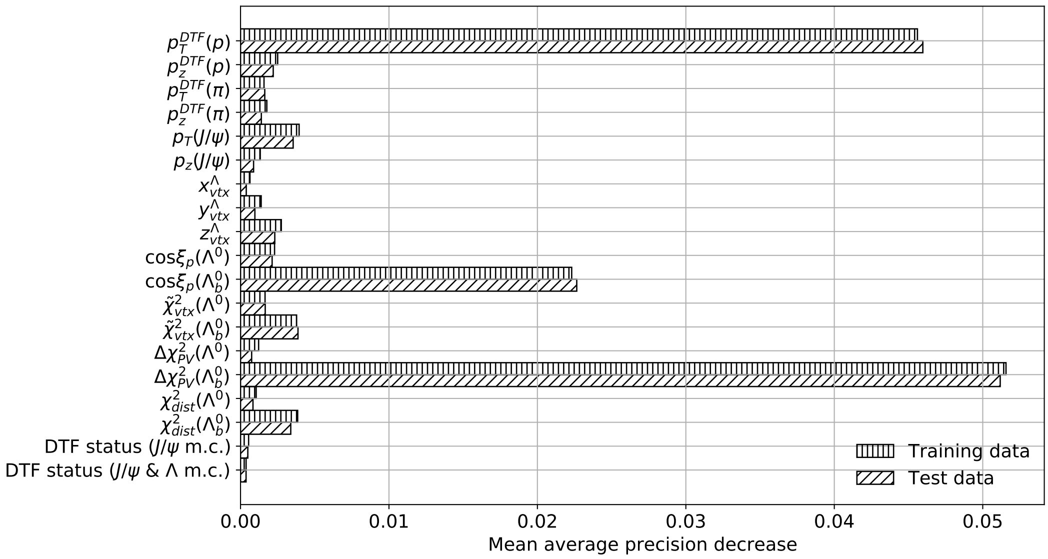

Figure 4.13: Decrease in the HBDT AP score when permutating the values of individual features in training (*vertical hatching*) and testing (*diagonal hatching*) data samples. See Section 4.1 for details on the feature labels.

Crystal Ball function. The standard, single-tailed Crystal Ball probability density function is parameterized as

$$f_{\mathrm{CB}}(m;\mu,\sigma,\alpha,n) = \begin{cases} \exp\left[-\frac{1}{2}\left(\frac{m-\mu}{\sigma}\right)^2\right], & \text{if } \frac{m-\mu}{\sigma} \geq -\alpha \\ A\cdot\left(B-\frac{m-\mu}{\sigma}\right)^{-n}, & \text{if } \frac{m-\mu}{\sigma} < -\alpha \end{cases}, \tag{4.17}$$

with

$$A = \left(\frac{n}{|\alpha|}\right)^n e^{-\frac{\alpha^2}{2}} \tag{4.18}$$

and

$$B = \frac{n}{|\alpha|} - |\alpha|. \tag{4.19}$$

Its shape is thus a Gaussian core with a power-law tail on the lower end when m outdistances μ by $\alpha\sigma$. The double-tailed Crystal Ball expands on this concept by having a Gaussian core with two asymmetric long tails, governed by different power laws:

$$f_{\mathrm{sig}}\left(m;S,\mu,\sigma,\alpha_1,n_1,\alpha_2,n_2\right) = N\begin{cases} f_{\mathrm{CB}}(m;\mu,\sigma,\alpha_1,n_1) & \text{if } m \leq \mu \\ f_{\mathrm{CB}}(2\mu-m;\mu,\sigma,\alpha_2,n_2) & \text{if } m > \mu \end{cases}, \tag{4.20}$$

with normalization

$$N = \frac{S}{\sigma(C_1 + C_2 + D)} \tag{4.21}$$

itself depending on

$$C_1 = \frac{n_1}{\alpha_1(n_1 - 1)} e^{-\frac{\alpha_1^2}{2}}, \tag{4.22}$$

$$C_2 = \frac{n_2}{\alpha_2(n_2 - 1)} e^{-\frac{\alpha_2^2}{2}}, \tag{4.23}$$

and

$$D = \sqrt{2\pi} \left(G_c(\alpha_2) - G_c(-\alpha_1) \right), \tag{4.24}$$

where

$$G_c(x) \coloneqq \frac{1}{\sqrt{2\pi}} \int_{-\infty}^{x} dt \, e^{-\frac{t^2}{2}} \tag{4.25}$$

is the Gaussian cumulative distribution function evaluated at x.

When fitting $m(J/\psi\,\Lambda^0)$ in Run 2 data, the function is the sum of two contributions: signal is modeled with the same double-tailed Crystal Ball from (4.17), with all parameters barring S and σ fixed to their Monte Carlo fit best values; the combinatorial background is fit with a conventional exponential function

$$f_{\text{bkg}}(m; C, a) = Ce^{-am}. \tag{4.26}$$

As will be shown in Section 4.4, the outlined combination of f_{sig} and f_{bkg} provides an excellent description of Run 2 data, as long as sufficient filtering is applied for the Λ_b^0 peak to emerge.

This data fit provides preliminary S_0 and B_0 values, obtained by integrating signal and background fit functions in the $\pm 3\sigma$ region around μ. I used these values to estimate the signal (background) rate S_i (B_i) for events passing a score threshold t_i with associated efficiency ε_i^S (ε_i^B):

$$S_i = S_0 \frac{\varepsilon_i^S}{\varepsilon_0^S}, \tag{4.27a}$$

$$B_i = B_0 \frac{\varepsilon_i^B}{\varepsilon_0^B}. \tag{4.27b}$$

Here ε_0^S and ε_0^B are the signal and background efficiencies associated to the soft threshold with S_0 and B_0 rates. Efficiencies were computed on the test sample and correspond to true/false positive rates evaluated for the ROC curve (Figure 4.12a).

Using the estimated S_i and B_i, I calculated the predicted signal significance (4.3) for each threshold t_i. Figure 4.14 shows the results as a function of the

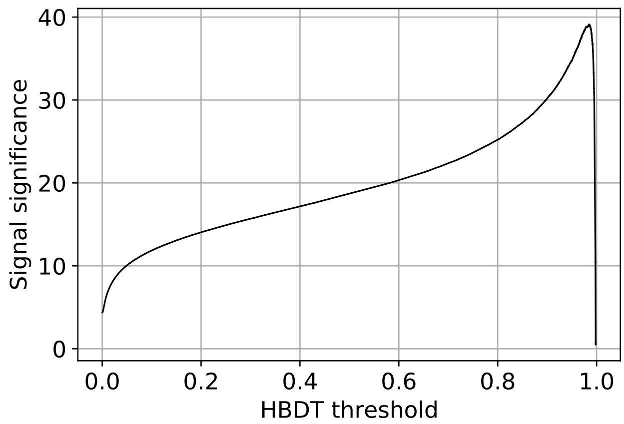

Figure 4.14: Projected $\Lambda_b^0 \to J/\psi\,\Lambda^0$ signal significance over background as a function of the HBDT response threshold used for selection.

score threshold. The best performing threshold was found to be $t_{\text{thres}} = 0.985$, with signal significance ≈ 46 and signal purity

$$\frac{S}{S+B} \approx 0.6. \tag{4.28}$$

4.4 Signal yield in invariant mass fits

Figure 4.15 shows the efficiencies of the presented selection steps as a function of the true z_{vtx}^{Λ}. The total efficiency of the process hovers in the 20–40% range, favouring selection of decays closer to the T stations. The main contribution lowering the efficiency is the $\approx 60\%$ of the HBDT threshold cut; while there is probably room for improvement in this field, a significant loss of signal is inevitable given the overwhelming combinatorial background the classifier is tasked to filter out.

Figures 4.16a and 4.16b show the $m(J/\psi\,\Lambda^0)$ invariant mass distributions of Monte Carlo simulated signal and Run 2 data after applying prefilters, $B^0 \to J/\psi\,K_S^0$ vetoes and the optimized $t > 0.985$ selection on the HBDT classifier score. To fit the distributions I adopted the same approach outlined in Section 4.3.4: the simulated signal is described with the double-tailed asymmetric Crystal Ball (4.17); the best fit parameter values, except for S and σ, are fixed for the signal function in the Run 2 data fit, while the exponential (4.26) was used to model the combinatorial background.

Binned fit results are listed in Table 4.1. The employed functions provide a great description for both the Monte Carlo simulation and the real data from Run 2, as seen from the fit-data discrepancies consistently below 3σ for

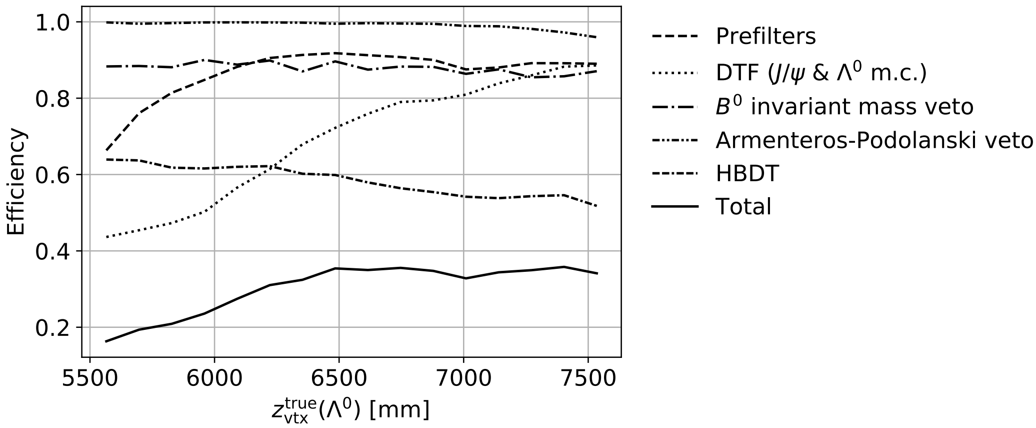

Figure 4.15: Efficiencies of the different steps of the $\Lambda_b^0 \to J/\psi\,\Lambda^0$ signal selection process, computed on reconstructed simulated events, as a function of the z component of the true $\Lambda^0 \to p\pi^-$ decay vertex. The steps are presented sequentially (top to bottom) in the legend; the efficiency of each step is computed on the baseline of events passing all previous steps.

each data bin. The resolution of the resonance peak is $\approx 12\%$ worse in real data compared to the simulation, an expected consequence of the underlying combinatorial background. Integrating the functions in the $\mu \pm 3\sigma$ interval, we estimate a 3590 ± 60 signal event yield and 2420 ± 50 background event yield. These are going to be the baseline yields for analyses on the Λ^0 electromagnetic dipole moments.

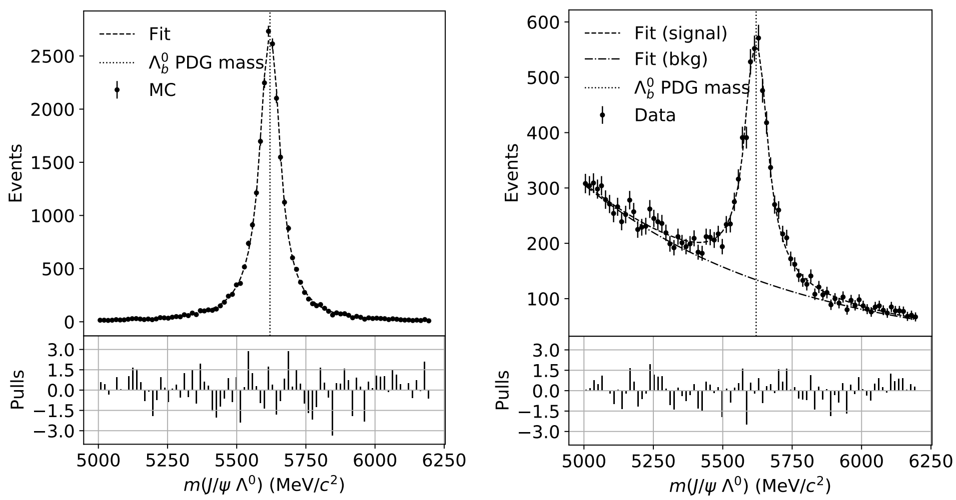

(a) **(b)**

Figure 4.16: Fitted $m(J/\psi\,\Lambda^0)$ invariant mass distributions for simulated $\Lambda_b^0 \to J/\psi\,\Lambda^0$ events *(a)* and Run 2 data *(b)* after all selection steps. Signal fit function is *dashed*, background fit function in *(b)* is *dash-dotted*. The PDG value for the Λ_b^0 mass [3] is marked by the *dotted vertical line*. Fit pulls (data-fit discrepancy divided by uncertainty) are shown below the main plots.

Parameter	Unit	Simulation		Data	
		Best value	Error	Best value	Error
S	–	365 900	3 100	65 600	1 800
μ	MeV/c^2	5 620.2	0.6	5 620.2	–
σ	MeV/c^2	36.9	1.0	41.6	1.6
α_1	–	0.99	0.04	0.99	–
n_1	–	2.44	0.12	2.44	–
α_2	–	1.01	0.04	1.01	–
n_2	–	2.69	0.15	2.69	–
C	–	–	–	240,000	40 000
a	$\times 10^{-3}$ MeV$^{-1}c^2$	–	–	1.336	0.029

Table 4.1: Parameter best values and associated uncertainties from $m(J/\psi\,\Lambda^0)$ fits on simulated signal and Run 2 data, after all selection steps. Parameters with no reported error are fixed.

Chapter 5

Preliminary study on the $\Lambda^0 \to p\pi^-$ angular distribution

In this final chapter, I present the results of a preliminary look into the angular distribution of $\Lambda^0 \to p\pi^-$ decay products, one of the key components for the measurement of Λ^0 electromagnetic dipole moments. Section 5.1 outlines the technique used to compute θ_p and ϕ_p angles in the Λ^0 helicity frame, as well as showcasing the main features of the angular distributions in the reconstructed $\Lambda_b^0 \to J/\psi\,\Lambda^0$ simulated sample. Section 5.2 focuses on the resolution on the two proton angles and explores the achievable improvements in view of the prospective resolution of the ghost vertex problem.

Unless otherwise specified, results and plots in this chapter are obtained with simulated $\Lambda_b^0 \to J/\psi\,\Lambda^0$ events with all selection steps from Chapter 4 applied (prefilters, B^0 invariant mass veto, K_S^0 Armenteros-Podolanski veto and HBDT $t > 0.985$ cut) and selecting the $\mu \pm 3\sigma$ signal region, using best values $\mu = 5620.2\,\mathrm{MeV/c^2}$ and $\sigma = 41.6\,\mathrm{MeV/c^2}$ from the Run 2 data $J/\psi\,\Lambda^0$ invariant mass fit.

5.1 Proton angular distribution

As described in Section 1.4, Λ^0 polarization $\vec{s}$ after the magnet can be computed by fitting the proton angular distribution

$$\frac{dN}{d\Omega'} = 1 + \alpha \vec{s} \cdot \hat{k}', \tag{1.50 revisited}$$

with unit vector

$$\hat{k}' = \begin{pmatrix} \sin\theta' \cos\phi' \\ \sin\theta' \sin\phi' \\ \cos\theta' \end{pmatrix}, \tag{1.51 revisited}$$

pointing in the flight direction $\Omega' \coloneqq (\theta', \phi')$ of the proton in the Λ^0 rest frame. I compute the helicity angle in the S_Λ frame, whereby the z axis is defined by the Λ^0 momentum direction $\hat{p}_\Lambda^H$ in the Λ_b^0 rest frame S_H (depicted in Figure 1.4b). This is the frame where initial Λ^0 polarization is maximal, thus preventing the Wick dilution effect that arises when using the $S_{\Lambda L}$ frame (see Section 1.4.3).

We define the heavy hadron Λ_b^0 rest frame coordinate system (x_0^H, y_0^H, z_0^H), with

$$\hat{z}_0^H = \hat{p}_{\Lambda_b}^{\mathrm{L}} \tag{5.1}$$

pointing towards the Λ_b^0 momentum in the laboratory frame, x_0^H parallel to the normal to the Λ_b^0 production plane and $\hat{y}_0^H = \hat{z}_0^H \times \hat{x}_0^H$. The S_Λ rest frame can be reached from the Λ_b^0 rest frame via the rotation operator $R(\phi, \theta, 0)$, with θ and ϕ being the Λ^0 helicity angles shown in Figure 1.4b: a rotation of angle ϕ about the z_0^H axis sends $(x_0^H, y_0^H, z_0^H) \to (x_1^H, y_1^H, z_1^H)$ and a θ rotation about y_1^H sends $(x_1^H, y_1^H, z_1^H) \to (x_2^H, y_2^H, z_2^H)$. The final rotation about z_2^H is not necessary and conventionally set to zero [34] [88]. This twice-rotated frame defines the S_Λ helicity frame coordinate system used to compute θ', ϕ' for (1.50):

$$\begin{cases} \hat{x}_0^\Lambda = \hat{x}_2^H, \\ \hat{y}_0^\Lambda = \hat{y}_2^H, \\ \hat{z}_0^\Lambda = \hat{z}_2^H. \end{cases} \tag{5.2}$$

In practice, the z_0^Λ direction is the easiest to compute, as by definition of S_Λ it's the Λ_b^0 momentum unit vector in the S_H frame:

$$\hat{z}_0^\Lambda = \hat{z}_2^H = \hat{p}_\Lambda^H. \tag{5.3}$$

Axis $\hat{x}_0^\Lambda = \hat{x}_2^H$ is defined as the antiparallel unit vector to the component of $\hat{z}_1^H$ that is perpendicular to $\hat{z}_2^H = \vec{p}_\Lambda^H$. An extensive treatment of the first rotation is superfluous for our end goal: since said rotation is about $\hat{z}_0^H$, obviously $\hat{z}_1^H = \hat{z}_0^H$ and we can determine $\hat{x}_0^\Lambda$ by computing the $\hat{z}_0^H$ component perpendicular to $\vec{p}_\Lambda^H$. This is done by vector-subtracting its projection on $\vec{p}_\Lambda^H$ from $\hat{z}_0^H$ itself:

$$\vec{a}_{\hat{z}_0 \perp \Lambda}^H \coloneqq \left(\hat{z}_0^H\right)_{\perp \vec{p}_\Lambda^H} = \hat{z}_0^H - \left(\hat{z}_0^H\right)_{\parallel \vec{p}_\Lambda^H}, \tag{5.4}$$

$$\hat{x}_0^\Lambda = \hat{x}_2^H = -\hat{a}_{\hat{z}_0 \perp \Lambda}^H. \tag{5.5}$$

The y_0^Λ axis is fixed by the Cartesian coordinate convention:

$$\hat{y}_0^\Lambda = \hat{z}_0^\Lambda \times \hat{x}_0^\Lambda \tag{5.6}$$

Within this newfound coordinate system we can compute the proton θ_p and ϕ_p helicity angles

$$\cos\theta_p \coloneqq \cos\theta' = \hat{z}_0^\Lambda \cdot \hat{p}_p^\Lambda, \tag{5.7a}$$

$$\phi_p \coloneqq \phi' = \operatorname{arctan2}\left(\hat{y}_0^\Lambda \cdot \hat{p}_p^\Lambda, \hat{x}_0^\Lambda \cdot \hat{p}_p^\Lambda\right), \tag{5.7b}$$

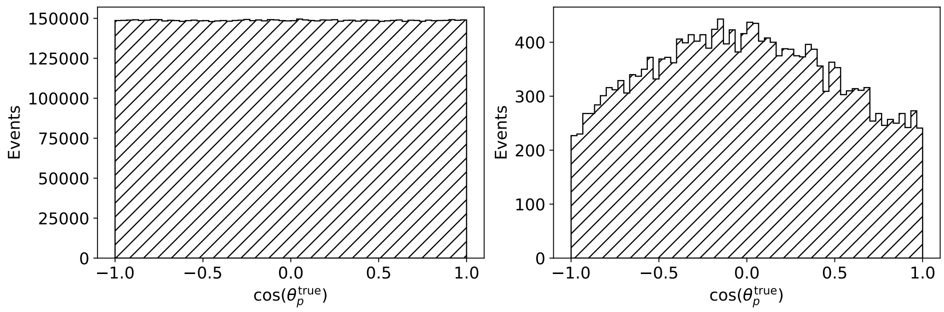

(a) **(b)**

Figure 5.1: Distributions of true values of $\cos\theta_p$, as defined in (5.7a), for simulated $\Lambda_b^0 \to J/\psi\,\Lambda^0$ events after all selection steps: *(a)* using all generated events; *(b)* using only reconstructed events.

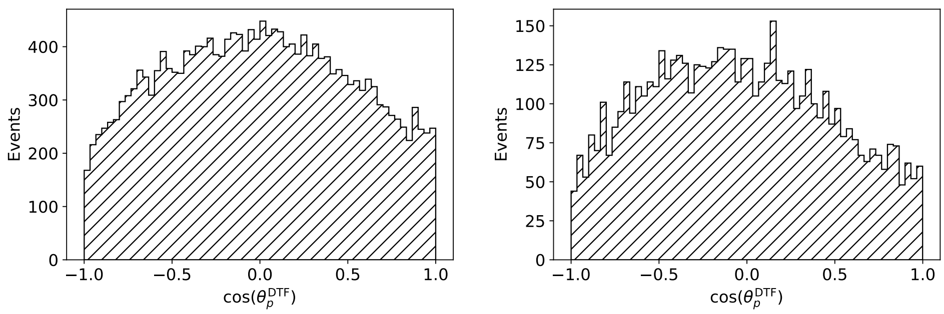

(a) **(b)**

Figure 5.2: Distributions of reconstructed $\cos\theta_p$, as defined in (5.7a), for simulated $\Lambda_b^0 \to J/\psi\,\Lambda^0$ events *(a)* and Run 2 data *(b)* after all selection steps. Angle θ_p is computed using Decay Tree Fitter momenta with J/ψ and Λ^0 mass constraints.

with momenta computed in the Λ^0 rest frame via a double Lorentz boost (laboratory frame into Λ_b^0 rest frame into Λ^0 rest frame).

Figure 5.1a depicts the $\cos\theta_p$ distribution of all (including non-reconstructed) simulated $\Lambda_b^0 \to J/\psi\,\Lambda^0$ events using true p and π^- momenta; these events are generated without accounting for Λ^0 polarization, hence the expected flatness of the distribution. Figure 5.1b shows true $\cos\theta_p$ distribution as well, this time only considering reconstructed events passing all selection steps. The comparison between these two figures highlights the angular acceptance effects that factor in the prospective Λ^0 EDM/MDM measurement.

Affinity of Figure 5.1b with Figure 5.2a, which shows reconstructed $\cos\theta_p$ using DTF momenta with J/ψ and Λ^0 mass constraints, foreshadows the great angular resolution I will delve into in Section 5.2. Finally, $\cos\theta_p$ in Run 2 data after all selection steps is shown in Figure 5.2b: this distribution is the

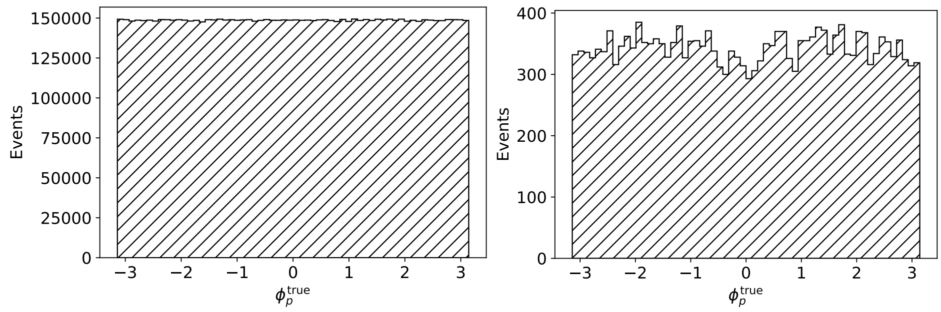

(a) **(b)**

Figure 5.3: Distributions of true values of ϕ_p, as defined in (5.7b), for simulated $\Lambda_b^0 \to J/\psi\,\Lambda^0$ events after all selection steps: *(a)* using all generated events; *(b)* using only reconstructed events.

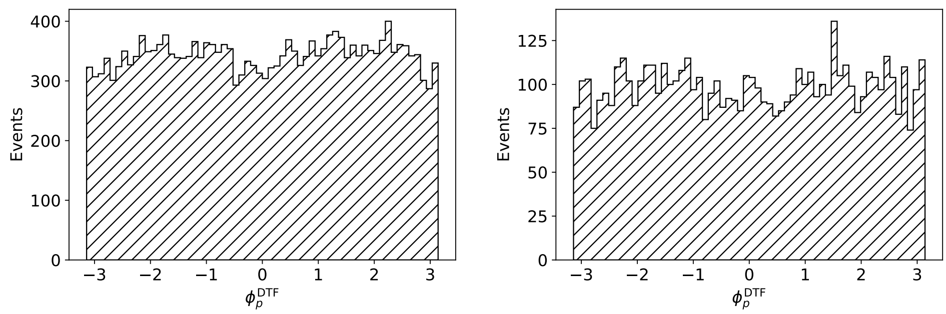

(a) **(b)**

Figure 5.4: Distributions of reconstructed ϕ_p, as defined in (5.7b), for simulated $\Lambda_b^0 \to J/\psi\,\Lambda^0$ events *(a)* and Run 2 data *(b)* after all selection steps. Angle ϕ_p is computed using Decay Tree Fitter momenta with J/ψ and Λ^0 mass constraints.

overlap of contributions from $\Lambda_b^0 \to J/\psi\,\Lambda^0$ signal with polarized Λ^0 and from combinatorial background in the $\mu \pm 3\sigma$ signal region.

The same considerations made for $\cos\theta_p$ are valid for ϕ_p distributions, which are reported in Figures 5.3 and 5.4.

5.2 Proton angular resolution

To assess the resolution on the proton angular distribution in reconstructed $\Lambda_b^0 \to J/\psi\,\Lambda^0$ events, I defined 8 bins in $\cos\theta_p^{\text{true}}$ and 12 bins in ϕ_p^{true} and evaluated reconstructed angle dispersion in each truth bin. Angular resolution within a bin is defined as the root mean square error (RMSE) between

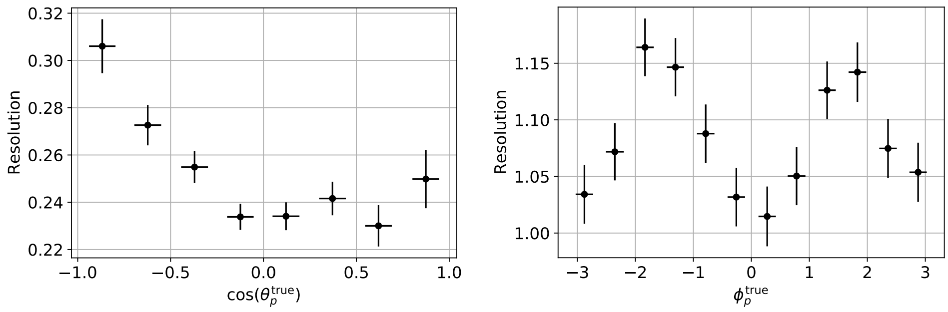

(a) **(b)**

Figure 5.5: Resolutions on $\cos\theta_p$ *(a)* and ϕ_p *(b)* as a function of the respective true values, computed on simulated $\Lambda_b^0 \to J/\psi\,\Lambda^0$ events after all selection steps. Standard deviations within each bin are used as error bars on the x axes.

reconstructed and true angles:

$$\mathrm{RMSE}(\psi) = \sqrt{\frac{1}{N}\sum_{i=1}^{N}\left(\psi_i^{\mathrm{DTF}} - \psi_i^{\mathrm{true}}\right)^2}, \tag{5.8}$$

with $\psi = \{\cos\theta_p, \phi_p\}$.

Figure 5.5a shows $\cos\theta_p$ resolution as a function of $\cos\theta_p^{\mathrm{true}}$, demonstrating overall good resolution (in line with $\cos\theta_p$ variability within each bin). The asymmetry in resolution at the opposite ends of the $\cos\theta_p$ spectrum, with a marked degradation of resolution around $\cos\theta_p^{\mathrm{true}} \approx -1$, does not have a clear explanation; however, as will be seen in Section 5.2.1, this behaviour becomes noticeably less pronounced when the high-bias ghost vertex class of events is removed from the sample.

Figure 5.5b depicts the same plot for azimuthal helicity angle ϕ_p. The only change from the $\cos\theta_p$ computation is that ϕ_p resolution needs to account for the fact that $\phi = -\pi$ and $\phi = \pi$ are physically the same angle. This has non-intuitive ripercussions when computing the residuals between ϕ_p^{true} and ϕ_p^{reco}. For instance, the nominal difference between $\phi_p^{\mathrm{reco}} = \pi - \varepsilon$ and $\phi_p^{\mathrm{true}} = -\pi + \varepsilon$ is $2\pi - 2\varepsilon$, but from a physical point of view the reconstructed angle is only off by 2ε:

$$|\phi_p^{\mathrm{reco}} - \phi_p^{\mathrm{true}}| = |\,(\pi - \varepsilon) - (-\pi + \varepsilon)\,| = |\,\underbrace{\pi - (-\pi)}_{\substack{=0\\ \text{same angles}}} - 2\varepsilon| = 2\varepsilon \tag{5.9}$$

Given $\phi_1, \phi_2 \in [-\pi, \pi]$, this problem is easily solved by computing

$$d \coloneqq |\phi_1 - \phi_2| \bmod 2\pi \tag{5.10}$$

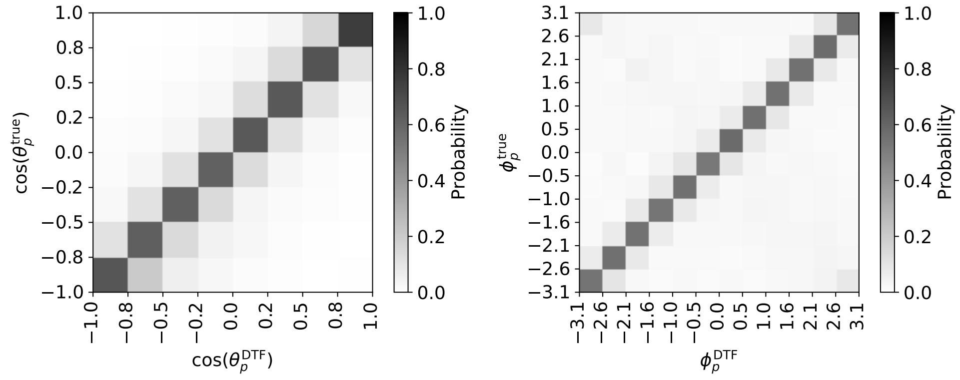

(a) **(b)**

Figure 5.6: Migration matrices of $\cos\theta_p$ *(a)* and ϕ_p *(b)*, computed on simulated $\Lambda_b^0 \to J/\psi\,\Lambda^0$ events after all selection steps. Probabilities and chromatic scale are normalized on true bins.

and choosing as distance the lesser value between d and $2\pi - d$.

The range of variability for ϕ_p resolution is even smaller compared to $\cos\theta_p$, which is consistent with the expected azimuthal symmetry of the LHCb detector; nevertheless, resolution gets noticeably worse for $\phi_p \approx \pm\frac{\pi}{2}$. The shape of Figure 5.5b shows remarkable correlation with the observed angular ϕ_p acceptance in reconstructed events (see Figure 5.4a), suggesting that the two effects might share a common source; moreso than in the $\cos\theta_p$ case, this effect is all but removed when excluding ghost vertex events.

The general soundness of proton angular reconstruction translates in the $\cos\theta_p$ and ϕ_p migration matrices presented in Figure 5.6: each (i, j) bin is color-coded according to the probability $P(i \to j)$ of migration from ψ_i in true bin i to ψ_j in reconstructed bin j. Probabilities are normalized to unity in the true bin, that is

$$\sum_{j\in\{\text{reco bins}\}} P(i \to j) = 1. \tag{5.11}$$

The matrices are both diagonal net of dispersion effects, demonstrating the lack of meaningful bias in reconstruction of $\cos\theta_p$ and ϕ_p. In Figure 5.6b, the top left and bottom right bins are evidence of the looping effect of the $[-\pi, \pi]$ range of values for ϕ_p, both harboring events from the physically adjacent bottom left and top right bins.

5.2.1 Impact of ghost vertex events

As discussed in Section 3.5, resolution in the $z_{\mathrm{vtx}}^{\Lambda}$ component of the $\Lambda^0 \to p\pi^-$ decay vertex is affected by a significant $\approx 14\,\mathrm{cm}$ positive bias, whose

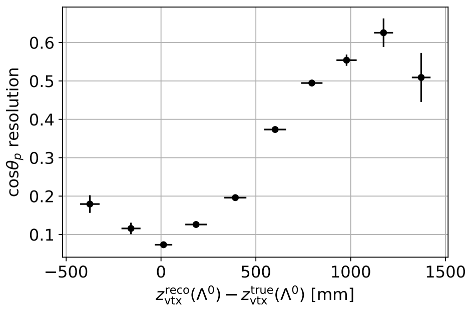

(a)

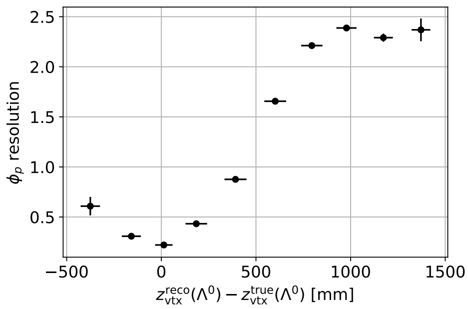

(b)

Figure 5.7: Angular resolutions on $\cos\theta_p$ *(a)* and ϕ_p *(b)* as a function of bias on reconstructed $z_{\mathrm{vtx}}^{\Lambda}$, computed on simulated $\Lambda_b^0 \to J/\psi\,\Lambda^0$ events after all selection steps.

distribution is depicted in Figure 3.13a. The detrimental effect of this bias is seen in Figure 5.7, showing proton $\cos\theta_p$ and ϕ_p resolutions as a function of $z_{\mathrm{vtx}}^{\Lambda}$ bias: resolutions worsen by a factor of five or more when going from $z_{\mathrm{vtx}}^{\mathrm{reco}} - z_{\mathrm{vtx}}^{\mathrm{true}} \approx 0\,\mathrm{m}$ to $1.2\,\mathrm{m}$. This is to be expected since poor Λ^0 vertex reconstruction affects resolution on proton momenta.

Studies detailed in Section 3.5.1 illustrate that most highly biased events can be traced back to the «ghost vertex» problem, whereby the bending of $p\pi^-$ tracks in the xz plane due to the LHCb magnetic field creates a second crossing point which provides a local χ^2 minimum for the Vertex Fitter algorithm to converge at. This issue affects almost one third of $\Lambda_b^0 \to J/\psi\,\Lambda^0$ simulated events and is only found in T tracks, since other track types come from particles produced upstream of the magnet.

Work is currently underway in the Milan and Valencia LHCb research groups to solve or mitigate the ghost vertex issue, with the goal of standardizing Λ^0 vertex resolution to the non-ghost-vertex baseline of $\approx 5.2\,\mathrm{cm}$. Should such an endeavour be successful, Figure 5.7 proves it would have a significant effect on the proton angular resolution and thus on the prospective measurement of Λ^0 electromagnetic dipole moments. As a proof of concept study, I computed angular resolutions for $\cos\theta_p$ and ϕ_p excluding ghost vertex events, the latter being defined with the locus of points from (3.38). Results are shown in Figures 5.8 and 5.9: in both cases resolution improves by a factor 2–3 in all truth bins. Furthermore, the deviation from flat resolutions seen in Figure 5.5a and 5.5b are significantly suppressed when removing ghost vertex events, identifying them as the primary culprits.

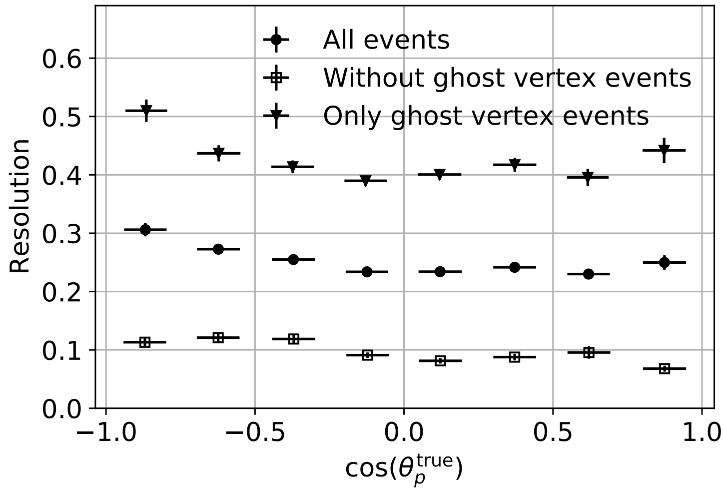

Figure 5.8: Angular resolution on $\cos\theta_p$ as a function of its true values. Resolution is computed on simulated $\Lambda_b^0 \to J/\psi\,\Lambda^0$ events after all selection steps, including (*filled circles*), removing (*empty squares*), and only keeping (*filled triangles*) $\Lambda^0 \to p\pi^-$ ghost vertex events.

5.3 Resolution effects on expected proton angular distributions

As seen in the previous section, resolution on proton production angles θ_p and ϕ_p can be significantly improved with the removal of ghost vertex events. As a first test of the impact of this enhancement on the prospective measurement of Λ^0 electromagnetic dipole moments, I generated samples of $n = 10^6$ $\Lambda_b^0 \to J/\psi\,\Lambda^0$ events under the following simplifying assumptions:

- Λ^0 are produced with $\vec{p} = p\hat{z}$, $\beta = 1$ and maximal longitudinal polarization $\vec{s}_0 = (0, 0, 1)$;
- all Λ^0 traverse the full $D_y = 4\,\mathrm{T\,m}$ LHCb magnetic field before decaying;
- no experimental resolutions are considered outside of the ones on $\cos\theta_p$ and ϕ_p;
- all acceptance effects are neglected;
- the Λ^0 gyroelectric and gyromagnetic factors are fixed to $d = 0$ and $g = 1.226$ [89] respectively.

For each event, values of $\cos\theta_p$ and ϕ_p were generated following the probability distribution

$$f(\cos\theta_p, \phi_p) \coloneqq 1 + \alpha\vec{s}\cdot\hat{k}, \tag{5.12}$$

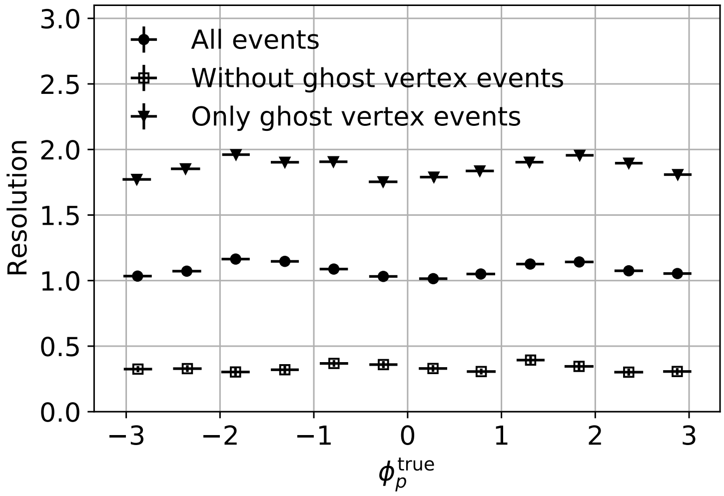

Figure 5.9: Angular resolution on ϕ_p *(a)* as a function of true values. Resolution is computed on simulated $\Lambda_b^0 \to J/\psi\,\Lambda^0$ events after all selection steps, including (*filled circles*), removing (*empty squares*), and only keeping (*filled triangles*) $\Lambda^0 \to p\pi^-$ ghost vertex events.

with precessed polarization vector

$$\vec{s} = \begin{cases} s_x = \sin\Phi \\ s_y = 0 \\ s_z = \cos\Phi \end{cases} , \tag{5.13}$$

proton production direction in the S_Λ frame

$$\hat{k} = \begin{pmatrix} \sqrt{1-\cos^2\theta_p}\cos\phi_p \\ \sqrt{1-\cos^2\theta_p}\sin\phi_p \\ \cos\theta_p \end{pmatrix} , \tag{5.14}$$

and precession angle vector

$$\Phi = \frac{gD_y\mu_B}{\hbar c}. \tag{5.15}$$

To extract angles according to (5.12), I employed a standard Monte Carlo rejection sampling algorithm: $\cos\theta_p \in [-1,1]$, $\phi_p \in [-\pi,\pi]$ and $\varepsilon \in [0,2]$ are generated uniformly in the respective intervals with a Mersenne Twister pseudorandom number engine; the chosen $\cos\theta_p$ and ϕ_p are accepted if $\varepsilon < f(\cos\theta_p, \phi_p)$, otherwise the process is repeated with a new set of values. The effect of angular resolutions on the measurement of $\cos\theta_p$ and ϕ_p was implemented with a per-event Gaussian smearing: the generated angles are used as mean value μ of

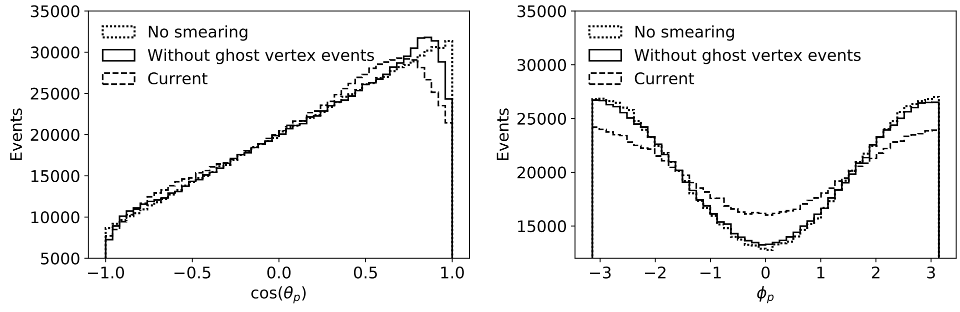

(a) **(b)**

Figure 5.10: Simplified distributions of $\cos\theta_p$ *(a)* and ϕ_p *(b)* assuming perfect angular resolution (*dotted line*), resolution with all reconstructed $\Lambda_b^0 \to J/\psi\,\Lambda^0$ events (*dashed line*) and resolution after the removal of ghost vertex events (*solid line*).

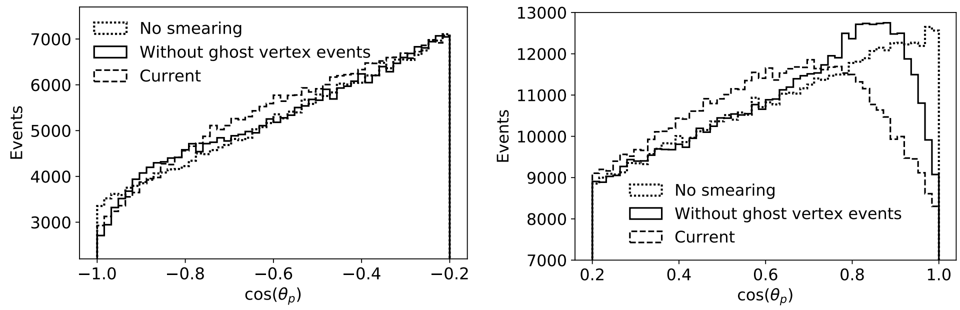

(a) **(b)**

Figure 5.11: Details on the leftmost *(a)* and rightmost *(b)* regions of $\cos\theta_p$ distributions from Figure 5.10a.

a Gaussian distribution $\mathcal{N}(\mu, \sigma^2)$, with σ being the average desired resolution, and new $\cos\theta_p$ and ϕ_p are chosen according to $\mathcal{N}$ with the aforementioned rejection sampling approach.

I produced three data samples: a «perfect» sample without any smearing, a sample matching the current resolution (i.e. with all reconstructed $\Lambda_b^0 \to J/\psi\,\Lambda^0$ events), and a sample matching resolution after the removal of ghost vertex events. Figure 5.10 shows the distributions of generated $\cos\theta_p$ and ϕ_p with the different angular resolutions. Effects on $\cos\theta_p$ are comparatively softer, primarily consisting in a depletion of $\cos\theta_p \approx \pm 1$ regions (shown in greater detail in Figure 5.11). In contrast, azimuthal angle ϕ_p distributions (Figure 5.10b) highlight the significant difference between the current resolution and the one attainable if the ghost vertex issue were to be completely solved: in the latter case the shape is much flatter, whereas the former sports a

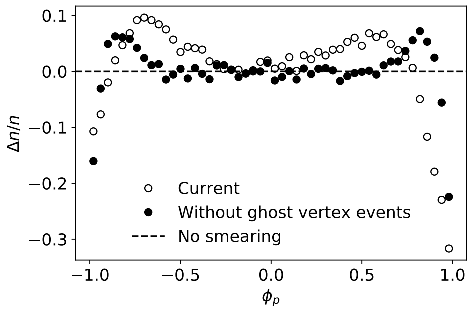

(a)

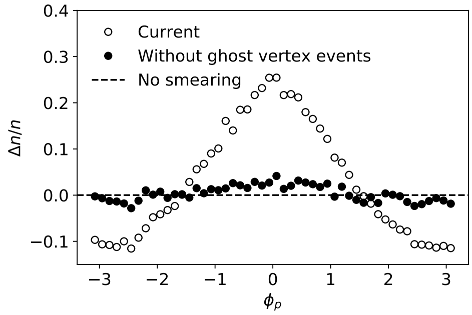

(b)

Figure 5.12: Binwise difference (in percentage of events) between smeared and non-smeared distributions of $\cos\theta_p$ *(a)* and ϕ_p *(b)* from Figure 5.10: *empty circles* are computed with smearing matching resolution with all reconstructed $\Lambda_b^0 \to J/\psi\,\Lambda^0$ events, *filled circles* with smearing matching resolution after the removal of ghost vertex events.

distribution almost indistinguishable from the one without smearing. It bears mentioning that the effect of a worse resolution in the ϕ_p case is highly correlated with the value of g: in the extreme instance of $g = 0$ no spin precession takes place, resulting in a final polarization $s_x = 0$ and a flat distribution in ϕ_p. Since the Gaussian smearing also tends to flatten the ϕ_p distribution, a fit to the measured proton angular distribution will result in a systematic underestimation of g unless the fit function takes due account of the resolution, e.g. via convolution with a Gaussian distribution.

Figure 5.12 tackles the same resolution comparison with a more numerical approach, plotting the binwise percentage difference between smeared and non-smeared angular distributions. Variations for $\cos\theta_p$ are contained within $\pm 10\%$ across the board except for the highly depleted $\cos\theta_p \approx \pm 1$ edges, reaching a -30% dip in the rightmost bin when retaining ghost vertex events. The difference is again far more noticeable for ϕ_p: the current resolution causes a $+20\%$ increase in events around $\phi_p \approx 0$, compensated with -10% decreases in the $\phi_p \approx \pm\pi$ portions of the distribution; the resolution after ghost vertex events removal imprints much more moderate $\leq \pm 5\%$ deviations from the non-smeared distribution and preserves its overall shape.

Conclusions

Electric and magnetic dipole moments of particles are sensitive to physics within and beyond the Standard Model. In this thesis, I worked on various aspects of the $\Lambda_b^0 \to J/\psi\ (\to \mu^+\mu^-)\ \Lambda^0\ (\to p\pi^-)$ decay analysis in preparation of a first measurement of the Λ^0 electromagnetic dipole moments using the LHCb Run 2 dataset.

Only roughly 45% of candidate $\Lambda^0 \to p\pi^-$ events reach convergence in the vertex reconstruction process. I conducted topological studies on a sample of simulated events to show that this is a result of a conflict of information in xz (bending) and yz (non-bending) track propagation planes. Through further investigation of the measured kinematic variables and comparison with the Monte Carlo generated values, I exposed a systematic underestimation of p_z in pion tracks reconstructed from hits in the T1–T3 downstream tracking stations. Said bias is only observed in non-converging $\Lambda^0 \to p\pi^-$ events and is understood to play a role in the xz-yz discrepancy at the origin of the vertexing failure. Additional research is under way to locate and fix the source of p_z bias, starting with the track momentum fit process at T station level.

For the time being, I demonstrated that recovery of a significant percentage of failed events in possible by modifying the main vertex fitting algorithm to increase the weight of track propagation in a specific plane. A threefold refit approach, attributing more importance to yz, xz and xy planes sequentally, results in a +26.4% increase in signal statistics. Comparisons to Monte Carlo truth reveal that recovered events have suboptimal reconstruction, with a median bias on the z component of the $\Lambda^0 \to p\pi^-$ vertex 20 cm greater than standard reconstructed events. Studies confirm that this is due to poor track information available in these events; the impact of lower vertex resolution on the Λ^0 electromagnetic dipole moment measurement is currently under analysis.

Working on $\Lambda_b^0 \to J/\psi\, \Lambda^0$ signal selection, I finalized the three main steps of the process: loose preliminary selections for long-lived Λ^0 events, including requirement of Decay Tree Fitter convergence with J/ψ and Λ^0 mass constraints; rejection of $B^0 \to J/\psi\, K_S^0$ physical background with an invariant mass veto and a cut in the Armenteros-Podolanski α–p_T space; the final selection of signal with a histogram-based gradient boosting classification tree, trained with simulated signal and LHCb combinatorial background and optimized to maximize $\Lambda_b^0 \to J/\psi\,\Lambda^0$ signal significance. The $m(J/\psi\,\Lambda^0)$ invariant mass fit after all steps shows good agreement with data, estimating a signal (background) yield of 3590 ± 60 (2420 ± 50).

As first step of the future Λ^0 dipole moment measurement, I computed angular distribution (θ_p, ϕ_p) of proton momentum in the Λ^0 helicity frame, which probes the final polarization state of decaying Λ^0 required for the spin precession technique. Angular reconstruction is unbiased net of acceptance effects; resolutions of 0.2–0.3 (1.0–1.2) for $\cos\theta_p$ (ϕ_p) are reasonably low, amounting to roughly one sixth of the allowed angular ranges.

Simulated $\Lambda_b^0 \to J/\psi\,\Lambda^0$ events passing the full selection process retain a median 14 cm bias in the z component of the reconstructed $\Lambda^0 \to p\pi^-$ vertex, which has a detrimental effect on $\cos\theta_p$ and ϕ_p resolutions. This can mostly be attributed to proton and pion tracks being bent by the magnetic field into a second downstream crossing point, acting as local χ^2 minimum during the vertexing process and being erroneously selected as the Λ^0 decay vertex. Removing this class of events (31.6% of the simulated sample) improves proton angular resolutions by a factor 2–3 across the full range of values. Simplified pseudoexperiments confirm that the higher resolution also reduces potential correlation effects with the value of gyromagnetic factor g in the angular fit, particularly concerning the ϕ_p distribution. Changing the vertex fitting algorithm to account for multiple χ^2 minima would therefore significantly affect the dipole moment measurement and must be considered a high priority for the analysis.

None of the issues I have identified during my work on this analysis compromise the prospective first measurement of the Λ^0 electromagnetic dipole moments. On the contrary, the achieved signal yield and absence of bias in the observed angular distributions are a resounding confirmation that physics results with long-lived Λ^0 baryons are possible at LHCb with just Run 2 data. Given the upcoming statistics surge projected for Run 3 and the significant boost in yield and resolution an improved vertexing algorithm would provide, the outlook is promising for a competitive measurement of Λ^0 gyroelectric and gyromagnetic factors.

Appendix A

Prefilter selections for $\Lambda_b^0 \to J/\psi\ (\to \mu^+\mu^-)\ \Lambda^0\ (\to p\pi^-)$ decay

Table A.1 reports the applied prefilter criteria for the preliminary selection of $\Lambda_b^0 \to J/\psi\ (\to \mu^+\mu^-)\ \Lambda^0\ (\to p\pi^-)$ signal decays over background.

Variable	Unit	Minimum	Maximum
$p(p)$	MeV/c	2 000	500 000
$p_T(p)$	MeV/c	400	–
$p(\pi^-)$	MeV/c	10 000	500 000
z_Λ^{vtx}	mm	5 500	8 500
$p_T(\Lambda^0)$	MeV/c	450	–
$m(p\pi^-)$ (Vertex Fitter)	MeV/c^2	600	1 500
$m(p\pi^-)$ (combined)	MeV/c^2	–	2 000
$m(p\pi^-)$ (measured)	MeV/c^2	–	1 500
$\cos\xi_p(\Lambda^0)$	–	0.9999	–
$\Delta\chi^2_{\text{PV}}(\Lambda^0)$	–	–	200
$\chi^2_{\text{dist}}(\Lambda^0)$	–	–	2×10^7
$\chi^2_{\text{vtx}}(\Lambda^0)$	–	–	750
$\lvert m(\mu^+\mu^-) - m_{\text{PDG}}(J/\psi)\rvert$	MeV/c^2	–	90
$m(J/\psi\,\Lambda^0)$ (combined)	MeV/c^2	4 700	–
$m(J/\psi\,\Lambda^0)$ (Vertex Fitter)	MeV/c^2	–	8 500
$\lvert\cos\xi_p(\Lambda_b^0)\rvert$	–	0.99	–
$\Delta\chi^2_{\text{PV}}(\Lambda_b^0)$	–	–	1 750
$\chi^2_{\text{vtx}}(\Lambda_b^0)$	–	–	150

Table A.1: Prefilter selection criteria applied to simulated $\Lambda_b^0 \to J/\psi\,\Lambda^0$ signal and Run 2 data. The Vertex Fitter invariant mass is computed by the homonymous algorithm; the *combined* invariant mass is computed from the 4-momenta of the daughter particles at the first measurement position, without track extrapolation; the *measured* invariant mass is computed in the same way as the combined mass, but after extrapolation at the reconstructed decay vertex of the mother particle. Other variables are defined as in Section 4.1.

Appendix B

Discriminating features for multivariate classifier training

Figure B.1 shows the distribution of all kinematic variables chosen for histogram-based boosted decision tree training to select $\Lambda_b^0 \to J/\psi\ (\to \mu^+\mu^-)\ \Lambda^0\ (\to p\pi^-)$ events.

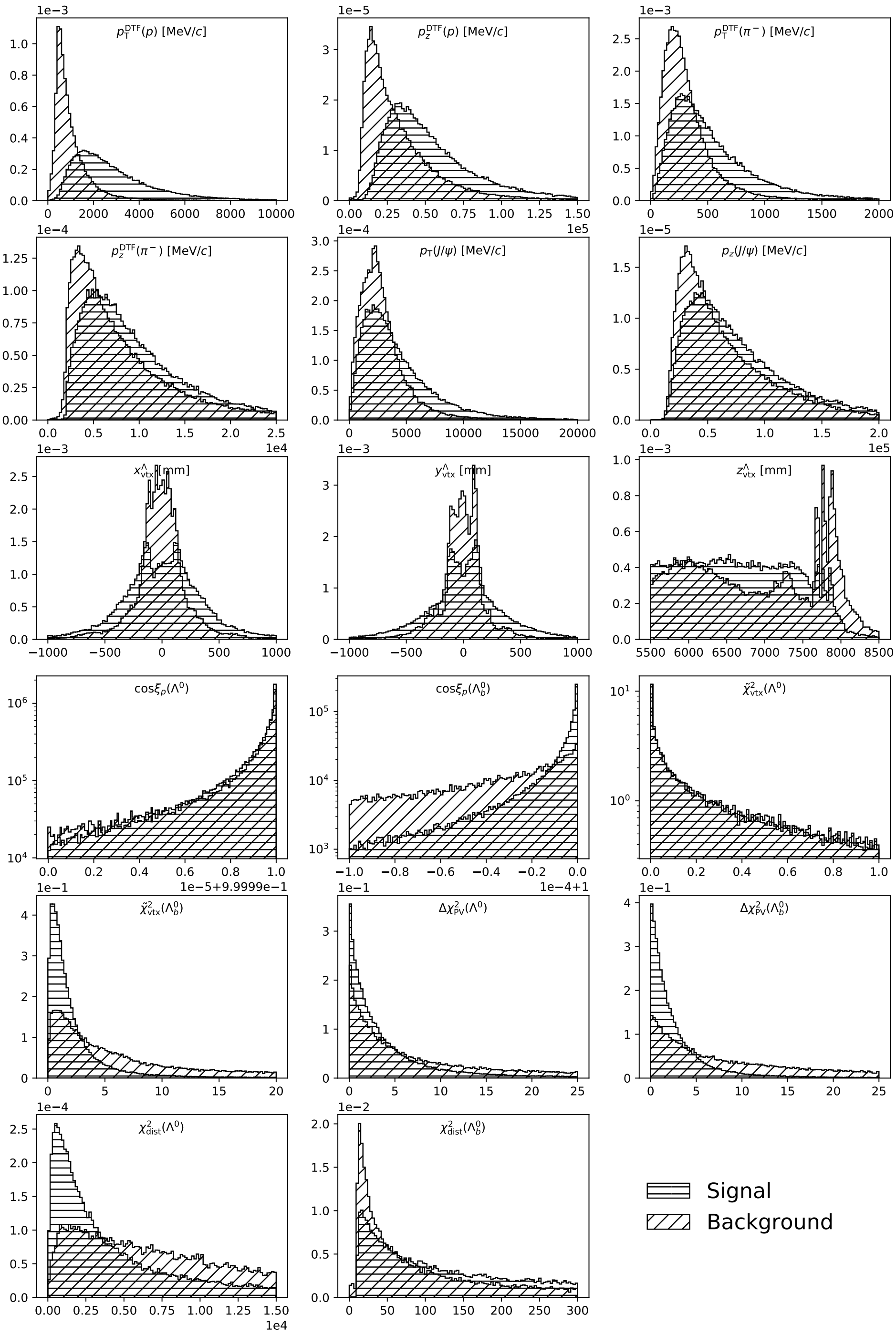

Figure B.1: Normalized distributions of kinematic variables in the HBDT training data for signal (*horizontal hatching*) and background from Run 2 data side bands (*diagonal hatching*). Definitions are as in Section 4.3.1; the y axes depict probability density.

Bibliography

[1] I. J. R. Aitchinson and A. J .G. Hey. *Gauge Theories in Particle Physics: A Practical Introduction. Volume 1: From Relativistic Quantum Mechanics to QED*. CRC Press, 2013.

[2] J. Erler and M. Schott. Electroweak precision tests of the Standard Model after the discovery of the Higgs boson. *Progress in Particle and Nuclear Physics*, 106:68–119, May 2019.

[3] P. A. Zyla et al. Review of Particle Physics. *PTEP*, 2020(8):083C01, 2020.

[4] A. B. McDonald. Sudbury Neutrino Observatory results. *Physica Scripta*, T121:29–32, Jan 2005.

[5] S.-K. Choi et al. (Belle Collaboration). Observation of a narrow charmonium-like state in exclusive $B^{\pm} \to K^{\pm}\pi^{+}\pi^{-}J/\psi$ decays. *Phys. Rev. Lett.*, 91(26), Dec 2003.

[6] T. Nakano et al. (LEPS Collaboration). Evidence for a narrow $S = +1$ baryon resonance in photoproduction from the neutron. *Phys. Rev. Lett.*, 91:012002, Jul 2003.

[7] P. W. Higgs. Broken symmetries and the masses of gauge bosons. *Phys. Rev. Lett.*, 13:508–509, Oct 1964.

[8] G. Aad et al. (ATLAS Collaboration). Observation of a new particle in the search for the Standard Model Higgs boson with the ATLAS detector at the LHC. *Physics Letters B*, 716(1):1–29, Sep 2012.

[9] S. Chatrchyan et al. (CMS Collaboration). Observation of a new boson at a mass of 125 GeV with the CMS experiment at the LHC. *Physics Letters B*, 716(1):30–61, Sep 2012.

[10] J. Zupan. Introduction to flavour physics. *arXiv e-prints*, Mar 2019.

[11] M. S. Sozzi. *Discrete symmetries and CP violation: from experiment to theory.* Oxford University Press, 2013.

[12] C. S. Wu, E. Ambler, R. W. Hayward, D. D. Hoppes, and R. P. Hudson. Experimental test of parity conservation in Beta decay. *Phys. Rev.*, 105:1413–1415, Feb 1957.

[13] R. L. Garwin, L. M. Lederman, and M. Weinrich. Observations of the failure of conservation of parity and charge conjugation in meson decays: the magnetic moment of the free muon. *Phys. Rev.*, 105:1415–1417, Feb 1957.

[14] J. P. Lees et al. (BABAR Collaboration). Observation of time-reversal violation in the B^0 meson system. *Phys. Rev. Lett.*, 109:211801, Nov 2012.

[15] I. B. Khriplovich and S. K. Lamoreaux. *CP Violation Without Strangeness. Electric Dipole Moments of Particles, Atoms, and Molecules.* Springer, 1997.

[16] J. H. Christenson, J. W. Cronin, V. L. Fitch, and R. Turlay. Evidence for the 2π decay of the K_2^0 meson. *Phys. Rev. Lett.*, 13:138–140, Jul 1964.

[17] A. Alavi-Harati et al. (KTeV Collaboration). Observation of direct CP violation in $K_{S,L} \to \pi\pi$ decays. *Phys. Rev. Lett.*, 83(1):22–27, Jul 1999.

[18] B. Aubert et al. (BaBar Collaboration). Measurement of CP-violating asymmetries in B^0 decays to CP eigenstates. *Phys. Rev. Lett.*, 86(12):2515–2522, Mar 2001.

[19] K. Abe et al. (Belle Collaboration). Observation of large CP violation in the neutral B meson system. *Phys. Rev. Lett.*, 87(9), Aug 2001.

[20] L. Canetti, M. Drewes, and M. Shaposhnikov. Matter and antimatter in the Universe. *New Journal of Physics*, 14(9):095012, Sep 2012.

[21] G. Steigman. Primordial nucleosynthesis in the precision cosmology era. *Annual Review of Nuclear and Particle Science*, 57(1):463–491, Nov 2007.

[22] L. Henry, D. Marangotto, A. Merli, N. Neri, J. Ruiz Vidal, and F. Martinez Vidal. Search for new physics via baryon EDM at LHC. *arXiv e-prints*, Jan 2021.

[23] M. E. Pospelov and I. B. Khriplovich. Electric dipole moment of the W boson and the electron in the Kobayashi-Maskawa model. *Sov. J. Nucl. Phys.*, 53:638–640, 1991.

[24] I. B. Khriplovich. Quark electric dipole moment and induced θ term in the Kobayashi-Maskawa model. *Phys. Lett. B*, 173:193–196, 1986.

[25] I. B. Khriplovich and A. R. Zhitnitsky. What is the value of the neutron electric dipole moment in the Kobayashi-Maskawa model? *Phys. Lett. B*, 109:490–492, 1982.

[26] F. J. Botella, L. M. Garcia Martin, D. Marangotto, F. Martinez Vidal, A. Merli, N. Neri, A. Oyanguren, and J. Ruiz Vidal. On the search for the electric dipole moment of strange and charm baryons at LHC. *The European Physical Journal C*, 77(3), Mar 2017.

[27] J. M. Pendlebury et al. Revised experimental upper limit on the electric dipole moment of the neutron. *Phys. Rev. D*, 92:092003, Nov 2015.

[28] E. Dahl-Jensen, N. Doble, D. Evans et al. A new measurement of the magnetic moment of the Λ-hyperon. *Nuov Cim A*, 3:1–24, May 1971.

[29] G. Baroni, S. Petrera, and G. Romano. An upper limit of the electric-dipole moment of the Λ-hyperon. *Lett. Nuovo Cimento*, 2:1256–1258, Dec 1971.

[30] L. Schachinger et al. Precise measurement of the Λ^0 magnetic moment. *Phys. Rev. Lett.*, 41:1348–1351, Nov 1978.

[31] L. Pondrom et al. New limit on the electric dipole moment of the Λ hyperon. *Phys. Rev. D*, 23:814–816, Feb 1981.

[32] B. Borasoy. Electric dipole moment of the neutron in chiral perturbation theory. *Phys. Rev. D*, 61:114017, May 2000.

[33] G. Aad et al. (ATLAS Collaboration). Measurement of the parity-violating asymmetry parameter α_b and the helicity amplitudes for the decay $\Lambda_b^0 \to J/\psi\Lambda^0$ with the ATLAS detector. *Phys. Rev. D*, 89:092009, May 2014.

[34] J. D. Richman. An experimenter's guide to the helicity formalism. Technical report, Calif. Inst. Technol., Pasadena, CA, Jun 1984.

[35] T. D. Lee and C. N. Yang. General partial wave analysis of the decay of a hyperon of spin ½. *Phys. Rev.*, 108:1645–1647, Dec 1957.

[36] E. Leader. *Spin in Particle Physics.* Cambridge University Press, 2001.

[37] D. P. Grosnick et al. (The FNAL-E581/704 Collaboration). The design and performance of the FNAL high-energy polarized-beam facility. *Nucl. Instrum. Meth. A*, 290(2):269–292, 1990.

[38] R. Aaij et al. (LHCb Collaboration). LHCb detector performance. *International Journal of Modern Physics A*, 30(07):1530022, Mar 2015.

[39] L. Evans. The Large Hadron Collider. *Annual Review of Nuclear and Particle Science*, 61(1):435–466, 2011.

[40] R. Antunes-Nobrega et al. (LHCb Collaboration). LHCb reoptimized detector design and performance: Technical Design Report. Technical report, Geneva, 2003.

[41] A. A. Alves et al. (LHCb Collaboration). The LHCb detector at the LHC. *JINST*, 3:S08005, 2008. Also published by CERN Geneva in 2010.

[42] R. Aaij et al. (LHCb Collaboration). A precise measurement of the B^0 meson oscillation frequency. *The European Physical Journal C*, 76(7), Jul 2016.

[43] R. Aaij et al. (LHCb Collaboration). Precision measurement of the B_S^0–$\bar{B}_S^0$ oscillation frequency with the decay $B_S^0 \to D_S^- \pi^+$. *New Journal of Physics*, 15, Apr 2013.

[44] R. Aaij et al. (LHCb Collaboration). Observation of CP violation in charm decays. *Phys. Rev. Lett.*, 122:211803, May 2019.

[45] R. Aaij et al. (LHCb Collaboration). Updated LHCb combination of the CKM angle γ. Technical report, CERN, Geneva, Oct 2020.

[46] R. Aaij et al. (LHCb Collaboration). Measurement of the $B_s^0 \to \mu^+\mu^-$ branching fraction and effective lifetime and search for $B^0 \to \mu^+\mu^-$ decays. *Phys. Rev. Lett.*, 118:191801, May 2017.

[47] R. Aaij et al. (LHCb Collaboration). Study of D_J meson decays to $D^+\pi^-$, $D^0\pi^+$ and $D^{*+}\pi^-$ final states in pp collisions. *Journal of High Energy Physics*, 2013(9), Sep 2013.

[48] R. Aaij et al. (LHCb Collaboration). Observation of $J/\psi p$ resonances consistent with pentaquark states in $\Lambda_b^0 \to J/\psi K^- p$ decays. *Phys. Rev. Lett.*, 115:072001, Aug 2015.

[49] E. Maurice. Fixed-target physics at LHCb. *arXiv e-prints*, Aug 2017.

[50] R. Aaij et al. (LHCb Collaboration). First measurement of charm production in fixed-target configuration at the LHC. *Phys. Rev. Lett.*, 122:132002, Apr 2019.

[51] S. Amato et al. (LHCb Collaboration). LHCb magnet: Technical Design Report. Technical report, Geneva, 2000.

[52] P. R. Barbosa-Marinho et al. (LHCb Collaboration). LHCb VELO (VErtex LOcator): Technical Design Report. Technical report, Geneva, 2001.

[53] R. Aaij et al. (LHCb VELO Group). Performance of the LHCb Vertex Locator. *Journal of Instrumentation*, 9(09), Sep 2014.

[54] J. Gassner, M. Needham, and O. Steinkamp. Layout and expected performance of the LHCb TT station. Technical report, CERN, Geneva, Apr 2004.

[55] P. R. Barbosa-Marinho et al. (LHCb Collaboration). LHCb inner tracker: Technical Design Report. Technical report, Geneva, 2002.

[56] P. R. Barbosa-Marinho et al. (LHCb Collaboration). LHCb outer tracker: Technical Design Report. Technical report, Geneva, 2001.

[57] I. Belyaev, G. Carboni, N. Harnew, C. Matteuzzi, and F. Teubert. The history of LHCb. *The European Physical Journal H*, 46(1), Mar 2021.

[58] S. Amato et al. (LHCb Collaboration). LHCb RICH: Technical Design Report. Technical report, Geneva, 2000.

[59] M. Adinolfi et al. (LHCb RICH group). Performance of the LHCb RICH detector at the LHC. *The European Physical Journal C*, 73(5), May 2013.

[60] S. Amato et al. (LHCb Collaboration). LHCb calorimeters: Technical Design Report. Technical report, Geneva, 2000.

[61] P. R. Barbosa-Marinho et al. (LHCb Collaboration). LHCb muon system: Technical Design Report. Technical report, Geneva, 2001.

[62] R. Antunes-Nobrega et al. (LHCb Collaboration). LHCb trigger system: Technical Design Report. Technical report, Geneva, 2003.

[63] I. Antcheva et al. ROOT — A C++ framework for petabyte data storage, statistical analysis and visualization. *Computer Physics Communications*, 180(12):2499–2512, 2009.

[64] S. Benson, V. Gligorov, M. A. Vesterinen, and J. M. Williams. The LHCb Turbo Stream. *Journal of Physics: Conference Series*, 664(8):082004, Dec 2015.

[65] T. Sjöstrand et al. An introduction to PYTHIA 8.2. *Computer Physics Communications*, 191:159–177, Jun 2015.

[66] S. Alioli, P. Nason, C. Oleari, and E. Re. A general framework for implementing NLO calculations in shower Monte Carlo programs: the POWHEG BOX. *JHEP*, 06:043, 2010.

[67] A. Ryd et al. EvtGen: A Monte Carlo Generator for B-Physics. Technical report, 5 2005.

[68] S. Agostinelli et al. Geant4—a simulation toolkit. *Nuclear Instruments and Methods in Physics Research Section A: Accelerators, Spectrometers, Detectors and Associated Equipment*, 506(3):250–303, 2003.

[69] A. Piucci. The LHCb upgrade. *J. Phys.: Conf. Ser.*, 878:012012, Jul 2017.

[70] R. Aaij et al. (LHCb Collaboration). LHCb Trigger and Online Upgrade Technical Design Report. Technical report, May 2014.

[71] R. Aaij et al. (LHCb Collaboration). LHCb VELO Upgrade Technical Design Report. Technical report, Nov 2013.

[72] R. Aaij et al. (LHCb Collaboration). LHCb Tracker Upgrade Technical Design Report. Technical report, Feb 2014.

[73] R. Aaij et al. (LHCb Collaboration). LHCb PID Upgrade Technical Design Report. Technical report, Nov 2013.

[74] I. Belyaev et al. Handling of the generation of primary events in Gauss, the LHCb simulation framework. *Journal of Physics: Conference Series*, 331(3):032047, Dec 2011.

[75] J. Palacios, Y. Xie, I. Belyaev, and Y. Amis. DaVinci Vertex Fitters documentation. `https://web.archive.org/web/20220123024832/https://twiki.cern.ch/twiki/bin/view/LHCb/VertexFitters`. Accessed: 23 Jan 2022.

[76] E. Hairer, G. Wanner, and S. P. Nørsett. *Solving Ordinary Differential Equations I: Nonstiff Problems*, chapter Runge-Kutta and Extrapolation Methods, pages 129–353. Springer Berlin Heidelberg, Berlin, Heidelberg, 1993.

[77] E. Bos and E. Rodrigues. The LHCb track extrapolator tools. Technical report, CERN, Geneva, Nov 2007.

[78] W. D. Hulsbergen. Decay chain fitting with a Kalman filter. *Nucl. Instrum. Meth. A*, 552:566–575, 2005.

[79] P. Li, E. Rodrigues, and S. Stahl. Tracking definitions and conventions for Run 3 and beyond. Technical report, CERN, Geneva, Feb 2021.

[80] M. Vesterinen. Considerations on the LHCb dipole magnet polarity reversal. Technical report, CERN, Geneva, Apr 2014.

[81] J. Podolanski and R. Armenteros. III. Analysis of V-events. *The London, Edinburgh, and Dublin Philosophical Magazine and Journal of Science*, 45(360):13–30, 1954.

[82] P. Baladrón Rodríguez et al. Calibration of the momentum scale of a particle physics detector using the Armenteros-Podolanski plot. *Journal of Instrumentation*, 16(06), Jun 2021.

[83] L. Pessina. *Studio di decadimenti di barioni Λ in preparazione alla misura dei momenti di dipolo elettromagnetici a LHCb*. Bachelor's Thesis, Università degli Studi di Milano, Milan, Italy, Oct 2020.

[84] F. Pedregosa et al. Scikit-learn: Machine learning in Python. *Journal of Machine Learning Research*, 12:2825–2830, 2011.

[85] G. Van Rossum and F. L. Drake. *Python 3 Reference Manual*. CreateSpace, Scotts Valley, CA, 2009.

[86] Y. Coadou. Boosted decision trees and applications. *EPJ Web of Conferences*, 55:02004, 2013.

[87] F. J. Massey. The Kolmogorov-Smirnov test for goodness of fit. *Journal of the American Statistical Association*, 46(253):68–78, 1951.

[88] N. P. Jurik. *Observation of $J/\psi p$ resonances consistent with pentaquark states in $\Lambda_b^0 \to J/\psi K^- p$ decays*. Ph.D. Thesis, Syracuse University, Syracuse, New York, Aug 2016.

[89] M. Ablikim et al. (BESIII Collaboration). Polarization and entanglement in baryon–antibaryon pair production in electron–positron annihilation. *Nature Physics*, 15(7):631–634, May 2019.